Simultaneous in situ determination of U-Th-Pb and Sm-Nd isotopes in monazite by laser ablation ICP-MS

by

© Dylan J. Goudie

A thesis submitted to the School of Graduate Studies

in partial fulfillment of the requirements for the degree of

Master of Science in Geology, Earth Sciences Dept., Faculty of Science

Memorial University of Newfoundland

June 2014

St. John's, Newfoundland and Labrador

Abstract

Results are presented for the in situ simultaneous determination of U-Pb and Sm-Nd isotopes in monazite using the Laser Ablation Split-Stream (LASS) method. This method uses a laser ablation system coupled to both a magnetic-sector inductively coupled plasma mass spectrometer (HR) (ICP-MS) for measuring U-Pb isotopes and multicollector (MC) ICP-MS for measuring Sm-Nd isotopes. The ablated material is split using a glass Y-connector and transported simultaneously to both mass spectrometers. In addition to Sm and Nd isotopes, the MC-ICP-MS is configured also acquire Ce, Nd, Sm, Gd, and Eu elemental abundances. This approach provides age, tracer isotope, and trace element data in the same ablation volume, thus reducing but not eliminating sampling problems associated with fine-scale zoning in accessory minerals. The precision and accuracy of the U-Pb method (along with the precision of the Sm-Nd method) is demonstrated by analysis of six well-characterized monazite reference materials. The LASS results agree within uncertainty with previously determined isotope dilution thermal ionization mass spectrometry (ID-TIMS) ages. Accuracy of the Sm-Nd method is assessed by comparing the LA-MC-ICP-MS results with ID-TIMS determinations on a well-characterized, in-house monazite reference material. The LASS method is then applied to monazite from the Birch Creek Pluton (BCP) in the White Mountains of southeastern California as a case study to illustrate the utility of this method for solving geologic problems. The U-Pb ages and Sm-Nd isotopic data determined using the LASS method support the conclusions drawn from previous results that monazite can record both timing and potential sources of hydrothermal fluids.

Acknowledgements

I would like to acknowledge Greg Dunning for providing the KMO3-72 and 93-GD-12 monazite samples, and Bill Davis for providing the GSC monazite samples. I would like to thank Mike Tubrett, Rebecca Lam, and Wilfredo "Jiggs" Diegor of the CREAIT network at Memorial University for their assistance with the LA-ICP-MS and LA-MC-ICPMS setups, as well as Sherri Strong, Lakmali Hewa, and Anne Westhues for their help with ID-TIMS Sm-Nd analyses of KMO3-72. I would also like to thank Chad Paton for his help in troubleshooting Iolite problems. I thank Chris Fisher, John Ayers, and Jim Crowley for helpful edits and comments. I would also like to thank Jim Crowley for performing the ID-TIMS analyses. This research was made possible by a Natural Sciences and Engineers Research Council of Canada (NSERC) Discovery Grant to JMH.

Table of Contents

List of Figures

List of Tables

List of Appendices

Chapter 1. Introduction

1.1 Monazite

Monazite-(Ce) is a relatively common rare earth element (REE) monoclinic orthophosphate (nominally $CePO_4$, with other REEs, Y, Th, and U substituting for Ce) accessory mineral found in a wide range of rock types [*Harrison et al*., 2002]. It occurs in igneous and metamorphic rocks, as a detrital mineral in sedimentary rocks, and in REE mineral deposits. Owing to high concentrations of U and Th (typically in the thousands of ppm U, and Th concentrations typically in the tens of thousands of ppm, and often > 50,000 ppm) [*Parrish*, 1990; *Heaman and Parrish*, 1991], high concentrations of radiogenic Pb (given the grain is not too young) and negligible amounts of common Pb, monazite has proven useful for constraining the timing of geologic events using U-Th-Pb isotopes [*Gebauer and Grünenfelder*, 1979; *Hawkins and Bowring*, 1997; *Harrison et al*., 2002; *Košler et al.*, 2001; *Kohn et al.*, 2008; *Warren et al.*, 2011]. Monazite is also useful for tracer isotope investigations using Sm-Nd isotopes, due to high concentrations of Sm and Nd (e.g., ~10^4 to 10^5 ppm) [*Tomascak et al*., 1998; *McFarlane and McCulloch*, 2007]. Similar to the combination of U-Pb age and Lu-Hf isotopic analyses in zircon [*Kemp et al.*, 2006*; Hawkesworth and Kemp*, 2006*; Yuan et al*., 2007; *Xie et al*., 2008], the Sm-Nd isotopic composition of monazite provides complementary information to the U-Th-Pb system, provided ages can be correctly assigned to measured Nd isotope compositions such that accurate initial $^{143}Nd/^{144}Nd$ can be obtained. As discussed in detail below, this may not always be possible in complexly zoned grains when different sample volumes are used for independent in situ U-Pb and Sm-Nd measurements, as has been done previously [*McFarlane and McCulloch*, 2007; *Iizuka et al.*, 2011a]. For this reason,

the utility of the Laser Ablation Split-Stream (LASS) technique will be evaluated for simultaneously determining age and Sm-Nd isotope composition in monazite.

Though not as widely used as zircon, monazite has proven to be a very useful U-Th-Pb geochronometer for many geologic applications [*Parrish*, 1990; *Heaman and Parrish*, 1991; *Košler et al.,* 2001; *Kohn et al*., 2008; *Warren et al.*, 2011]. The high concentrations of U, Th, and Pb in monazite allow for the determination of three independent ages, based on three distinct decay schemes: $^{208}Pb/^{232}Th$, $^{206}Pb/^{238}U$, and $^{207}Pb/^{235}U$ and also the dependant $^{207}Pb/^{206}Pb$ age [*Parrish,* 1990; *Košler et al*., 2001]. Monazite also has a relatively high closure temperature for Pb (i.e., ~700–900º C). [*Cherniak*, 2010] and is less prone to radiation damage than zircon due to self-annealing at low T [*Parrish*, 1990; *Harrison et al*., 2002]. Further, because the growth of monazite can often be linked to metamorphic processes (i.e., as inclusions in minerals such as garnet), U-Th-Pb dating of monazite is a powerful tool for constraining the timing of metamorphic events [*Foster et al., 2000; Košler et al*., 2001; *Williams et al.*, 2007*; Moecher et al*., 2011]. One disadvantage with U-Th-Pb dating of monazite, however, its ability to recrystallize under the influence of fluid related alteration causing its U-Th-Pb system to be reset [*Harlov et al.*, 2011; *Williams et al.*, 2011]. However, this tendency to recrystallize can sometimes help date fluid events, so in some cases it is not a disadvantage.

The Sm-Nd isotopic system in monazite has been used as an isotopic tracer [*Tomascak et al*., 1998; *McFarlane and McCulloch*, 2007; *Iizuka et al*., 2011b] but it can also be used in tandem with a mineral with contrasting Sm-Nd as a geochronometer by producing improved isochrons [*Evans and Zalasiewicz*, 1996]. The Sm-Nd isotopic

system is particularly useful for source region investigations, as both Sm and Nd are relatively immobile elements [*DePaolo*, 1988], are part of the monazite structure (N.B. monazite is nominally $CePO_4$ but always has other REEs present in the structure in descending concentrations from LREEs to HREEs) and would not be expected to readily diffuse out of the crystal during a thermal event, [*Cherniak et al.*, 2010] and large scale fractionation of Sm and Nd during most crustal processes is not expected.

Traditionally, high-precision Sm-Nd isotopic measurements in monazite were done by isotope dilution thermal ionization mass spectrometry (ID-TIMS) [e.g., *Hawkins and Bowring*, 1997; *Tomascak et al*., 1998] using whole grains or pieces of grains. More recently, isotopic analyses of monazite have been successfully done in situ using laser ablation multicollector inductively coupled plasma mass spectroscopy (LA-MC-ICP-MS) with sub-ε_{Nd} unit reproducibility [*McFarlane and McCulloch*, 2007; *Yang et al*., 2009; *Fisher et al*., 2011; *Iizuka et al*., 2011a] (an ε_{Nd} unit is a measure of relative deviation from the CHondritic Uniform Reservior (CHUR)) [*Bouvier et al.*, 2008], thereby allowing for Sm-Nd isotopic analysis of individual regions in monazite grains.

Combining U-Pb dating and Sm-Nd isotopes in monazite can be a powerful geochemical tool. Coupling these systems enables the determination of initial Nd isotopic compositions, and thus allows constraints to be placed on source region, material and age of the monazite.

In addition to age and Sm-Nd isotope data, this technique can also provide Ce-Nd-Eu-Gd, which are complementary to the U-Pb and Sm-Nd data and can be used in various geochemical applications. The most widely used application of these REE data is the

determination of the europium anomaly or Eu/Eu*, which is a measure of the relative abundance of Eu compared to Sm and Gd is related to the oxygen fugacity of the source magma [*Trail et al.,* 2012] and is often used to constrain the crystallization of plagioclase in melts [*Fowler and Doig,* 1983; *McFarlane and McCulloch,* 2007; *Fisher et al,* 2011]. Additionally, as presented by *McFarlane and McCulloch* [2007], calculating initial $^{143}Nd/^{144}Nd$ ratios using corresponding U-Pb or Pb-Pb ages, rather than Sm-Nd isochron ages, greatly reduces uncertainties, as the relatively small values and ranges of Sm/Nd in monazite preclude precise Sm-Nd age determination in Sm-Nd isochron dating.

1.2 Advantages of Laser Ablation Split-Stream

Monazite grains often have complex, fine-scale patchy zoning in addition to growth zoning, which can be highlighted when viewed with BSE imaging or elemental X-ray mapping [e.g., *Hawkins and Bowring,* 1997; *Williams et al*., 2007; *Williams and Jercinovic*, 2012]. These zones can be distinct in both composition and age within a single grain, leading to the need for in situ analysis in either thin section or grain mounts, with a spatial resolution suitable for the problem being addressed [*Williams et al*., 2007; *Williams and Jercinovic*, 2012].

To overcome these obstacles related to analyzing monazite, a method is presented that allows for the simultaneous measurement of U-Pb and Sm-Nd isotopes along with elemental concentrations of Ce, Nd, Sm, Gd, and Eu in monazite. Simultaneously sampling the same ablation volume for multiple geochemical systems at a single ablation site yields an excellent solution to the sampling limitations discussed above. Additionally, the relatively small (i.e., 20 μm) laser spot used in this study helps avoid, but does not

completely eliminate, the internal zoning problem in monazite mentioned above [*Hawkins and Bowring*, 1997; *Williams et al.*, 2007]. Previously, non-split-stream LA-ICP-MS measurements of U-Pb and Sm-Nd in monazite would have been collected using different laser spots typically with the U-Pb first and the Sm-Nd placed on top of or near the pre-existing laser crater ideally in the same growth-zone region. However, this increases the level of sampling uncertainty because of the differences in the ablation volumes, ablation depths, and ablation locations.

The LASS approach maximizes the amount of data that can be obtained from a single analysis by using two mass spectrometers simultaneously. This is ideal for U-Pb detrital monazite studies, in which a large number of grains need to be analyzed in order to obtain a statistically valid data set [*Hietpas et al*., 2010; *Hietpas et al*., 2011; *Moecher et al*., 2011]. In detrital studies, Sm-Nd isotopes can be used as a tracer of the source rocks in which the monazite originally crystallized, and the compositional zoning can reveal information about the metamorphic or igneous history of the monazite [*Ross et al*., 1991; *Iizuka et al*., 2011B]. Recently, *Hietpas et al*. [2010] showed that detrital monazite results could be used to constrain the metamorphic history of an area more reliably and more effectively than zircon, as monazite grows more readily in politic schist than zircon, and thus is able to better record low temperature metamorphic events. This makes monazite potentially more useful in detrital studies in areas that have substantial low-grade metamorphic materials.

The main limitation of a LASS configuration is that the signal strength to each ICP-MS is reduced when compared to measuring U-Pb or Sm-Nd separately because the total flux of ablated material is divided between the two ICP-MS instruments. The

ablation process and the throughput into the ICP-MS to the detector is already highly inefficient, with only ~1% of the ablated material making it to the detector [*Košler and Sylvester*, 2003]. By splitting the ablated material between the two ICP-MS instruments, the amount of material reaching each ICP-MS is slightly reduced, which ultimately reduces the precision of each analysis. This reduction will be discussed further in Chapter 4.

The precision and accuracy of U-Pb ages measured using the LASS method is assessed using six well-characterized (i.e., using ID-TIMS) monazite samples from the Geologic Survey of Canada (GSC), some of which have been used as U-Pb reference materials for the sensitive high-resolution ion microprobe (SHRIMP II) [*Stern and Berman*, 2000]. Two in-house monazite samples [*MacLachlan et al*., 2004; *G. Dunning*, pers. comm., 2012] were dated by ID-TIMS at Memorial University of Newfoundland and used to further assess the accuracy and precision of the U-Pb ages provided by the LASS method discussed in this paper. Additionally, five ID-TIMS Sm-Nd analyses were done on individual grains of one of the in-house samples (KMO3-72) and used to further assess the precision and accuracy of the Sm-Nd isotopic measurements conducted in LASS mode. This method is then applied in a case study using monazite grains from the Birch Creek Pluton (BCP), and surrounding rocks in which the BCP intruded, in the White Mountains of southeastern California [*Barton*, 2000; *Ayers et al*., 2006]. The results from this case study demonstrate how the simultaneous in situ determination of U-Pb isotopes, Sm-Nd isotopes, and REE concentrations in monazite using the LASS method can constrain the timing of the intrusion and source of the magma, and provide

information about the timing and nature of hydrothermal fluid interaction in surrounding rocks.

1.3 Previous work

The first simultaneous determination of age and tracer isotope data was done by *Woodhead et al.,* [2004] who used a single LA-MC-ICP-MS to measure both Pb and Hf isotopes. $^{207}Pb/^{206}Pb$ ages were measured using a MC-ICP-MS instrument with a zoom lens. *Harrison et al.* [2008] and *Kemp et al.,* [2009] completed similar studies and used the zoom optics feature on ThermoScientific NEPTUNE instruments. This approach uses depth profiling to help ensure that the Hf data that were coupled with $^{207}Pb/^{206}Pb$ ages were obtained from the same ablation volume and were unaffected by age mixing of multiple growth zones preserved in the zircon. *Woodhead et al.* [2004] demonstrated acceptable accuracy and only slightly degraded precision compared to individual analyses, using the zircon reference materials 91500 and BR266. The main drawback of the method, however, is that with only $^{207}Pb/^{206}Pb$ ages and no U-Pb or Th-Pb ages, there is no way to detect Pb loss or mixing of different age components.

Yuan et al. [2008] reported the first LASS measurements of U-Pb isotopes, Lu-Hf isotopes, and trace elements in well-characterized zircon reference materials using a quadrupole (Q) ICP-MS and a MC-ICP-MS. These authors demonstrated the potential of this technique, and their studies yielded results for both Lu-Hf and U-Pb, which was only slightly degraded from separate analyses of U-Pb and Lu-Hf.

Xie et al. [2008] also did LASS in situ measurements of U-Pb isotopes, Lu-Hf isotopes, and trace elements, in well-characterized zircon and baddeleyite reference

materials. Similar to *Yuan et al*. [2007], their setup utilized a Q-ICP-MS coupled with a MC-ICP-MS. Their U-Pb and Lu-Hf data agree with the reference values for the zircon and baddeleyite samples used in their study. They also found no evidence of any increased elemental fractionation when the aerosol is split in different proportions, which is a key result in support of LASS analyses.

Tollstrup et al. [2012] also completed simultaneous measurements of both U-Pb ages and Lu-Hf isotopes in zircon, using an HR-ICP-MS (ELEMENT) and a MC-ICP-MS (NEPTUNE Plus) coupled to a 193 nm laser ablation system. This is similar to what was used in our instrumental configuration discussed below, except our MC-ICP-MS is a NEPTUNE, not a NEPTUNE Plus, and our HR-ICP-MS is an ELEMENT XR. In that study, the U-Pb data were obtained from individual laser pulses, at a depth of 60 nm each, which allowed for depth profiling of the zircon. They found that LASS U-Pb ages of various reference materials were accurate to within 0.3–2.5% relative uncertainty (2σ) when compared with accepted values for those materials, and Lu-Hf isotopic compositions were accurate to within 1 ε_{Hf} unit relative to solution MC-ICP-MS analyses for the same reference materials. The authors then applied this method to discordant zircon grains from previous work in an attempt to resolve ages from previously unresolvable U-Pb data.

Kylander-Clark et al. [2013] did LASS "petrochronology" on reference zircon and monazite samples using both an HR-ICP-MS and a MC-ICP-MS coupled to a 193 nm excimer laser with spot sizes of 10 μm for monazite and 20 or 30 μm for zircon. In their setup, U-Th-Pb isotopes were measured on the MC-ICP-MS (Nu *Plasma HR*) and

elemental abundances were measured on the HR-ICP-MS (Nu *AttoM*). They measured U-Pb on the HR-ICP-MS and REE abundances on the MC-ICP-MS. Additionally, their laser was a 193 nm excimer laser and used spot sizes of 10μm for monazite and 20 or 30 μm for zircon. The LASS results for analyzed zircon reference materials (e.g., 91500, Plesovice) agreed with previously published values, except for Plesovice which was ~1% too old even within uncertainty, likely due to measured uncorrected Pb-U down-hole fractionation [*Kylander-Clark et al.,* 2013]. Weighted average $^{206}Pb/^{238}U$ dates for monazite reference materials analyzed (e.g., 44609, Bananeira, FC1, Manangotry, Trebilcock, and 554) agreed within 1% of accepted high precision TIMS values, except for Manangotry.

A LASS study using monazite was done by *Liu et al.,* [2012], who measured both Sm-Nd and U-Th-Pb data (as well as trace element concentrations) in situ using a quadrupole ICP-MS and a MC-ICP-MS. Analyses were done on several monazite reference materials (some of which have been previously characterized for U-Th-Pb ages) in order to determine if any of them were sufficiently homogenous (in both U-Pb and Sm-Nd) to be used as a monazite reference material for LASS studies. The robustness of the method was demonstrated by comparing LASS obtained values with previously accepted values (where available) or by doing additional ID-TIMS analyses for verification. To ensure the precision and accuracy of their MC-ICP-MS data, they also did a series of analyses on well characterized synthetic glasses; including JNdi-1 and a LREE-doped glass [*Fisher et al.,* 2011], and showed that their Sm-Nd values obtained agreed well with the ID-TIMS accepted values for those glasses. They concluded that the LASS method

for monazite can provide reliable U-Th-Pb ages and Sm-Nd isotopic information, and suggested Manangoutry and Namaqualand as potential LASS monazite standards.

Chapter 2. Methods

2.1 ICP-MS instrumentation

The simultaneous analyses presented in this study were done at Memorial University of Newfoundland in the MicroAnalysis Facility of the Bruneau Centre for Research and Innovation. The method used a ThermoFinnigan NEPTUNE MC-ICP-MS and a ThermoFinnigan ELEMENT XR high-resolution magnetic sector inductively coupled plasma mass spectrometer (HR-ICP-MS). The cup configuration (Table 2-1) for the NEPTUNE was identical to that used by *Fisher et al*. [2011]. This cup configuration allowed the determination of not only Sm-Nd isotopes but also Ce, Eu, and Gd isotopes. The NEPTUNE was run in static mode with an integration time of 2 seconds for each cycle with 15 cycles for background, 35 cycles for analysis and 15 cycles for washout. For the ELEMENT XR, time resolved intensity data were acquired by peak-hopping mode in a combination of pulse-counting for masses ^{204}Pb, ^{206}Pb, ^{207}Pb, ^{238}U and analog modes for ^{208}Pb, ^{232}Th, all at one point measured per peak. Dwell time per mass was 10ms except for ^{206}Pb (20ms) and ^{207}Pb (30ms). Operating parameters of the two ICP-MS instruments are reported in Table 2-2.

2.2 Laser ablation instrumentation

The samples in this study were ablated using a GeoLas 193 nm excimer laser. All unknowns and the U-Pb reference material were ablated with a laser spot size of 20 μm, which allowed for a relatively high degree of spatial resolution but at the same time maintaining sufficient signal intensity for precise isotopic measurements, which are only slightly degraded in comparison to separate U-Pb or Sm-Nd analyses of the same

material. The LREE glass described by *Fisher et al*. [2011], which was used as a Sm-Nd reference material, required an 89 μm spot due to lower concentrations of target elements present within the glass relative to natural monazite (e.g., wt. % Nd2O3 = 1.52 ±0.09 and wt. % Sm2O3 = 0.62±0.04). If possible, it is best to use the same spot size for both sample and standard; to eliminate any differences in possible laser induced fractionation of Sm-Nd during ablation; however this was not possible with the lower Sm and Nd concentrations of the LREE glass. As discussed by *Fisher et al*. [2011], Sm-Nd fractionation was very low (typically <1%), and thus the difference in laser-spot size between unknown and reference material does not introduce significant additional uncertainty. The laser operated at a frequency of 4 Hz and an energy density of 4 J/cm^2 (Table 2-3), compared to 10 Hz and an energy density of 3 J/cm^2 used in the study of *Liu et al*. [2012]. The laser power also represents a reduction compared to the parameters used in *Fisher et al*. [2011] (6 Hz and 6 J/cm^2) in an attempt to reduce the elemental fractionation of U and Pb and minimize the amount of sample consumed, while maintaining acceptable precision. An in-house built reduced-volume laser ablation cell (Fig. 2-1) was used to reduce bias that could be attributed to sampling position and to greatly reduce the "washout" times between analyses. All analyses consisted of 30 seconds of background followed by 70 seconds of ablation.

2.3 Laser Ablation Split-Stream analytical setup

The LASS method developed for this study used the laser ablation system described above interfaced to both a HR-ICP-MS and a MC-ICP-MS (Fig. 2-2). U-Pb

isotopes were measured on the HR-ICP-MS (Element XR), whereas the Sm-Nd isotopes and Ce, Eu, and Gd relative elemental concentrations were measured on the MC-ICP-MS (NEPTUNE). The ablated material is transported from the laser cell and then split using an in-house built baffled glass Y-connector (Fig. 2-3) and simultaneously transported to both mass spectrometers via Tygon tubing with an inner diameter of 4 mm. Tube lengths used in this study were ~90cm from the laser cell to the Y-connector, ~80cm from the Y-connector to the MC-ICP-MS and ~ 200cm from the Y-connector to the HR-ICP-MS. Various tube lengths were tested, and it was empirically determined that the length of the tubing used in this study, within reason, had little effect on signal intensity or quality of the data. The baffled Y-connector helps promote mixing of the aerosol particles after ablation and before the ablated material is introduced into each ICP-MS instrument.

Helium was used as a carrier gas to transport the ablated material toward the ICP-MS instruments. Nitrogen (N_2) gas was added to the argon sample gas inlet tube on the MC-ICP-MS for increased sensitivity for the Sm-Nd isotopes of interest. One would expect a similar increase in sensitivity if N_2 were added to the HR-ICPMS, however it has never been part of the lab practice at MUN and there was sufficient sensitivity without it adding the N_2. The gas flow rates used in this study are presented in Table 2-2.

2.4 Data-reduction methodology

To facilitate the data-acquisition process of using two ICP-MS instruments simultaneously, the MC-ICP-MS was set up with long acquisition times (combining multiple analyses in one large file with acquisition times typically ~2 hours) so that it would continuously acquire data whereas the user interacts predominately with the laser

ablation and HR-ICP-MS computer systems. All data for this study were reduced using Iolite v. 1.4, a non-commercial program designed specifically for processing mass spectrometer data and developed by the Melbourne Isotope Group at Melbourne University (www.iolite.org.au) [*Paton et al.*, 2011], that runs in the IgorPro software package (www.wavemetrics.com). The U-Pb data used the Iolite data-reduction scheme "U_Pb_Geochronology2," with a smoothed-cubic spline down-hole correction model, one of several U-Pb down-hole correction model options available within Iolite [*Paton et al*., 2010]. Other U-Pb down-hole correction models (e.g. linear, exponential) were also tested, however the smoothed-cubic spline best corrected the data.

The Sm-Nd data were reduced using a custom data-reduction scheme written in Iolite (available upon request from D.J. Goudie [d.goudie@mun.ca] or C.M. Fisher [chris.fisher@wsu.edu]). Care was used when selecting which portion of the ablation signal to integrate, as the signal must be checked for any abnormal spikes at mass 204 (i.e., common Pb) or other problems such as inclusions of other minerals. Contamination from common Pb typically happens when the ablation area overlaps a crack, inclusion, or incorporated in the mineral. While monazite commonly contains a small proportion of common Pb, no attempt was made to correct for common Pb. However, in the few cases where it was detected (based on elevated signal intensities at 204 amu), only the portion of the U-Pb signal with no contamination was selected. The complete Sm-Nd signal was still selected, as it is unaffected by this contamination.

The data reduction involved the use of two different reference materials: one for calibrating the U-Pb data; and one for calibrating the $^{147}Sm/^{144}Nd$ and other REE inter-elemental ratios. Trebilcock monazite (270 Ma) was used as the U-Pb calibration

material, as well as to correct $^{143}Nd/^{144}Nd$ as described in detail elsewhere [*Tomascak et al*., 1996; *McFarlane and McCulloch*, 2007; *Fisher et al*., 2011]. The $^{147}Sm/^{144}Nd$ calibration material was a synthetic LREE doped haploandesite glass [*Fisher et al*., 2011].

The customized Sm-Nd data-reduction scheme follows the data-reduction scheme discussed in *Fisher et al*. [2011], with the following exceptions: 1) baselines were corrected by using the automatic cubic spline function available in Iolite and were selected between each analysis, with typical integration times ~30 seconds. Our approach of selecting baselines between each sample ensured thorough washout between samples and still allowed for robust background correction. However, given the extremely high Nd concentrations, background corrections proved to be negligible provided there was thorough (~30 seconds) sample washout (e.g., ^{146}Nd signal/noise ratios are typically > 1,000,000); 2) the inter-elemental ratios $^{147}Sm/^{144}Nd$, Eu/Eu*, and Ce/Gd require calibration relative to an external standard (LREE Glass in this study), as described by *Fisher et al*. [2011]. In the original study, a standard-sample bracketing approach was employed using a linear fit between standards. A similar standard-sample bracketing approach was used here; however, the Iolite software offers numerous equations to define the behavior of standards including mean, linear, exponential, and various spline fits. In this study, an automatic spline was found to best define the drift of the standards and was therefore used to correct all of the data for this study; and 3) in the study of *Fisher et al*. [2011], the calculation of the Ce/Gd ratio was not discussed; however, the Ce/Gd ratio was calculated using the Ce and Gd abundance normalized voltages obtained from Iolite. This normalization procedure theoretically corrects for both instrumental drift and for

differential ablation yields of the individual elements using the LREE glass as the standard. The LREE glass has been characterized by solution ICP-MS for Ce (23,200 ± 1160 ppm) and Gd (3470 ± 174 ppm) content, and therefore the Ce/Gd ratio is 6.69 ± 0.70 [*Fisher et al.*, 2011].

In the present study, the isobaric interference of ^{142}Nd on ^{142}Ce was corrected using the measured ^{146}Nd and a ^{142}Nd/^{146}Nd reference value of 1.5782, and the ßNd determined for each sample (Eqs. 1 and 2) where, total142(v) is the total volts measured on the MC-ICP-MS at mass 142, ^{146}Nd(v)$_{\text{measured}}$ is the volts for ^{146}Nd measured on the MC-ICP-MS for the sample, $(\frac{^{142}\text{Nd}}{^{146}\text{Nd}})_{ref}$ is the natural ratio of ^{142}Nd to ^{146}Nd, and ßNd is the mass bias correction factor .

$$^{142}\text{Ce(v)}_{\text{calculated}} = \text{total142(v)} - {}^{142}\text{Nd(v)}_{\text{calculated}} \quad (1)$$

$$^{142}\text{Nd(v)}_{\text{calculated}} = {}^{146}\text{Nd(v)}_{\text{measured}} * (\frac{^{142}\text{Nd}}{^{146}\text{Nd}})_{ref} * (\frac{M146}{M142})^{\beta\text{Nd}} \quad (2)$$

As discussed in *McFarlane and McCulloch* [2007] and *Fisher et al*. [2011], LA-MC-ICP-MS Nd isotopic measurements typically yield lower ^{143}Nd/^{144}Nd than those reported by TIMS for the same materials by ~0.5 to ~1 ε_{Nd} unit. To facilitate direct comparison of TIMS and LA-MC-ICP-MS data, a further normalization of ^{143}Nd/^{144}Nd data was done relative to the ID-TIMS value of Trebilcock monazite interspersed between unknowns. This correction factor varies based on the measured Trebilcock values for that day, but it was typically ~1.000055 (~0.55 εNd units). The mean ^{143}Nd/^{144}Nd for Trebilcock monazite for the GSC analyses was 0.512585 ± 0.000037 (2SD) (Fig. 2-4), and the mean ^{147}Sm/^{144}Nd was 0.2180 ± 0.0096 (2SD). These data can be seen in

appendix Table B-1. Concordia diagrams, weighted mean plots, and Sm-Nd isochrons presented in this study were produced using Isoplot v. 3.34 [*Ludwig*, 2003]. The initial $^{143}Nd/^{144}Nd$ is calculated for these samples using the measured $^{143}Nd/^{144}Nd$, $^{147}Sm/^{144}Nd$, and $^{207}Pb/^{206}Pb$ age (for each GSC sample), and using 6.54 *10-12/year as the ^{147}Sm decay constant [*Lugamir and Marti*, 1978]. The Sm-Nd results for the GSC monazites are presented in Table 3-1.

2.5 Verifying the ^{144}Sm-^{144}Nd correction

Since ^{144}Nd is the reference isotope for $^{143}Nd/^{144}Nd$ and $^{146}Nd/^{144}Nd$, as well as $^{147}Sm/^{144}Nd$, it is very important that it is measured accurately. Due to potential for percent level of isobaric interference from ^{144}Sm on the reference isotope ^{144}Nd (e.g., ~3% for a monazite with $^{147}Sm/^{144}Nd$ of 0.14), an interference correction must be made in order to ensure accurate results. The correction applied in this study is made based on *Fisher et al*. [2011] and *Iizuka et al*. [2011a]. The corrected ^{144}Nd is determined by subtracting the calculated ^{144}Sm from the total 144 a.m.u. signal (Eq. 3), where the ^{144}Sm is calculated using the measured intensity of ^{149}Sm and an assumed reference value for $^{144}Sm/^{149}Sm$ and simultaneously being corrected for mass bias (Eq. 4):

$$^{144}\mathrm{Nd} = 144\mathrm{total} - {}^{144}\mathrm{Sm} \quad (3)$$

$$^{144}\mathrm{Sm} = {}^{149}\mathrm{Sm} * \left(\frac{^{144}\mathrm{Sm}}{^{149}\mathrm{Sm}}\right)_{\mathrm{ref}} * \left(\frac{M149}{M144}\right)\beta\mathrm{Sm} \quad (4)$$

Where $\frac{M149}{M144}$ represents the ratio of the atomic masses ^{149}Sm and ^{144}Sm, and βSm is the mass bias factor, which is calculated using measured $^{147}Sm/^{149}Sm$ values as is

detailed by *Fisher et al*. [2011]. The reference value for $^{144}Sm/^{149}Sm$ used in this study, as in *Fisher et al*. [2011], is that of *Isnard et al.* [2005] and is 0.22332.

In order to test the accuracy of this correction, analyses were done on synthetic REE +Y doped apatite (both "10x" apatite, which is synthetically grown apatite doped with ~10,000 ppm of individual REEs and Y, and "100x" apatite which is doped with ~10 wt % of individual REEs and Y), and synthetic REE + Y-oxide crystals [*Moore et al., 2013*], which have much higher Sm-Nd than monazite and other natural minerals suitable for in situ Sm-Nd isotopic analysis and thus have higher interference of ^{144}Sm on ^{144}Nd than is typically seen in natural minerals. TIMS Nd analyses were done on a 100x apatite sample and a REE+Y-oxide sample, giving $^{143}Nd/^{144}Nd$ compositions of 0.512456 ± 0.000007 and 0.512460 ± 0.000006, respectively. TIMS Nd analyses were also done on the Nd oxide powder used to make these synthetic minerals, giving a $^{143}Nd/^{144}Nd$ composition of 0.512440 ± 0.000007. The TIMS method for these analyses follows the methodology presented in *Fisher et al.*, [2011]. Even with these unnaturally high Sm concentrations, the interference correction accurately corrected the isobaric interference of ^{144}Sm on ^{144}Nd (Fig. 2-5), although the LA-ICP-MS $^{143}Nd/^{144}Nd$ values are systematically lower than the ID-TIMS values, consistent with results from previous studies (e.g., *Fisher et al.*, 2011). These synthetic apatite crystals are available from J.M. Hanchar [jhanchar@mun.ca; jmhanchar@gmail.com] upon request.

2.6 Uncertainty propagation

Given the relatively high parent-daughter ratio (i.e., Sm-Nd) of LREE-rich minerals like monazite, substantial correction for the in-growth of ^{143}Nd is required for

more ancient material, and the magnitude of this correction increases with age and Sm-Nd. As this correction can potentially be large, and subject to much larger uncertainty than the measured present day values, propagation of the uncertainty in a number of variables is necessary.

2.6.1 $^{147}Sm/^{144}Nd$ uncertainty propagation

The internal uncertainties (2SE) for $^{147}Sm/^{144}Nd$ are generally considered to be underestimates of the uncertainty in the $^{147}Sm/^{144}Nd$; therefore, for this study a method is described for propagating the $^{147}Sm/^{144}Nd$ uncertainty in the calibration material in that of the unknown to give a more reasonable uncertainty estimate (Eq. 5). This is required of most inter-element ratio determinations by LA-ICPMS, LA-MC-ICPMS and other methods, most notably U-Pb in zircon [*Jackson et al*., 2004]. This estimate (σ_p) includes the internal uncertainty (σ_1) in $^{147}Sm/^{144}Nd$ of the individual spot analyses of the sample, as well as the 2SD (σ_2) of the mean $^{147}Sm/^{144}Nd$ analysis of the standard, for the run in question.

$$\sigma p = \left(\frac{^{147}\mathrm{Sm}}{^{144}\mathrm{Nd}}\right)_{\mathrm{sample}} * \left[\left(\frac{\sigma 1}{\left(\frac{^{147}\mathrm{Sm}}{^{144}\mathrm{Nd}}\right)_{\mathrm{sample}}}\right)^2 + \left(\frac{\sigma 2}{\left(\frac{^{147}\mathrm{Sm}}{^{144}\mathrm{Nd}}\right)_{\mathrm{StdM}}}\right)^2\right]^{\frac{1}{2}} \quad (5)$$

For any run where the 2SD of the $^{147}Sm/^{144}Nd$ of the standard was <0.5%, an uncertainty of 0.5% was assigned.

2.6.2 Initial $^{143}Nd/^{144}Nd$ uncertainty propagation

A propagated uncertainty (σ) must also be determined for the initial $^{143}Nd/^{144}Nd$, and includes uncertainty in the measured $^{143}Nd/^{144}Nd$, $^{147}Sm/^{144}Nd$, and age. The equation

for this uncertainty propagation is adopted from *Iizuka et al*. [2011a] (Eq. 6).

$$\sigma^2 = \sigma_a^2 + \sigma_b^2 + (\sigma_f * [\frac{^{147}Sm}{^{144}Nd}]m * \left(1 - e^{\lambda t}\right))^2 + (\sigma_t * f_m * [\frac{^{147}Sm}{^{144}Nd}]m * \lambda e^{\lambda t})^2 \quad (6)$$

In this equation σ_a represents the internal uncertainty (2SE) of the $^{143}Nd/^{144}Nd$ value for each spot analysis, whereas σ_b represents the mean standard uncertainty (2SE) of the reference material (Trebilcock in this case) used to normalize the Nd isotopic data for each run. Also, σ_f represents the uncertainty in the fractionation factor (f_m) for $^{147}Sm/^{144}Nd$ estimated as the 2SD (from Iolite) of the mean correction factor from the standard (LREE glass) for each particular run, where f_m is the fractionation correction factor for each spot analysis. Additionally, $[\frac{^{147}Sm}{^{144}Nd}]m$represents the mean $^{147}Sm/^{144}Nd$ for each spot analysis. The uncertainty in the age is given as σ_t and is in Ma, as is *t* whereas λ is in Ma^{-1}.

2.7 ID-TIMS Method – Boise State University

Four to seven monazite grains from three samples from the Birch Creek Pluton were dated by the ID-TIMS at Boise State University. These analyses were performed on an Isotopx Isoprobe-T multicollector thermal ionization mass spectrometer equipped with an ion-counting Daly detector. Detailed ID-TIMS methodology is presented as Appendix A.

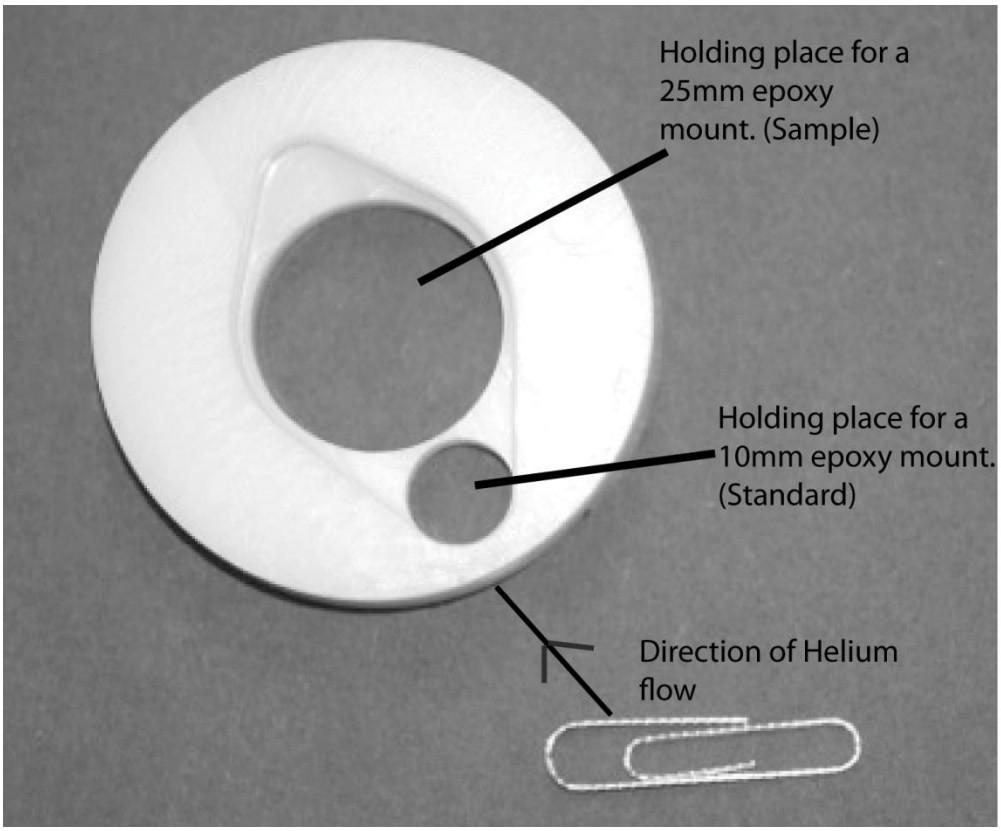

Figure 2-1: Custom laser ablation cell used in this study. Paper clip for scale.

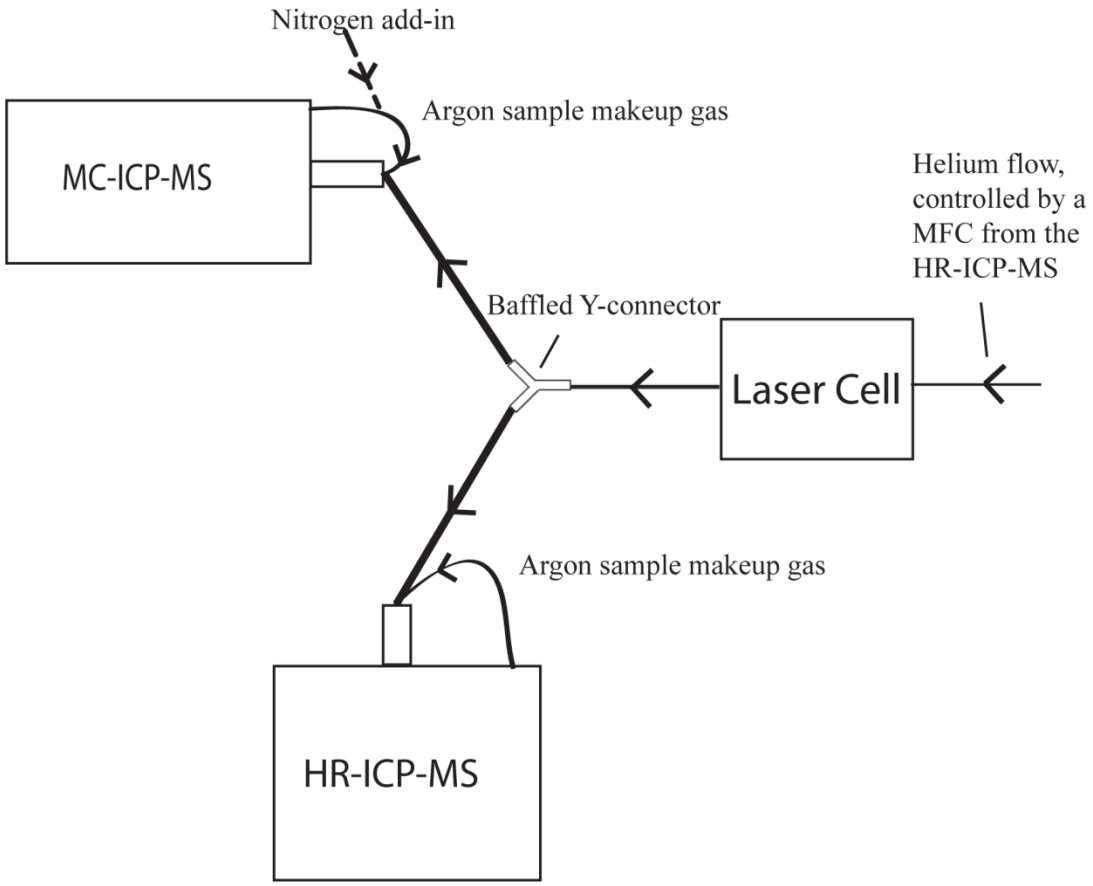

Figure 2-2: LASS analytical setup. MFC= Mass flow controller.

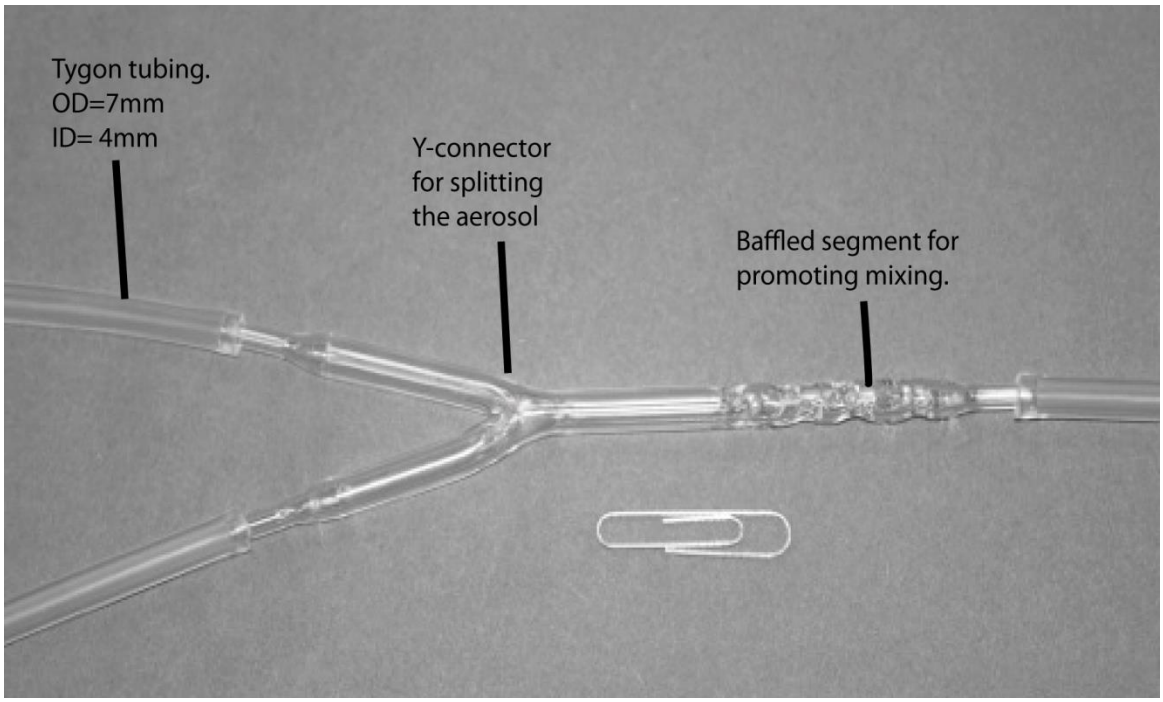

Figure 2-3: Glass Y-connecter for splitting aerosol. Paper clip for scale, OD = outer diameter, ID = inner diameter.

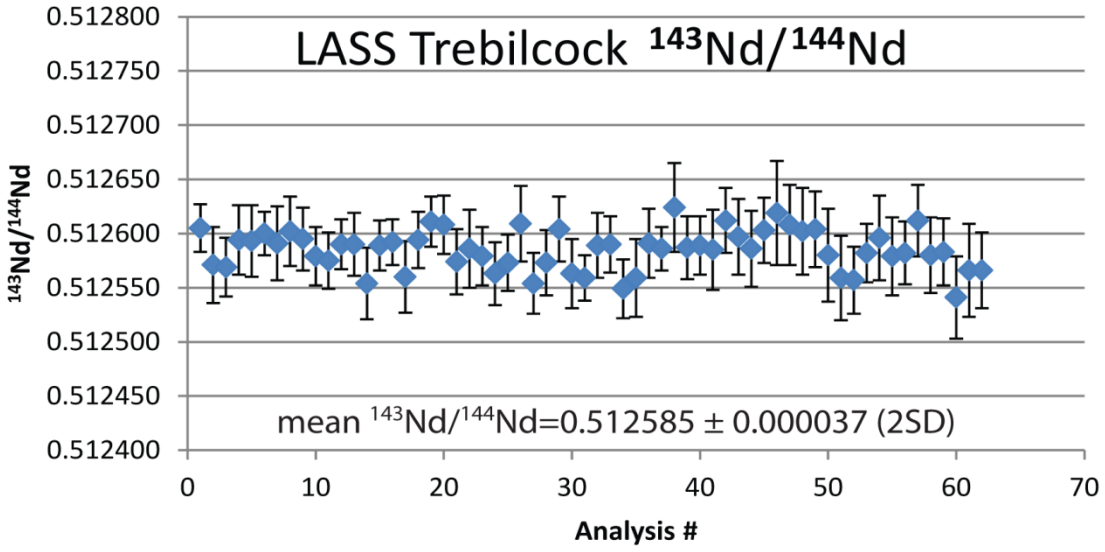

Figure 2-4: LASS Trebilcock monazite $^{143}Nd/^{144}Nd$ results.

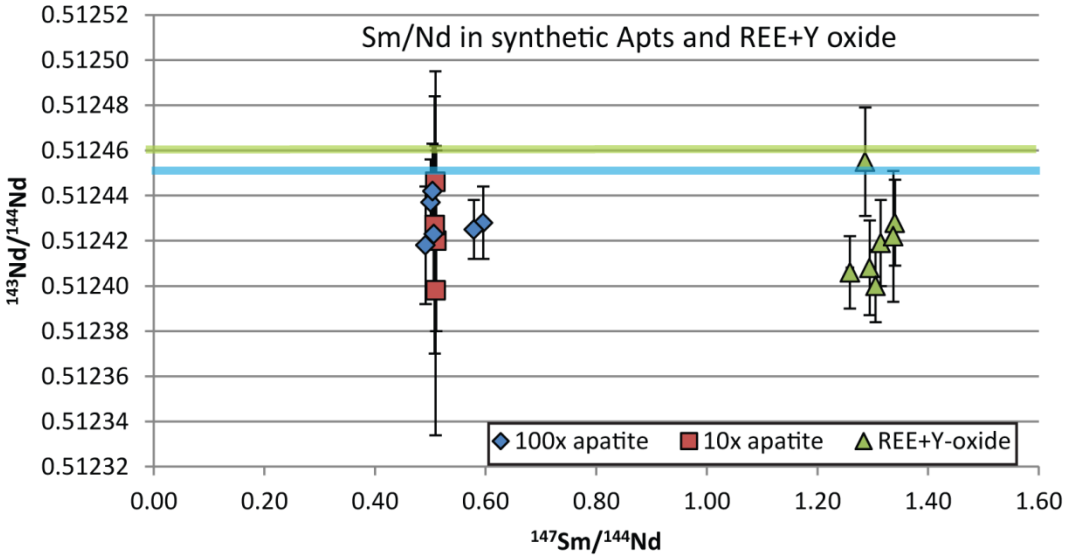

Figure 2-5: Sm-Nd in synthetic apatites and REE+Y oxide. Green line represents ID-TIMS Nd value for the REE+Y oxide, blue line represents ID-TIMS Nd value for 100x apatite.

Table 2-1: MC-ICP-MS cup configuration and interferences.

Cup configuration and interferences									
	L4	L3	L2	L1	Axial	H1	H2	H3	H4
Analyte	^{142}Nd	^{143}Nd	^{144}Nd	^{145}Nd	^{146}Nd	^{147}Sm	^{149}Sm	^{153}Eu	^{157}Gd
Interferences	^{142}Ce		^{144}Sm						$^{141}Pr^{16}O$

Table 2-2: Operating parameters for the two mass spectrometers.

Operating Parameters	**HR-ICP-MS**		**MC-ICP-MS**
Model	Element XR		Neptune
Forward Power	1150-1200W		1200W
Mass Resolution	Low		Low
Gas Flows:			
Cool/Plasma (Ar)	16 L/min		16 L/min
Auxiliary (Ar)	1.00 L/min		0.80 L/min
Sample Makeup (Ar)	1.20 L/min		0.980 L/min
Carrier Gas (He)	1.00 L/min		N/A*
Nitrogen (N_2)	N/A		6 mL/min
Sampler Cone	Nickel		Nickel
Skimmer Cone	Nickel "H"		Nickel "H"
*carrier gas was controlled from the HR-ICP-MS			

Table 2-3: Laser ablation operating parameters.

Laser Ablation	
Type	193 nm Ar-F excimer laser
Model	Geolas Pro
Repetition Rate	4 Hz
Energy Density	4 J/cm^2
Spot Size	20-89 microns

Chapter 3. Results

We selected eight monazite samples that are well characterized and have been previously used as primary or secondary U-Pb standards. We used the LASS method described in Chapter 2 to measure both U-Pb ages and Sm-Nd isotopic data and compare our results with previously published high precision ID-TIMS where available.

3.1 KMO3-72

The KMO3-72 monazite grains are from a high-grade gneiss terrane in the Trans-Hudson Orogen [*MacLachlan et al*., 2004]. This sample is used as an in-house quality control reference material and was provided by Dr. G. Dunning of Memorial University. Previous ID-TIMS work on this sample by *MacLachlan et al.,* [2004] gives a $^{207}Pb/^{206}Pb$ weighted average age of 1822 ± 1.5 Ma (MSWD=0.63) (Fig. 3-1A), which is in agreement with the LASS $^{207}Pb/^{206}Pb$ weighted average age of 1828.5 ± 9.9 (2σ, MSWD=3.0) (Fig. 3-1B). A high MSWD suggest that the sample is complex geologically or that uncertainties have been underestimated. A backscattered electron(BSE) image of a representative KMO3-72 grain can be seen as Figure 3-10B showing that the sample is not overly complex, suggesting that this high MSWD is due to an underestimation of the uncertainties.

ID-TIMS analyses were done on 5 individual grains of KMO3-72 monazite to determine their Sm-Nd isotopic compositions, following the ID-TIMS methodology reported by *Fisher et al.,* [2011]. The results of both LASS and ID-TIMS can be seen in Figure 3-1C, along with an 1822 Ma reference isochron. Data points from both the LASS and ID-TIMS results follow the trend of the reference isochron and are therefore in

agreement with each other, demonstrating the accuracy of LASS Sm-Nd isotopic measurements. The inset on Figure 2C shows a weighted mean initial $^{143}Nd/^{144}Nd$ plot for this sample with both the LASS and ID-TIMS data giving a mean of 0.510119 ± 0.000004. The LASS data have the larger error bars, while the ID-TIMS data have the smaller error bars. The LASS method also provided REE data for KMO3-72, giving a range of Eu^{*} values, 0.031-0.042, and a range in Ce/Gd of 12.98-14.85. Detailed results for KMO3-72 can be seen in Table B-2 in Appendix.

3.2 Sample 93-GD-12

The monazite grains for this sample (93-GD-12) originated in a garnet-staurolite-kyanite migmatite within the Port-aux-Basques Gneiss Complex, southwestern Newfoundland. This sample was chosen to test the accuracy and precision of the LASS method when analyzing young samples. Previous work on this sample gives an ID-TIMS $^{206}Pb/^{238}U$ date of 416 ± 1.2 Ma [*G. Dunning, pers. comm*. 2012]. A BSE image of a 93-GD-12 grain is displayed as Figure 3-10A. The LASS results for this sample are presented in Figure 3-2 as a U-Pb Tera-Wasserburg (TW) concordia (Fig. 3-2A) with a weighted mean $^{206}Pb/^{238}U$ age of 407.4 ± 6.5 Ma (2σ, MSWD = 3.9) and a Sm-Nd isochron (Fig. 3-2B) with an age of 348 ± 700 Ma (2σ, MSWD = 2.7). The high MSWD value for the $^{206}Pb/^{238}U$ age this sample represents an underestimation of the internal uncertainties. This isochron age has a very large uncertainty because of the small spread in the Sm-Nd ratio in this sample. 93-GD-12 showed a range of $^{147}Sm/^{144}Nd$ values of 0.1130-0.1285, and has a mean present day $^{143}Nd/^{144}Nd$ value of 0.511990 ± 0.000052

(2SD) and a mean $^{145}Nd/^{144}Nd$ value of 0.348425 ± 0.000035 (2SD). Detailed results for sample 93-GD-12 are presented in appendix Table B-2.

3.3 GSC monazite samples

A number of the monazite samples used in this study were supplied by the Geologic Survey of Canada, some of which are used as in-house SHRIMP II standards [*Stern and Sanborn*, 1998; *Davis et al*., 1998; *Stern and Berman*, 2001]. These samples have been previously dated by ID-TIMS (both $^{207}Pb/^{206}Pb$ and $^{208}Pb/^{232}Th$ ages) and are used in assessing the accuracy of the U-Pb age results obtained by the LASS method in this study. The $^{207}Pb/^{206}Pb$ ID-TIMS ages presented by *Stern and Berman* [2001] are more precise (i.e., lower analytical uncertainty) than the $^{208}Pb/^{232}Th$ ID-TIMS ages and thus are used as the ages to compare with our LASS results. The LASS Sm-Nd results for the six GSC samples are reported in Table 3-1 and the LASS U-Pb results for the GSC samples are reported in Table 3-2. BSE images of representative grains from each GSC sample are seen in Figure 3-11. These samples have not been previously characterized for Sm-Nd isotopic composition. A compilation of our LASS results for the six GSC samples are reported in Tables 3-1 and 3-2. These samples have not been previously characterized for Sm-Nd isotopic composition.

Additionally, a compilation of $^{145}Nd/^{144}Nd$ results for the GSC monazites, KMO3-72, 93-GD-12, Trebilcock monazites, and LREE Glass are shown in Figure 3-9A. Sm-Nd data for the reference materials, Trebilcock monazite and LREE Glass, are presented as appendix Tables B-1 and B-3 respectively.

3.3.1 GSC-1859

Sample GSC-1859 is a diatexite from the Asuanipi Complex of the Superior Province [*Stern and Sanborn*, 1998] and has ID-TIMS ages of 2662 ± 1 Ma for $^{207}Pb/^{206}Pb$ and 2676 ± 13 Ma for $^{208}Pb/^{232}Th$ [*Stern and Berman*, 2001]. The LASS U-Pb analyses for this sample are shown in Figure 3-3A and 3-3B, and yield a weighted mean $^{207}Pb/^{206}Pb$ age 2669 ± 11 Ma (2σ, MSWD = 0.23), which agrees within uncertainty with the reported ID-TIMS ages.

In addition to the U-Pb data mentioned above, the LASS method allowed for the simultaneous acquisition of Sm-Nd isotope data. The mean measured (present day) $^{143}Nd/^{144}Nd$ obtained from this sample was 0.510302 ± 0.000043 (2SD), with a mean $^{145}Nd/^{144}Nd$ ratio of 0.348431 ± 0.000029 (2SD). Sample GSC-1859 showed a very narrow range of $^{147}Sm/^{144}Nd$ from 0.0594 to 0.0619, causing very large uncertainties on the Sm-Nd isochron (Fig. 3-3C). A weighted mean initial $^{143}Nd/^{144}Nd$ of 0.509227 ± 0.000045 (2SD) was obtained (Fig. 3-3D). Eu* values for this sample ranged from 0.217 to 0.234, and Ce/Gd ranged from 55.27 to 62.49. An example of a monazite grain from this sample is shown in the BSE images in Figure 3-11A.

3.3.2 GSC-1861

Sample GSC-1861 is a leucosome in a paragneiss, also from the Ashuanipi Complex, Superior Province [*Stern and Sanborn*, 1998] and has ID-TIMS ages of 2666 ± 1.0 Ma for $^{207}Pb/^{206}Pb$ and 2667 ± 13 Ma for $^{208}Pb/^{232}Th$ [*Stern and Berman*, 2001]. The LASS U-Pb analyses for this sample are presented in Figure 3-4A and 3-4B, and give a $^{207}Pb/^{206}Pb$ weighted average age of 2676.2 ± 9.8 Ma (2σ, MSWD = 0.33), which is in

agreement, within uncertainty, with the reported ID-TIMS ages.

The mean measured (present day) $^{143}Nd/^{144}Nd$ was 0.510558 ± 0.000306 (2SD). The standard deviation is relatively high due to the large range in Sm and Nd seen in this sample. The mean $^{145}Nd/^{144}Nd$ for this sample was 0.348426 ± 0.000022 (2SD). The measured $^{147}Sm/^{144}Nd$ for this sample ranged from 0.0619 to 0.0874 based on 14 analyses. A Sm-Nd isochron for sample 1861 (Fig. 3-4C) gives an isochron age of 2547 ± 150 Ma (2σ, MSWD = 0.96), which overlaps both the LASS $^{207}Pb/^{206}Pb$ age and the ID-TIMS ages for this sample. A weighted mean initial $^{143}Nd/^{144}Nd$ of 0.509215 ± 0.000031 (2SD) was obtained (Fig. 3-4D). This sample showed a large range in Ce/Gd values, 23.71 to 52.70, and displayed a Eu* range from 0.074 to 0.256. An example of a monazite grain from this sample is shown in the BSE images in Figure 3-11B.

3.3.3 GSC-2775

Sample GSC-2775 is a granulite facies orthogneiss from the Grenville Province in Quebec [*Stern and Sanborn*, 1998] and has monazite ID-TIMS ages of 1166 ± 3 Ma for $^{207}Pb/^{206}Pb$ and 1169 ± 6 Ma for $^{208}Pb/^{232}Th$ [*Stern and Berman*, 2001]. The LASS U-Pb results for this sample (Figs. 3-5A and 3-5B), give a weighted average $^{207}Pb/^{206}Pb$ age of 1190 ± 21 Ma (2σ, MSWD = 0.98), which agrees within uncertainty with the reported ID-TIMS ages. However, the relative uncertainty is high (~2%) and the mean age is ~2% higher than the ID-TIMS value.

The mean measured (present day) $^{143}Nd/^{144}Nd$ was 0.511852 ± 0.000047 (2SD) and the mean $^{145}Nd/^{144}Nd$ was 0.348426 ± 0.000017 (2SD). The measured $^{147}Sm/^{144}Nd$ ranged from 0.083885 to 0.091241 based on 11 analyses. A Sm-Nd isochron (Fig. 3-5C)

for this sample gives a highly inaccurate isochron age of 1530 ± 530 Ma (2σ, MSWD = 0.58), owing to the small spread in Sm-Nd and relatively young age. A weighted mean initial $^{143}Nd/^{144}Nd$ of 0.511180 ± 0.000039 (2SD) was obtained (Fig. 3-5D). The MC-ICP-MS also provided Eu* and Ce/Gd values, which ranged from 0.019-0.049 and 16.82-25.49, respectively. An example of a monazite grain from this sample is shown in the BSE images in Figure 3-11C.

3.3.4 GSC-2908

Sample GSC-2908 is a deformed muscovite granite within the East Athabasca Mylonite Zone [*Stern and Sanborn*, 1998] and is used as the low-Th standard for the GSC SHRIMP II lab. It has ID-TIMS ages of 1795.2 ± 0.7 Ma for $^{207}Pb/^{208}Pb$ and 1787 ± 9 Ma for $^{208}Pb/^{232}Th$ [*Stern and Berman*, 2001]. The LASS U-Pb results for this sample (Figs. 3-6A and 3-6B) provides a $^{207}Pb/^{206}Pb$ weighted average age of 1794 ± 11 Ma (2σ, MSWD = 0.32), which agrees within uncertainty with the reported ID-TIMS ages.

The mean measured (present day) $^{143}Nd/^{144}Nd$ was 0.512023 ± 0.000489 (2SD), with this large SD being caused by the large variation seen in Sm and Nd for this sample. The mean measured $^{145}Nd/^{144}Nd$ for this sample was 0.348431 ± 0.000023 (2SD). The range of values for $^{147}Sm/^{144}Nd$ was 0.1658-0.2628 based on 19 analyses. A Sm-Nd isochron (Fig. 3-6C) yields an age of 1773 ± 110 Ma (2σ, MSWD = 2.0), which is consistent with LASS $^{207}Pb/^{206}Pb$ age and previous ID-TIMS ages. A weighted mean initial $^{143}Nd/^{144}Nd$ of 0.509803 ± 0.000060 (2SD) (Fig. 3-6D) was also determined using the parameters outlined in section 3.3. This sample shows very small Eu* values, ranging from 0.0001 to 0.003, and also showed relatively low Ce/Gd values, ranging from 5.04 to

9.89. An example of a monazite grain from this sample is shown in the BSE images in Figure 3-11D.

3.3.5 GSC-3345

Sample GSC-3345 is a migmatite paragneiss from Baffin Island [*Stern and Sanborn*, 1998], and has ID-TIMS ages of 1821.0 ± 0.6 Ma for $^{207}Pb/^{206}Pb$ and 1822 ± 9 Ma for $^{208}Pb/^{232}Th$ [*Stern and Berman*, 2001]. This particular sample is currently used as the 'medium-Th' standard for the GSC SHRIMP II lab. The LASS U-Pb results for this sample (Figs. 3-7A and 3-7B) gives a $^{207}Pb/^{206}Pb$ weighted average age of 1831 ± 10 Ma (2σ, MSWD = 0.35) which agrees within 2σ uncertainty with the ID-TIMS ages from previous work.

The mean measured (present day) $^{143}Nd/^{144}Nd$ obtained through LASS for sample GSC-3345 is 0.510759 ± 0.000178 (2SD), which is an inflated external reproducibility due to the variation in Sm and Nd measured in this sample. The mean $^{145}Nd/^{144}Nd$ was 0.348429 ± 0.000021 (2SD). The range of $^{147}Sm/^{144}Nd$ in this sample is from 0.0683 to 0.1053, consisting of 21 analyses which yielded a Sm-Nd isochron with an age of 1592 ± 190 Ma (2σ, MSWD=1.9) (Fig. 3-7C). A weighted mean initial $^{143}Nd/^{144}Nd$ 0.509684 ± 0.000054 (2SD) (Fig. 3-7D) was determined using the measured $^{143}Nd/^{144}Nd$, $^{147}Sm/^{144}Nd$, and $^{207}Pb/^{206}Pb$ age. Eu* values for this sample ranged from 0.046 to 0.070, whereas Ce/Gd values showed a large range, from 16.98 to 83.81. An example of a monazite grain from this sample is shown in the BSE images in Figure 3-11E.

3.3.6 GSC-4170

Sample GSC-4170 is a monzogranite from South Baffin Island [*Stern and Sanborn,* 1998] and has previously determined monazite ID-TIMS ages of 1836.0 ± 0.5 Ma for $^{207}Pb/^{206}Pb$ and 1832 ± 11 Ma for $^{208}Pb/^{232}Th$ [*Stern and Berman,* 2001]. Sample 4170 is currently used as the 'high-Th' standard for the GSC SHRIMP II lab. The LASS U-Pb results for this sample (Figs. 3-8A and 3-8B) give a weighted average $^{207}Pb/^{206}Pb$ age of 1857 ± 13 Ma (2σ, MSWD=0.36). The LASS $^{207}Pb/^{206}Pb$ age is ~1.2% larger than the ID-TIMS age, and falls just outside of the analytical uncertainty.

The mean measured (present day) $^{143}Nd/^{144}Nd$ was 0.510796 ± 0.000143 (2SD), with a mean $^{145}Nd/^{144}Nd$ of 0.348431 ± 0.000028 (2SD). The range for $^{147}Sm/^{144}Nd$ in this sample was 0.0854–0.1191, based on 17 analyses. A weighted mean initial $^{143}Nd/^{144}Nd$ of 0.509610 ± 0.000195 (2SD) (Fig. 3-8D) was also calculated based on the parameters outlined in Chapter 2.6. Additional REE data was also provided by the LASS method, giving Eu* values ranging between 0.006 and 0.022, and Ce/Gd values ranging from 14.40 to 30.35. An example of a monazite grain from this sample is shown in the BSE images in Figure 3-11F.

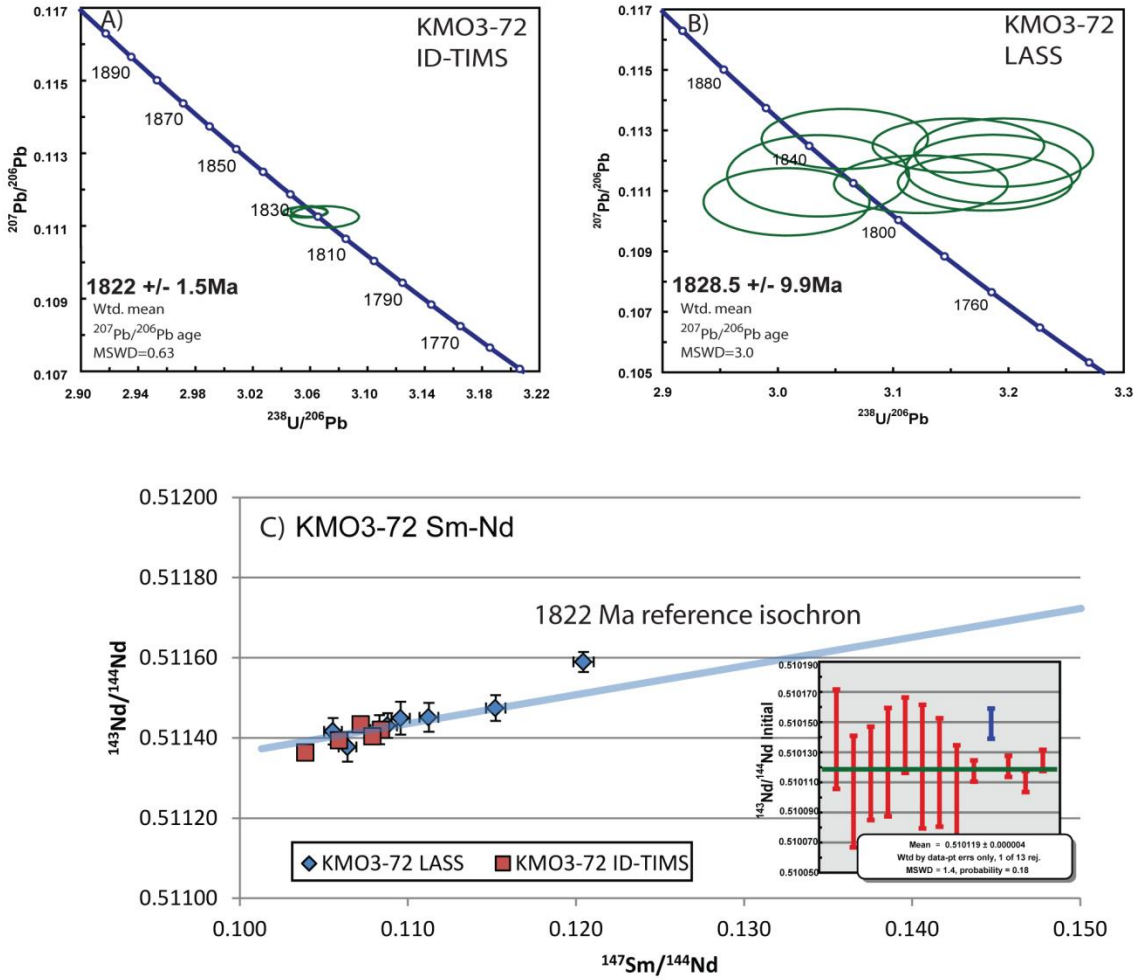

Figure 3-1: A) ID-TIMS U-Pb TW concordia for KMO3-72 with displayed $^{207}Pb/^{206}Pb$ weighted mean age (G. Dunning, pers. comm.). **B)** LASS U-Pb TW concordia for KMO3-72 with $^{207}Pb/^{206}Pb$ weighted mean age. **C)** Sm-Nd results for KMO3-72, with an 1822 Ma reference isochron. The inset on this figure shows a weighted average initial $^{143}Nd/^{144}Nd$ for this sample.

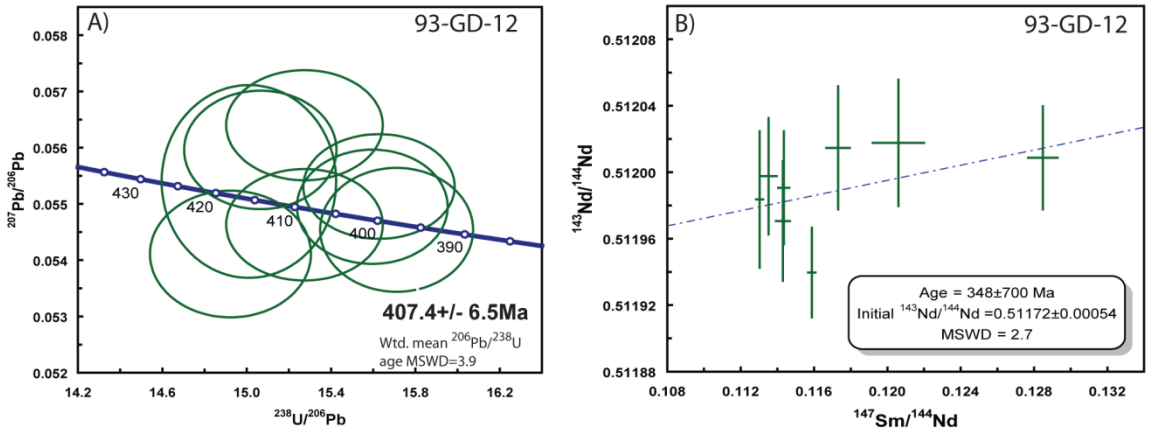

Figure 3-2: LASS results for 93-GD-12: **A)** U-Pb TW concordia for 93-GD-12 with displayed $^{206}Pb/^{238}U$ weighted mean age. **B)** Sm-Nd isochron for 93-GD-12.

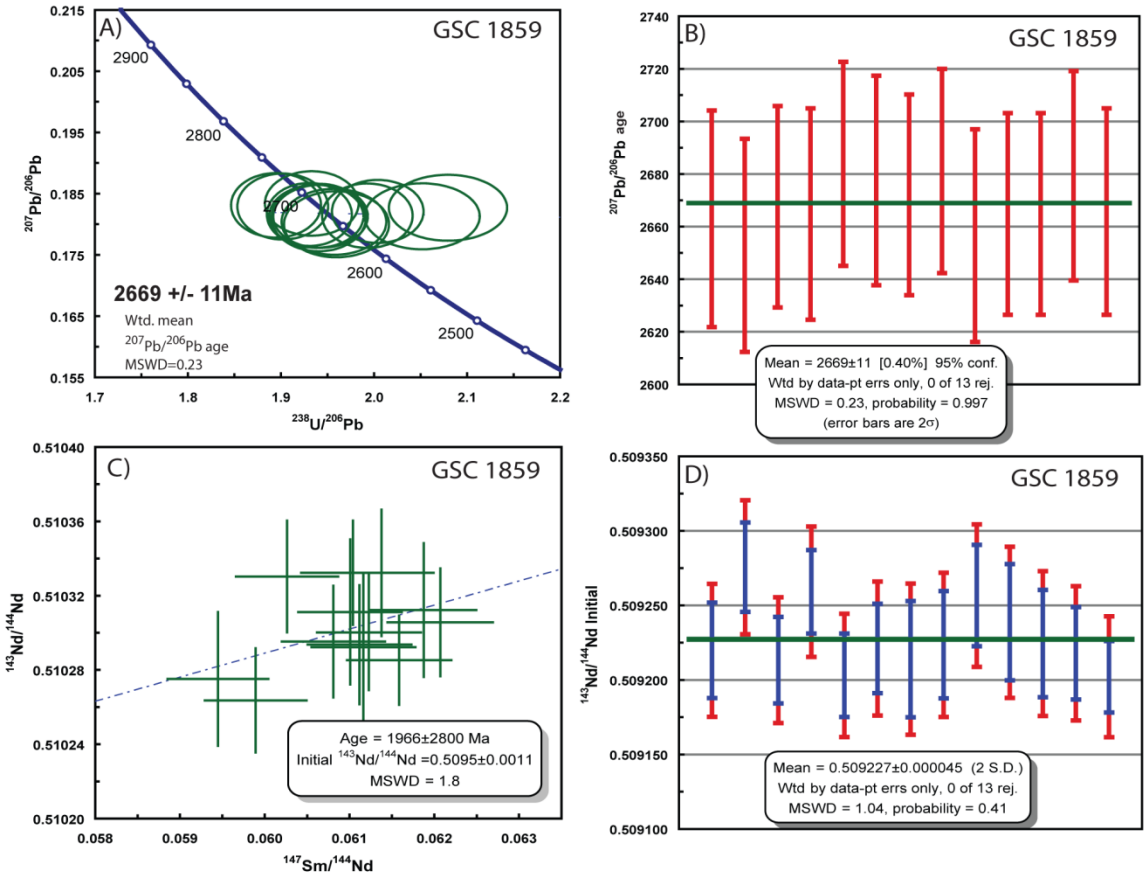

Figure 3-3: LASS results for sample GSC 1859. **A)** U-Pb TW concordia with displayed $^{207}Pb/^{206}Pb$ weighted mean age. **B)** Weighted mean $^{207}Pb/^{206}Pb$ age (Ma) diagram. **C)** Sm-Nd isochron. **D)** Weighted mean initial $^{143}Nd/^{144}Nd$ isotopic composition. Blue lines represent measured 2 S.E., whereas red lines represent propagated uncertainty.

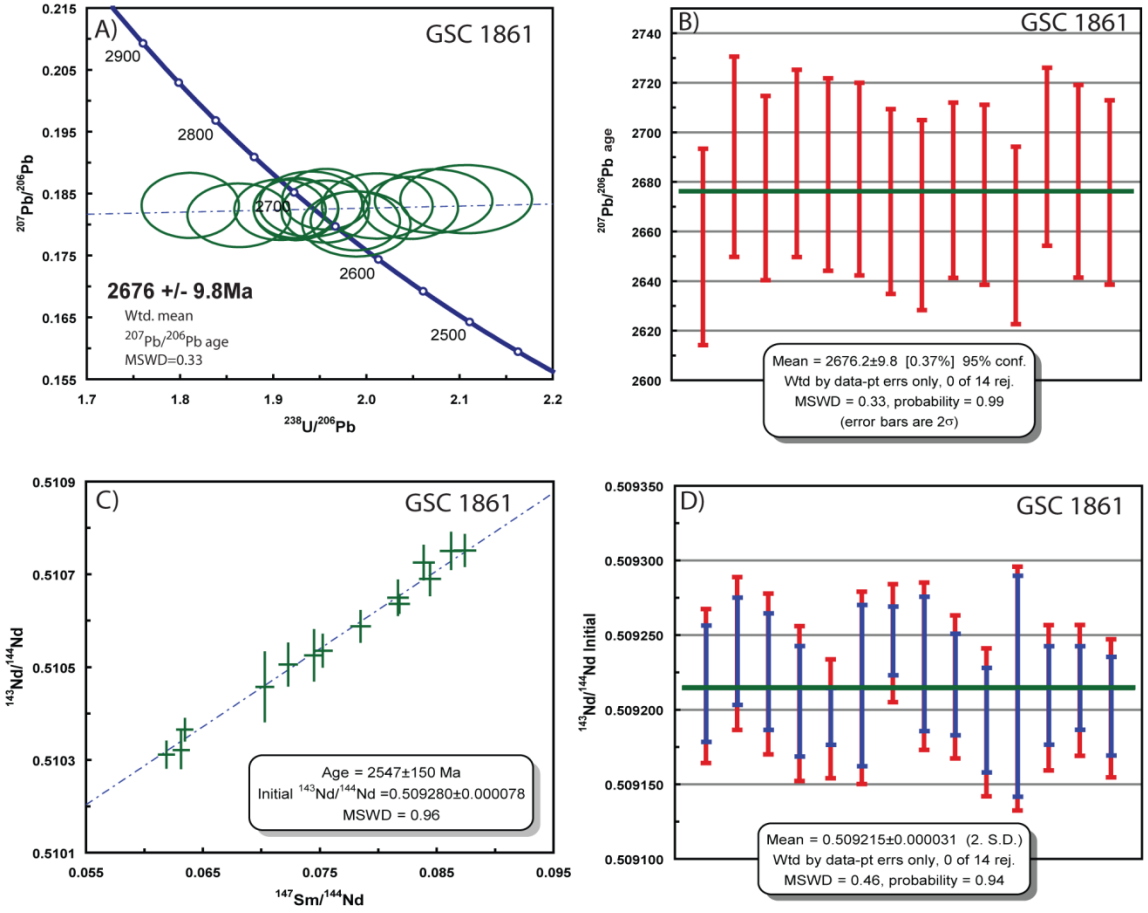

Figure 3-4: LASS results for sample GSC 1861. **A)** U-Pb TW concordia with displayed $^{207}Pb/^{206}Pb$ weighted mean age. **B)** Weighted mean $^{207}Pb/^{206}Pb$ age (Ma) diagram. **C)** Sm-Nd isochron. **D)** Weighted mean initial $^{143}Nd/^{144}Nd$ isotopic composition. Blue lines represent measured 2 S.E., whereas red lines represent propagated uncertainty.

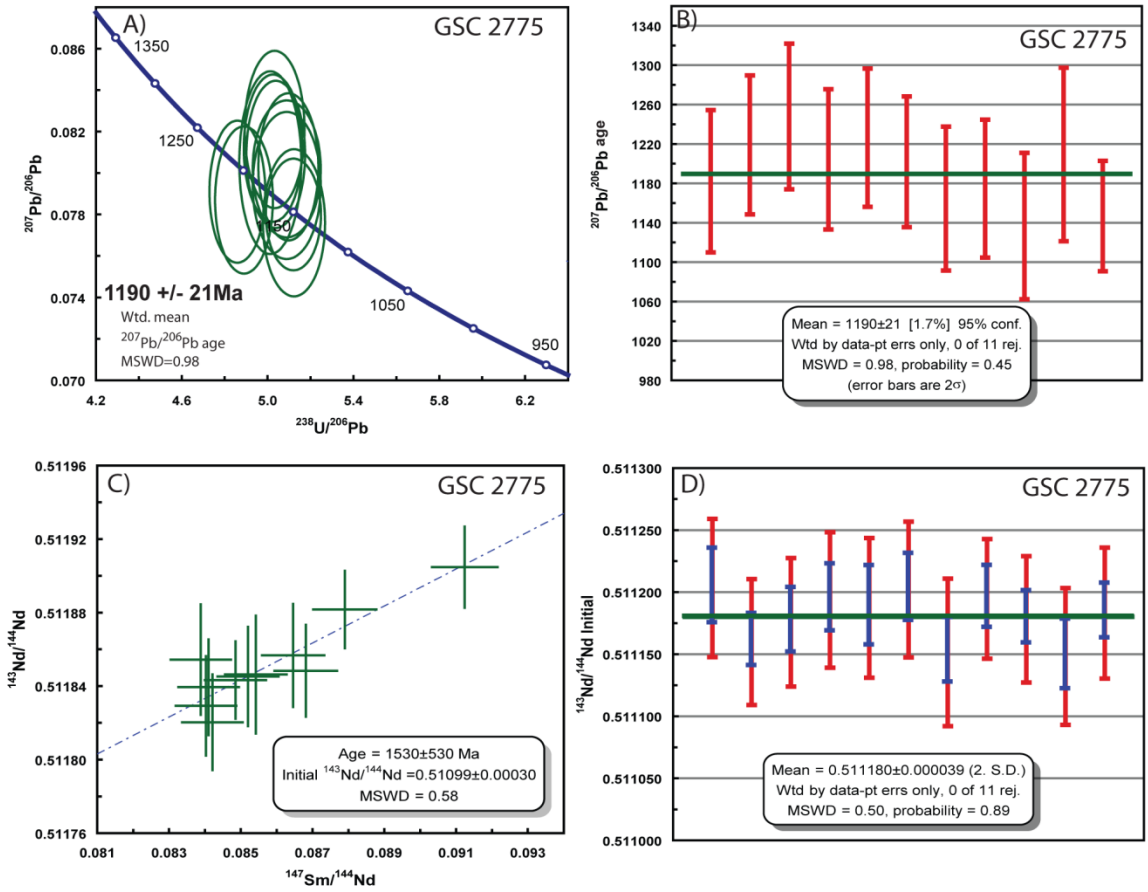

Figure 3-5: LASS results for sample GSC 2775. **A)** U-Pb TW concordia with displayed $^{207}Pb/^{206}Pb$ weighted mean age. **B)** Weighted mean $^{207}Pb/^{206}Pb$ age (Ma) diagram. **C)** Sm-Nd isochron. **D)** Weighted mean initial $^{143}Nd/^{144}Nd$ isotopic composition. Blue lines represent measured 2 S.E., whereas red lines represent propagated uncertainty.

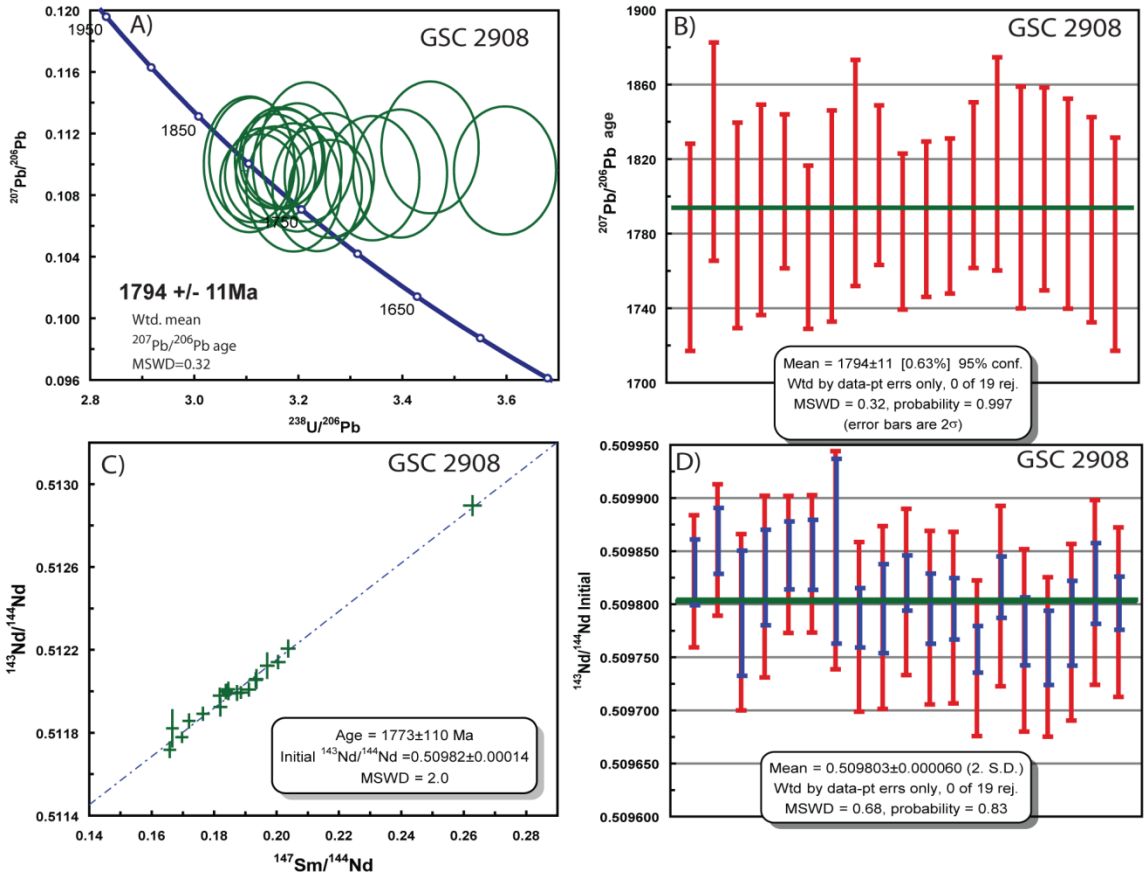

Figure 3-6: LASS results for sample GSC 2908. **A)** U-Pb TW concordia with displayed $^{207}Pb/^{206}Pb$ weighted mean age. **B)** Weighted mean $^{207}Pb/^{206}Pb$ age (Ma) diagram. **C)** Sm-Nd isochron. **D)** Weighted mean initial $^{143}Nd/^{144}Nd$ isotopic composition. Blue lines represent measured 2 S.E., whereas red lines represent propagated uncertainty.

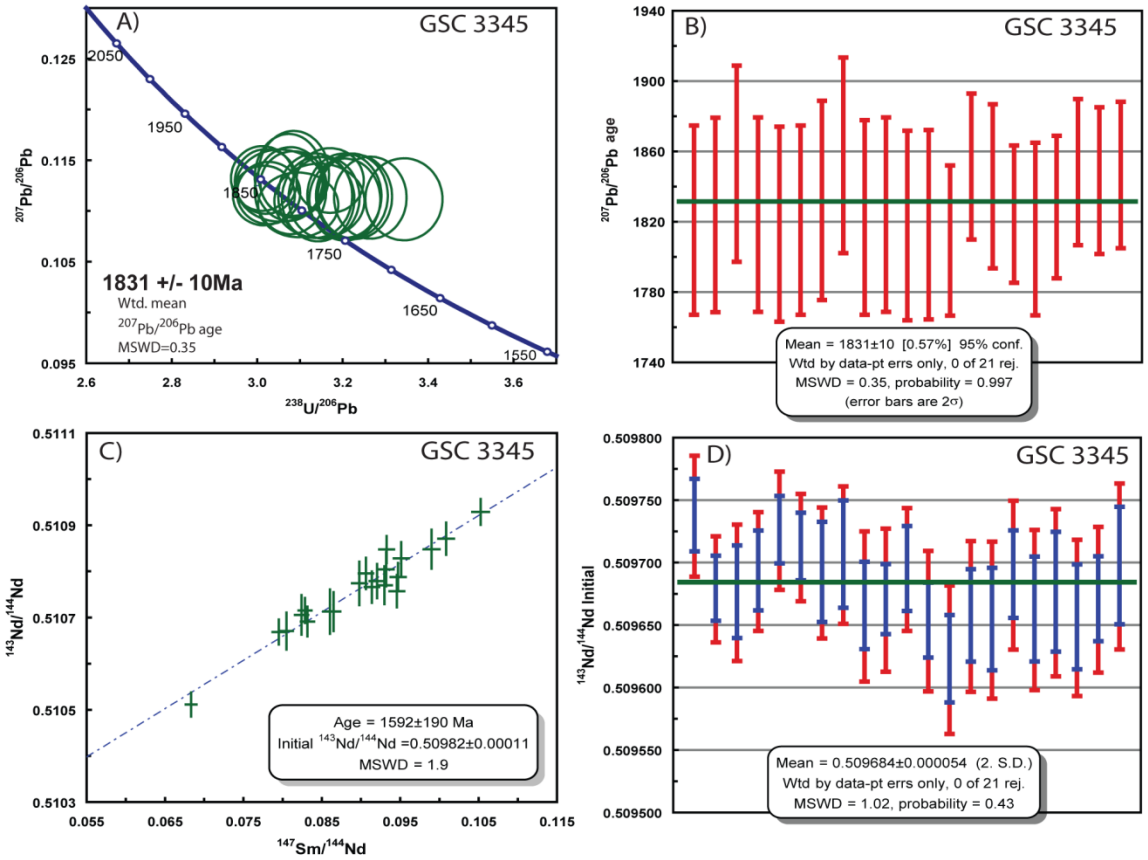

Figure 3-7: LASS results for sample GSC 3345. **A)** U-Pb TW concordia with displayed $^{207}Pb/^{206}Pb$ weighted mean age. **B)** Weighted mean $^{207}Pb/^{206}Pb$ age (Ma) diagram. **C)** Sm-Nd isochron. **D)** Weighted mean initial $^{143}Nd/^{144}Nd$ isotopic composition. Blue lines represent measured 2 S.E., whereas red lines represent propagated uncertainty.

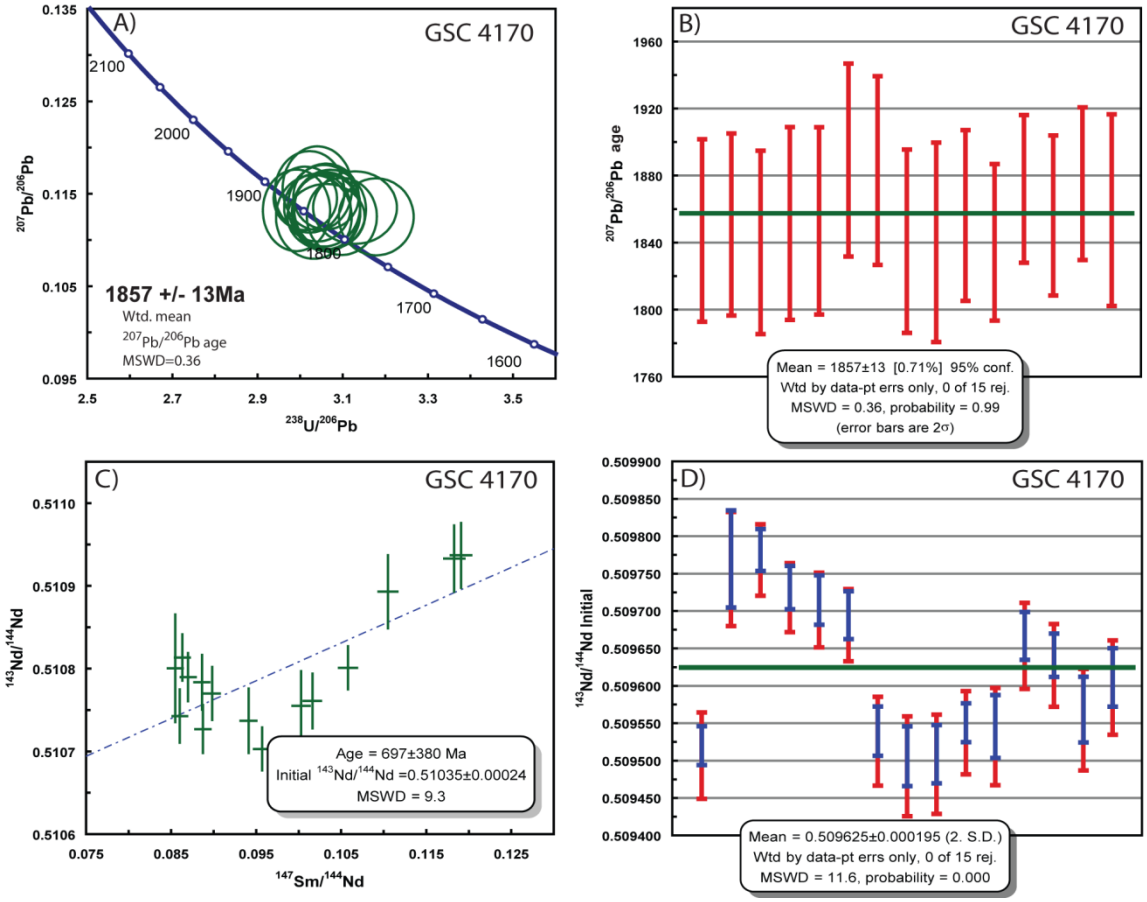

Figure 3-8: LASS results for sample GSC 4170. **A)** U-Pb TW concordia with displayed $^{207}Pb/^{206}Pb$ weighted mean age. **B)** Weighted mean $^{207}Pb/^{206}Pb$ age (Ma) diagram. **C)** Sm-Nd isochron. **D)** Weighted mean initial $^{143}Nd/^{144}Nd$ isotopic composition. Blue lines represent measured 2 S.E., whereas red lines represent propagated uncertainty.

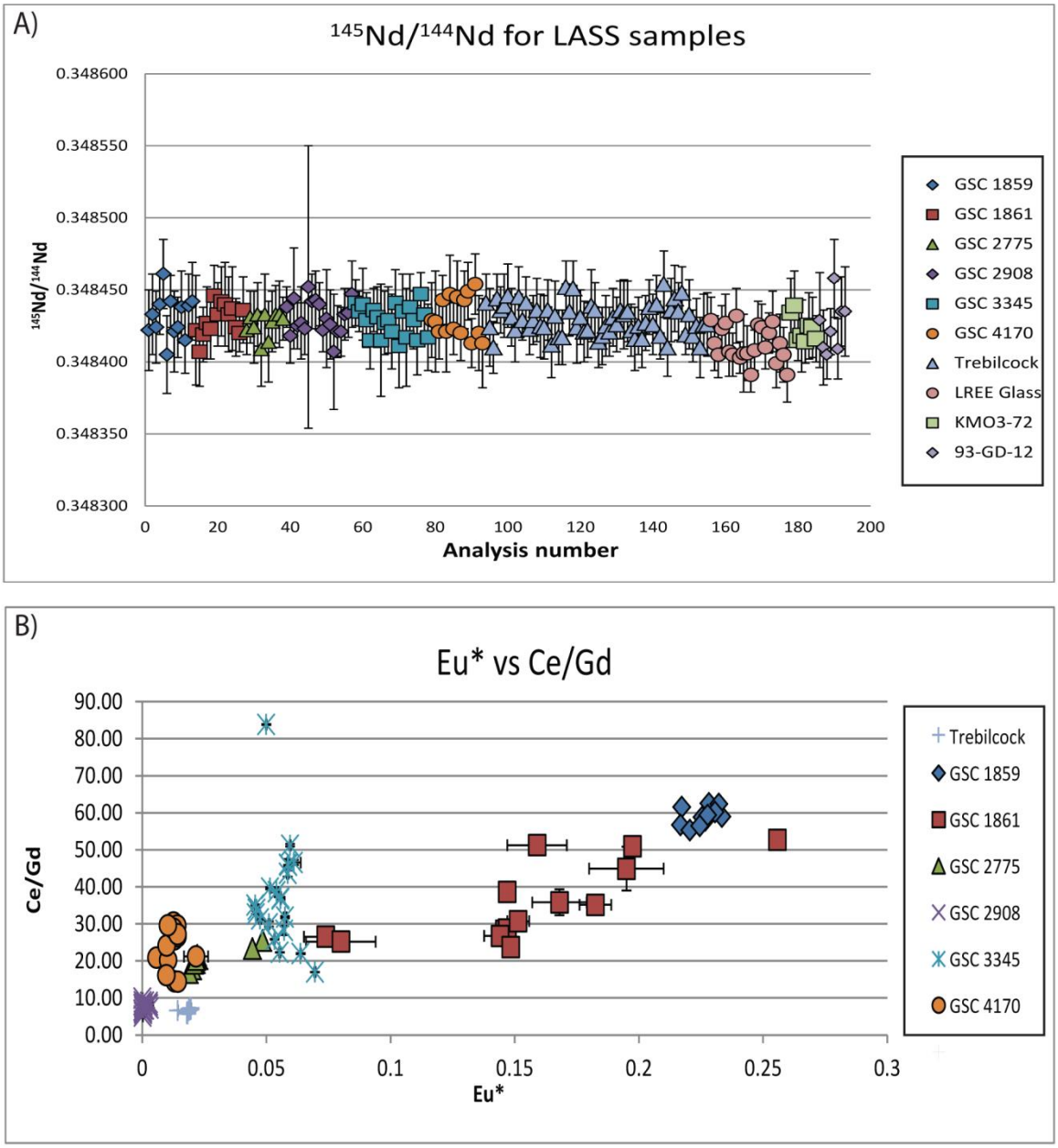

Figure 3-9: A) $^{145}Nd/^{144}Nd$ LASS results for various samples and reference materials. **B)** Rare Earth Element pattern for GSC samples and Trebilcock monazite

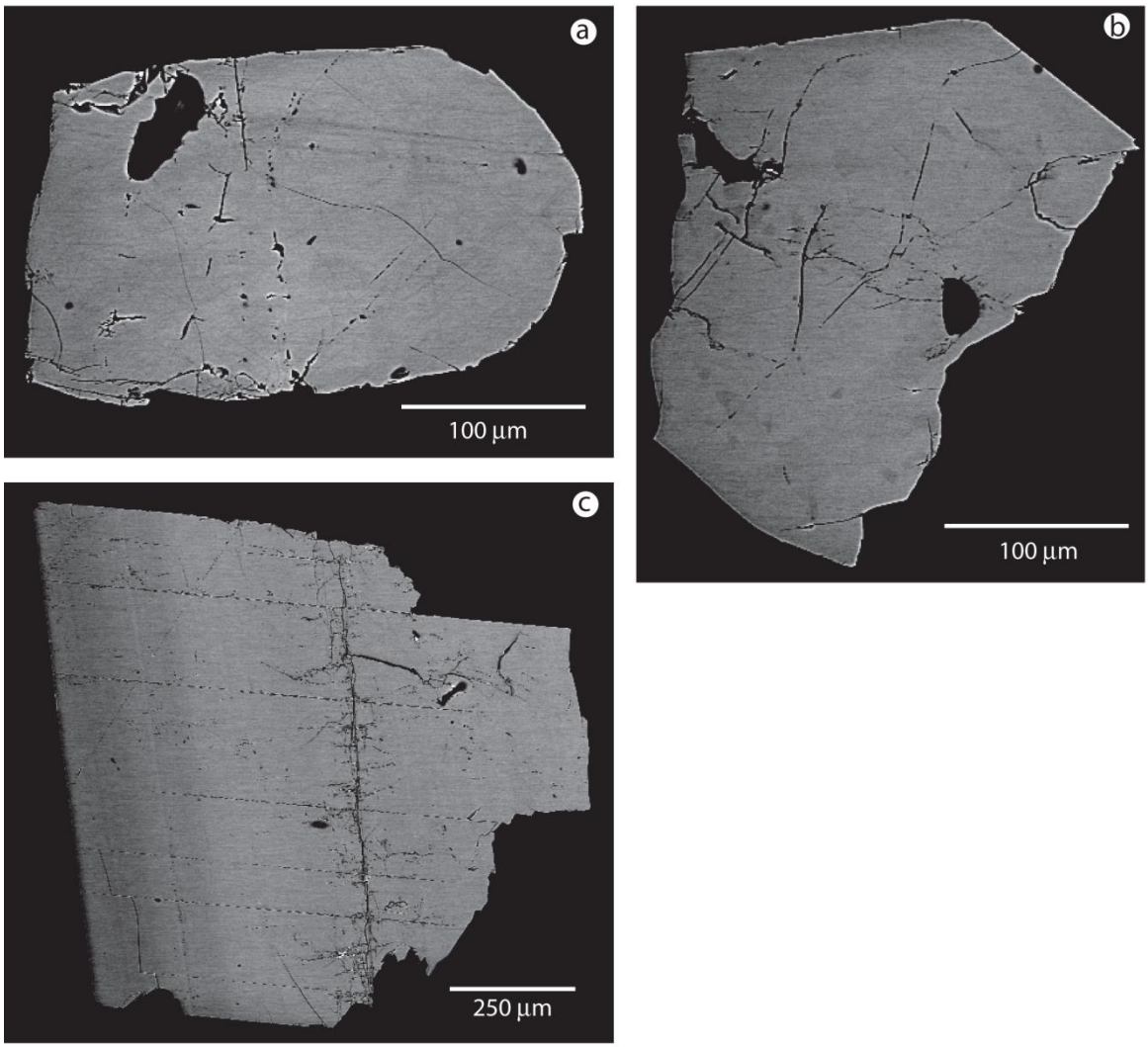

Figure 3-10: BSE images of **A)** 93-GD-12 **B)** KM03-72 and **C)** Trebilcock.

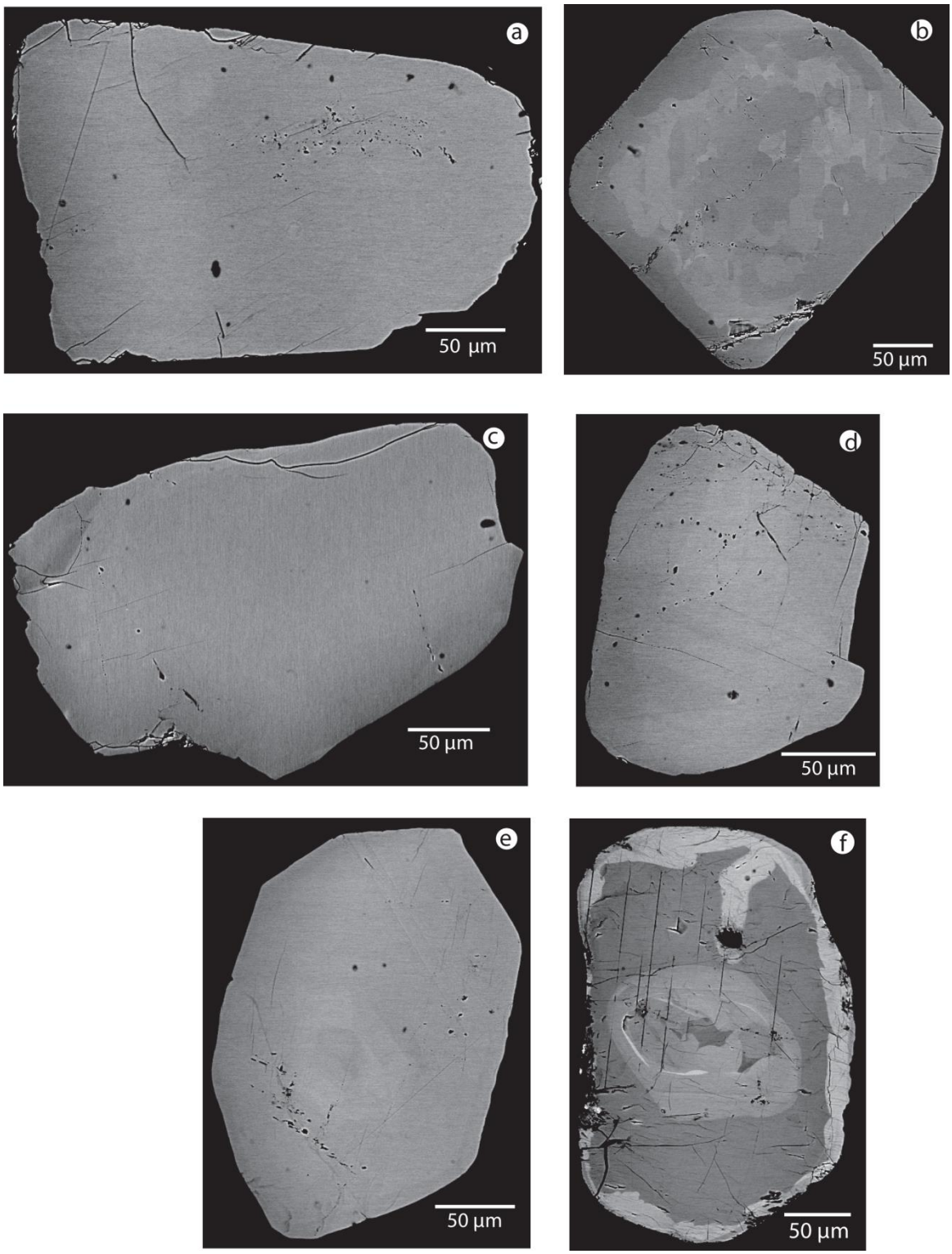

Figure 3-11: BSE images of **A)** GSC-1859 **B)** GSC-1861 **C)** GSC-2775 **D)** GSC-2908 **E)** GSC-3345 and **F)** GSC-4170

Table 3-1: LASS Sm-Nd and REE results for GSC Samples

Grain	$^{143}Nd/^{144}Nd$	2SE	$^{147}Sm/^{144}Nd$	Prop Uncertainty[1]	$^{145}Nd/^{144}Nd$	2SE	$^{143}Nd/^{144}Nd$ Initial	Prop Uncertainty	εNd(i)	Eu*	2SE	Ce/Gd	2SE
GSC 1859													
2	0.510294	0.000032	0.0611	0.0003	0.348422	0.000028	0.509220	0.000045	0.9	0.225	0.0004	58.79	0.20
3	0.510330	0.000030	0.0603	0.0001	0.348433	0.000028	0.509276	0.000045	1.7	0.217	0.0003	61.48	0.24
3	0.510306	0.000029	0.0621	0.0003	0.348424	0.000025	0.509213	0.000042	0.9	0.217	0.0003	56.71	0.21
4	0.510332	0.000028	0.0610	0.0001	0.348440	0.000021	0.509259	0.000044	1.7	0.228	0.0003	58.72	0.07
4	0.510264	0.000028	0.0599	0.0003	0.348461	0.000024	0.509203	0.000041	1.1	0.228	0.0004	62.49	0.28
5	0.510295	0.000030	0.0608	0.0001	0.348405	0.000027	0.509221	0.000045	1.3	0.233	0.0002	59.30	0.10
5	0.510292	0.000039	0.0612	0.0002	0.348442	0.000018	0.509214	0.000051	1.0	0.234	0.0003	58.96	0.08
5	0.510275	0.000036	0.0594	0.0002	0.348421	0.000028	0.509224	0.000048	1.4	0.232	0.0004	62.36	0.19
6	0.510332	0.000034	0.0614	0.0001	0.348424	0.000021	0.509257	0.000048	1.5	0.227	0.0002	57.97	0.23
6	0.510311	0.000039	0.0610	0.0002	0.348438	0.000025	0.509239	0.000051	1.3	0.231	0.0004	60.22	0.27
6	0.510312	0.000036	0.0619	0.0002	0.348415	0.000023	0.509224	0.000049	1.0	0.221	0.0002	55.27	0.12
7	0.510300	0.000031	0.0612	0.0002	0.348439	0.000022	0.509218	0.000045	1.3	0.228	0.0003	59.36	0.16
7	0.510285	0.000024	0.0616	0.0002	0.348442	0.000027	0.509202	0.000041	0.6	0.225	0.0002	56.46	0.13
GSC 1861													
1	0.510321	0.000039	0.0631	0.0007	0.348422	0.000038	0.509216	0.000052	0.6	0.256	0.003	52.70	1.20
2	0.510725	0.000036	0.0839	0.0010	0.348407	0.000024	0.509238	0.000051	1.9	0.074	0.009	26.53	0.77
3	0.510750	0.000039	0.0862	0.0006	0.348419	0.000019	0.509224	0.000054	1.5	0.080	0.014	25.20	0.36
4	0.510649	0.000037	0.0817	0.0002	0.348427	0.000025	0.509204	0.000052	1.1	0.146	0.0003	28.09	0.05
4	0.510636	0.000019	0.0818	0.0002	0.348423	0.000021	0.509194	0.000040	0.6	0.147	0.0002	28.50	0.05

Grain	$^{143}Nd/^{144}Nd$	2SE	$^{147}Sm/^{144}Nd$	Prop Uncertainty[1]	$^{145}Nd/^{144}Nd$	2SE	$^{143}Nd/^{144}Nd$ Initial	Prop Uncertainty	εNd(i)	Eu*	2SE	Ce/Gd	2SE
GSC-1861 (cont.)													
5	0.510525	0.000054	0.0745	0.0030	0.348446	0.000021	0.509215	0.000064	0.9	0.168	0.011	35.80	3.50
5	0.510365	0.000023	0.0635	0.0004	0.348433	0.000022	0.509245	0.000040	1.7	0.197	0.001	50.97	0.69
6	0.510505	0.000045	0.0723	0.0021	0.348442	0.000024	0.509229	0.000056	1.4	0.147	0.003	38.60	2.50
7	0.510535	0.000034	0.0753	0.0009	0.348440	0.000029	0.509215	0.000048	0.7	0.183	0.006	35.14	0.95
8	0.510690	0.000035	0.0844	0.0010	0.348433	0.000026	0.509191	0.000050	1.0	0.144	0.006	26.74	0.64
9	0.510457	0.000074	0.0703	0.0042	0.348437	0.000029	0.509214	0.000082	1.2	0.195	0.015	44.90	5.90
9	0.510751	0.000033	0.0874	0.0003	0.348424	0.000020	0.509208	0.000049	1.0	0.148	0.0005	23.71	0.15
10	0.510311	0.000028	0.0619	0.0005	0.348420	0.000013	0.509213	0.000044	1.5	0.159	0.012	51.25	0.83
12	0.510588	0.000033	0.0785	0.0004	0.348436	0.000023	0.509201	0.000046	0.9	0.151	0.004	30.70	1.20
GSC 2775													
1	0.511854	0.000030	0.0839	0.0002	0.348422	0.000017	0.511203	0.000056	2.0	0.022	0.0001	21.51	0.04
4	0.511843	0.000021	0.0849	0.0002	0.348431	0.000018	0.511160	0.000051	2.2	0.022	0.0001	21.04	0.08
5	0.511839	0.000026	0.0841	0.0002	0.348424	0.000025	0.511176	0.000052	1.9	0.049	0.0001	25.49	0.02
5	0.511845	0.000027	0.0852	0.0003	0.348433	0.000022	0.511194	0.000055	1.3	0.023	0.0002	20.55	0.17
6	0.511846	0.000032	0.0854	0.0003	0.348409	0.000026	0.511187	0.000056	1.5	0.021	0.0001	19.27	0.15
7	0.511829	0.000027	0.0840	0.0003	0.348433	0.000028	0.511202	0.000055	0.8	0.022	0.0001	20.74	0.05
8	0.511820	0.000026	0.0842	0.0007	0.348414	0.000028	0.511152	0.000059	1.6	0.022	0.0002	20.33	0.37
9	0.511848	0.000025	0.0868	0.0003	0.348428	0.000021	0.511195	0.000048	0.9	0.044	0.0009	23.33	0.12
10	0.511882	0.000021	0.0879	0.0004	0.348433	0.000020	0.511178	0.000051	2.4	0.020	0.0001	17.83	0.15
11	0.511857	0.000028	0.0865	0.0004	0.348433	0.000023	0.511148	0.000055	2.5	0.022	0.0001	19.52	0.05

Grain	$^{143}Nd/^{144}Nd$	2SE	$^{147}Sm/^{144}Nd$	Prop Uncertainty[1]	$^{145}Nd/^{144}Nd$	2SE	$^{143}Nd/^{144}Nd$ Initial	Prop Uncertainty	εNd(i)	Eu*	2SE	Ce/Gd	2SE
GSC 2908													
12	0.511905	0.000022	0.0912	0.0005	0.348430	0.000015	0.511183	0.000053	2.1	0.019	0.00004	16.82	0.03
28	0.512010	0.000031	0.1845	0.0009	0.348438	0.000014	0.509822	0.000062	-9.3	0.0001	0.00003	8.17	0.26
29	0.511857	0.000031	0.1720	0.0009	0.348418	0.000019	0.509851	0.000062	-9.5	0.0002	0.00003	8.88	0.11
30	0.512124	0.000059	0.1970	0.0010	0.348444	0.000035	0.509783	0.000083	-10.0	0.0001	0.00003	6.67	0.07
34	0.512896	0.000045	0.2628	0.0013	0.348425	0.000016	0.509817	0.000086	-10.0	0.0003	0.00001	5.04	0.15
37	0.511999	0.000032	0.1838	0.0018	0.348427	0.000025	0.509838	0.000065	-9.4	0.0012	0.0002	8.83	0.21
38	0.511978	0.000033	0.1818	0.0016	0.348423	0.000018	0.509838	0.000065	-9.3	0.0007	0.0001	8.23	0.16
39	0.511821	0.000087	0.1666	0.0007	0.348452	0.000098	0.509841	0.000103	-8.8	0.0001	0.00004	9.89	0.07
1b	0.512008	0.000028	0.1912	0.0005	0.348442	0.000019	0.509779	0.000080	-10.9	0.0004	0.00005	6.36	0.03
1b	0.512059	0.000042	0.1935	0.0006	0.348443	0.000020	0.509787	0.000086	-10.5	0.0003	0.00003	6.16	0.01
2b	0.511989	0.000026	0.1846	0.0003	0.348440	0.000015	0.509812	0.000078	-9.8	0.0031	0.0002	7.24	0.02
2b	0.511992	0.000033	0.1873	0.0003	0.348422	0.000015	0.509787	0.000082	-10.3	0.0013	0.0002	7.02	0.01
3b	0.511891	0.000029	0.1764	0.0009	0.348430	0.000034	0.509787	0.000081	-9.7	0.0029	0.0002	8.09	0.10
3b	0.511778	0.000022	0.1697	0.0007	0.348426	0.000024	0.509749	0.000073	-10.4	0.0028	0.0001	8.74	0.02
4b	0.512141	0.000029	0.2005	0.0011	0.348407	0.000040	0.509808	0.000085	-10.4	0.0004	0.00005	6.35	0.10
4b	0.512054	0.000032	0.1933	0.0028	0.348421	0.000018	0.509766	0.000086	-10.5	0.0007	0.0001	6.98	0.28
5b	0.511718	0.000035	0.1658	0.0015	0.348421	0.000017	0.509750	0.000075	-10.7	0.0004	0.00004	7.63	0.16
5b	0.511924	0.000040	0.1820	0.0002	0.348433	0.000018	0.509774	0.000083	-10.4	0.0005	0.00004	7.73	0.01
6b	0.512206	0.000038	0.2037	0.0008	0.348434	0.000017	0.509811	0.000087	-9.9	0.0004	0.0001	5.85	0.07
6b	0.511994	0.000025	0.1886	0.0002	0.348447	0.000023	0.509793	0.000080	-10.6	0.0004	0.0001	7.40	0.02

Grain	$^{143}Nd/^{144}Nd$	2SE	$^{147}Sm/^{144}Nd$	Prop Uncertainty[1]	$^{145}Nd/^{144}Nd$	2SE	$^{143}Nd/^{144}Nd$ Initial	Prop Uncertainty	εNd(i)	Eu*	2SE	Ce/Gd	2SE
GSC 3345													
1	0.510847	0.000029	0.0933	0.0004	0.348441	0.000016	0.509737	0.000048	-10.8	0.0575	0.0005	31.77	0.28
2	0.510511	0.000026	0.0683	0.0002	0.348435	0.000014	0.509679	0.000042	-10.9	0.0500	0.0002	83.81	0.11
3	0.510804	0.000037	0.0932	0.0009	0.348440	0.000025	0.509676	0.000055	-11.2	0.0572	0.0004	28.20	1.20
3	0.510691	0.000032	0.0832	0.0005	0.348429	0.000019	0.509693	0.000047	-11.3	0.0586	0.0003	43.58	0.85
4	0.510715	0.000027	0.0829	0.0002	0.348415	0.000020	0.509725	0.000047	-10.9	0.0588	0.0001	45.75	0.14
4	0.510669	0.000027	0.0795	0.0004	0.348436	0.000015	0.509712	0.000043	-10.8	0.0596	0.0002	51.22	0.35
5	0.510671	0.000040	0.0805	0.0004	0.348431	0.000021	0.509692	0.000052	-10.7	0.0611	0.0027	46.55	0.68
6	0.510706	0.000043	0.0824	0.0004	0.348415	0.000039	0.509706	0.000055	-10.6	0.0586	0.0005	46.00	1.50
7	0.510871	0.000035	0.1009	0.0002	0.348427	0.000022	0.509665	0.000060	-12.0	0.0638	0.0003	29.97	0.68
7	0.510929	0.000028	0.1053	0.0001	0.348429	0.000023	0.509670	0.000057	-11.9	0.0696	0.0002	21.97	0.15
7	0.510796	0.000034	0.0906	0.0005	0.348421	0.000026	0.509694	0.000049	-10.7	0.0511	0.0003	16.98	0.04
1b	0.510788	0.000030	0.0947	0.0002	0.348441	0.000023	0.509653	0.000056	-12.2	0.0557	0.0001	36.69	0.10
1b	0.510757	0.000035	0.0946	0.0001	0.348411	0.000029	0.509622	0.000059	-12.7	0.0558	0.0002	37.07	0.19
2b	0.510779	0.000037	0.0920	0.0001	0.348435	0.000026	0.509657	0.000060	-11.3	0.0456	0.0002	35.07	0.08
2b	0.510770	0.000041	0.0930	0.0001	0.348417	0.000034	0.509654	0.000063	-12.1	0.0458	0.0001	32.63	0.07
3b	0.510828	0.000035	0.0951	0.0002	0.348438	0.000023	0.509690	0.000060	-11.5	0.0533	0.0001	25.81	0.08
3b	0.510848	0.000042	0.0990	0.0001	0.348429	0.000020	0.509662	0.000064	-12.0	0.0554	0.0003	22.29	0.04
5b	0.510713	0.000048	0.0861	0.0003	0.348415	0.000024	0.509676	0.000067	-11.4	0.0515	0.0002	39.62	0.32
5b	0.510713	0.000042	0.0865	0.0001	0.348447	0.000015	0.509656	0.000063	-11.2	0.0541	0.0007	38.59	0.07
6b	0.510766	0.000034	0.0914	0.0002	0.348433	0.000015	0.509670	0.000058	-11.8	0.0475	0.0004	31.29	0.18
6b	0.510774	0.000047	0.0898	0.0002	0.348417	0.000023	0.509697	0.000066	-11.2	0.0461	0.0007	33.91	0.45

Grain	$^{143}Nd/^{144}Nd$	2SE	$^{147}Sm/^{144}Nd$	Prop Uncertainty[1]	$^{145}Nd/^{144}Nd$	2SE	$^{143}Nd/^{144}Nd$ Initial	Prop Uncertainty	εNd(i)	Eu*	2SE	Ce/Gd	2SE
GSC 4170													
1	0.510801	0.000026	0.1058	0.0004	0.348429	0.000026	0.509507	0.000058	-14.0	0.0073	0.0001	30.35	0.09
3	0.510800	0.000065	0.0855	0.0002	0.348428	0.000035	0.509756	0.000076	-9.2	0.0126	0.0005	29.57	0.26
5	0.510813	0.000028	0.0863	0.0003	0.348421	0.000019	0.509768	0.000048	-9.4	0.0141	0.0002	28.69	0.25
5	0.510790	0.000029	0.0870	0.0004	0.348443	0.000017	0.509718	0.000046	-9.6	0.0126	0.0005	27.25	0.66
6	0.510784	0.000033	0.0886	0.0004	0.348421	0.000028	0.509701	0.000050	-10.3	0.0143	0.0002	29.65	0.46
7	0.510743	0.000032	0.0860	0.0004	0.348447	0.000027	0.509681	0.000048	-10.2	0.0103	0.0006	19.14	0.08
1b	0.510761	0.000033	0.1016	0.0006	0.348423	0.000018	0.509526	0.000059	-14.0	0.0057	0.0002	20.89	0.16
3b	0.510933	0.000040	0.1183	0.0002	0.348445	0.000025	0.509492	0.000067	-14.5	0.0131	0.0002	14.50	0.03
3b	0.510937	0.000039	0.1191	0.0003	0.348420	0.000019	0.509495	0.000066	-14.8	0.0144	0.0002	14.40	0.09
4b	0.510703	0.000026	0.0957	0.0017	0.348443	0.000020	0.509537	0.000056	-13.7	0.0217	0.0049	21.20	1.20
4b	0.510755	0.000042	0.1003	0.0025	0.348449	0.000020	0.509532	0.000065	-13.7	0.0104	0.0009	20.20	1.20
5b	0.510770	0.000032	0.0898	0.0002	0.348413	0.000017	0.509653	0.000058	-10.4	0.0129	0.0006	25.80	0.19
5b	0.510727	0.000029	0.0888	0.0002	0.348454	0.000021	0.509627	0.000055	-11.1	0.0142	0.0007	26.64	0.18
6b	0.510893	0.000044	0.1105	0.0015	0.348420	0.000026	0.509555	0.000068	-13.6	0.0097	0.0001	16.12	0.48
6b	0.510737	0.000039	0.0941	0.0003	0.348413	0.000031	0.509598	0.000063	-12.8	0.0098	0.0001	24.14	0.13

[1] Uncertainties that were <0.5% are displayed as 0.5%

b indicates grains from a different mount

Table 3-2: LASS U-Pb results for GSC samples (ages in Ma)

Grain	^{206}Pb-^{238}U Age	Prop 2SE	^{207}Pb-^{235}U Age	Prop 2SE	^{207}Pb-^{206}Pb Age	Prop 2SE	$^{238}U/^{206}Pb$	Prop 2SE	$^{207}Pb/^{206}Pb$	Prop 2SE	$^{207}Pb/^{235}U$	Prop 2SE	$^{206}Pb/^{238}U$	Prop 2SE
GSC 1859														
2	2676	46	2664	36	2663	41	1.94	0.04	0.1811	0.0045	12.77	0.50	0.515	0.011
3	2659	52	2645	44	2653	41	1.96	0.05	0.1800	0.0044	12.55	0.60	0.510	0.012
3	2692	45	2675	36	2668	38	1.93	0.04	0.1816	0.0042	12.95	0.50	0.518	0.010
4	2561	51	2597	44	2665	40	2.05	0.05	0.1813	0.0044	11.93	0.57	0.487	0.012
4	2687	45	2677	36	2684	39	1.93	0.04	0.1834	0.0043	13.01	0.50	0.517	0.011
5	2529	50	2615	44	2678	40	2.08	0.05	0.1827	0.0044	12.18	0.58	0.481	0.012
5	2608	44	2639	36	2672	38	2.00	0.04	0.1821	0.0042	12.47	0.48	0.499	0.010
5	2733	46	2703	36	2681	39	1.89	0.04	0.1831	0.0043	13.33	0.51	0.528	0.011
6	2659	53	2657	45	2657	40	1.96	0.05	0.1804	0.0044	12.72	0.61	0.511	0.012
6	2678	45	2665	36	2665	38	1.94	0.04	0.1813	0.0042	12.79	0.49	0.515	0.011
6	2680	45	2675	35	2665	38	1.94	0.04	0.1813	0.0042	12.97	0.50	0.516	0.011
7	2724	47	2693	36	2679	40	1.90	0.04	0.1829	0.0044	13.24	0.51	0.526	0.011
7	2623	45	2652	36	2666	39	1.99	0.04	0.1814	0.0043	12.67	0.49	0.502	0.010
GSC 1861														
1	2624	53	2653	44	2654	40	1.99	0.05	0.1801	0.0043	12.64	0.60	0.503	0.012
2	2539	50	2634	44	2687	38	2.07	0.05	0.1838	0.0042	12.42	0.59	0.483	0.012
3	2678	53	2690	45	2683	39	1.94	0.05	0.1833	0.0043	13.17	0.62	0.515	0.012
4	2832	54	2736	45	2681	39	1.81	0.04	0.1831	0.0043	13.79	0.65	0.552	0.013
4	2662	44	2663	35	2672	37	1.96	0.04	0.1821	0.0041	12.76	0.49	0.511	0.010
5	2770	53	2704	45	2667	38	1.86	0.05	0.1815	0.0042	13.34	0.63	0.537	0.013

Grain	^{206}Pb-^{238}U Age	Prop 2SE	^{207}Pb-^{235}U Age	Prop 2SE	^{207}Pb-^{206}Pb Age	Prop 2SE	$^{238}U/^{206}Pb$	Prop 2SE	$^{207}Pb/^{206}Pb$	Prop 2SE	$^{207}Pb/^{235}U$	Prop 2SE	$^{206}Pb/^{238}U$	Prop 2SE
GSC 1861 cont.														
5	2697	43	2682	35	2677	35	1.92	0.04	0.1826	0.0039	13.02	0.49	0.520	0.010
6	2715	45	2688	36	2675	36	1.91	0.04	0.1824	0.0040	13.16	0.50	0.524	0.011
7	2627	43	2659	35	2658	36	1.99	0.04	0.1806	0.0039	12.72	0.48	0.503	0.010
8	2661	43	2688	35	2690	36	1.96	0.04	0.1841	0.0040	13.12	0.49	0.511	0.010
9	2600	53	2631	47	2680	39	2.01	0.05	0.1830	0.0043	12.37	0.60	0.497	0.012
9	2696	43	2699	36	2676	37	1.92	0.04	0.1825	0.0041	13.24	0.50	0.520	0.010
10	2494	52	2596	38	2690	40	2.11	0.06	0.1841	0.0045	11.93	0.59	0.475	0.013
12	2562	43	2621	34	2678	37	2.05	0.04	0.1827	0.0041	12.18	0.46	0.488	0.010
GSC 2775														
1	1156	27	1161	37	1182	72	5.09	0.13	0.0794	0.0029	2.16	0.12	0.197	0.005
4	1171	24	1180	32	1226	70	5.03	0.11	0.0812	0.0029	2.21	0.10	0.199	0.004
5	1157	27	1161	36	1202	66	5.09	0.13	0.0802	0.0027	2.14	0.11	0.197	0.005
5	1199	24	1178	33	1165	73	4.89	0.11	0.0787	0.0029	2.21	0.10	0.205	0.005
6	1206	24	1190	33	1175	70	4.86	0.11	0.0791	0.0028	2.24	0.10	0.206	0.005
7	1148	24	1138	33	1137	74	5.12	0.12	0.0776	0.0029	2.09	0.10	0.195	0.005
8	1173	25	1188	37	1209	88	5.01	0.12	0.0805	0.0036	2.20	0.12	0.200	0.005
9	1150	22	1158	28	1147	56	5.12	0.10	0.0780	0.0022	2.13	0.09	0.195	0.004
10	1167	24	1178	33	1219	70	5.04	0.11	0.0809	0.0029	2.21	0.10	0.199	0.004
11	1169	24	1183	34	1248	74	5.03	0.11	0.0821	0.0031	2.24	0.11	0.199	0.005
12	1155	24	1149	32	1204	71	5.10	0.11	0.0803	0.0029	2.10	0.10	0.196	0.004

Grain	**^{206}Pb-^{238}U Age**	**Prop 2SE**	**^{207}Pb-^{235}U Age**	**Prop 2SE**	**^{207}Pb-^{206}Pb Age**	**Prop 2SE**	**^{238}U/^{206}Pb**	**Prop 2SE**	**^{207}Pb/^{206}Pb**	**Prop 2SE**	**^{207}Pb/^{235}U**	**Prop 2SE**	**^{206}Pb/^{238}U**	**Prop 2SE**
GSC 2908														
28	1775	30	1780	31	1803	41	3.15	0.06	0.1102	0.0025	4.78	0.18	0.317	0.006
29	1723	30	1737	32	1773	44	3.26	0.06	0.1084	0.0026	4.55	0.18	0.307	0.006
30	1766	31	1781	32	1806	43	3.17	0.06	0.1104	0.0026	4.79	0.18	0.315	0.006
34	1789	31	1780	33	1781	42	3.13	0.06	0.1089	0.0025	4.76	0.18	0.320	0.006
37	1785	31	1779	32	1788	42	3.13	0.06	0.1093	0.0025	4.77	0.18	0.319	0.006
38	1772	31	1772	32	1789	42	3.16	0.06	0.1094	0.0025	4.74	0.18	0.317	0.006
39	1769	32	1773	33	1806	44	3.17	0.07	0.1104	0.0027	4.74	0.18	0.316	0.007
1b	1736	33	1760	32	1773	56	3.24	0.07	0.1084	0.0033	4.66	0.18	0.309	0.007
1b	1686	33	1739	31	1784	55	3.34	0.07	0.1091	0.0033	4.55	0.17	0.299	0.007
2b	1582	31	1681	32	1793	56	3.60	0.08	0.1096	0.0034	4.24	0.17	0.278	0.006
2b	1664	32	1735	32	1789	57	3.40	0.07	0.1094	0.0034	4.51	0.17	0.295	0.006
3b	1744	35	1768	34	1813	61	3.22	0.07	0.1108	0.0037	4.72	0.19	0.311	0.007
3b	1638	32	1728	32	1817	57	3.45	0.08	0.1111	0.0035	4.49	0.17	0.290	0.006
4b	1893	41	1836	36	1769	57	2.93	0.07	0.1082	0.0034	5.11	0.21	0.341	0.009
4b	1799	36	1811	34	1799	60	3.11	0.07	0.1100	0.0036	4.96	0.20	0.322	0.007
5b	1796	34	1795	31	1804	54	3.11	0.07	0.1103	0.0033	4.87	0.18	0.322	0.007
5b	1753	33	1765	32	1796	56	3.20	0.07	0.1098	0.0034	4.71	0.18	0.313	0.007
6b	1725	32	1754	31	1787	55	3.26	0.07	0.1093	0.0033	4.65	0.18	0.307	0.007
6b	1756	36	1761	32	1774	57	3.19	0.07	0.1085	0.0034	4.68	0.18	0.313	0.007

Grain	**^{206}Pb-^{238}U Age**	**Prop 2SE**	**^{207}Pb-^{235}U Age**	**Prop 2SE**	**^{207}Pb-^{206}Pb Age**	**Prop 2SE**	**^{238}U/^{206}Pb**	**Prop 2SE**	**^{207}Pb/^{206}Pb**	**Prop 2SE**	**^{207}Pb/^{235}U**	**Prop 2SE**	**^{206}Pb/^{238}U**	**Prop 2SE**
GSC 3345														
1	1802	39	1807	41	1809	43	3.10	0.08	0.1106	0.0026	4.90	0.23	0.323	0.008
2	1847	32	1847	32	1851	42	3.01	0.06	0.1132	0.0026	5.17	0.20	0.332	0.007
3	1828	42	1826	40	1840	47	3.10	0.08	0.1106	0.0026	4.90	0.23	0.323	0.008
3	1846	31	1830	32	1824	39	3.01	0.06	0.1132	0.0026	5.17	0.20	0.332	0.007
4	1777	42	1761	40	1816	49	3.15	0.09	0.1110	0.0030	4.67	0.23	0.318	0.009
4	1840	32	1827	32	1828	41	3.03	0.06	0.1118	0.0025	5.06	0.19	0.330	0.007
5	1767	31	1795	33	1848	42	3.17	0.06	0.1130	0.0026	4.85	0.19	0.315	0.006
6	1810	32	1811	32	1843	42	3.08	0.06	0.1127	0.0026	4.96	0.19	0.324	0.007
7	1750	32	1792	32	1818	54	3.21	0.07	0.1111	0.0033	4.85	0.18	0.312	0.007
7	1686	32	1760	31	1818	54	3.34	0.07	0.1112	0.0033	4.67	0.18	0.299	0.007
7	1844	32	1839	32	1847	42	3.02	0.06	0.1129	0.0026	5.13	0.19	0.331	0.007
1b	1722	32	1767	32	1821	54	3.26	0.07	0.1113	0.0033	4.70	0.18	0.306	0.007
1b	1741	33	1790	32	1824	55	3.22	0.07	0.1115	0.0034	4.83	0.18	0.310	0.007
2b	1815	34	1835	31	1853	56	3.07	0.07	0.1133	0.0035	5.08	0.19	0.325	0.007
2b	1750	34	1795	32	1824	55	3.20	0.07	0.1115	0.0034	4.87	0.19	0.312	0.007
3b	1780	34	1790	31	1819	56	3.14	0.07	0.1112	0.0034	4.84	0.18	0.318	0.007
3b	1772	33	1792	31	1821	54	3.16	0.07	0.1113	0.0033	4.85	0.18	0.317	0.007
5b	1812	34	1824	32	1832	57	3.08	0.07	0.1120	0.0035	5.04	0.19	0.325	0.007
5b	1810	34	1826	31	1858	56	3.09	0.07	0.1136	0.0035	5.07	0.20	0.324	0.007
6b	1738	33	1791	32	1822	55	3.23	0.07	0.1114	0.0034	4.84	0.19	0.310	0.007
6b	1785	34	1797	31	1824	55	3.14	0.07	0.1115	0.0034	4.90	0.19	0.319	0.007

Grain	^{206}Pb-^{238}U Age	Prop 2SE	^{207}Pb-^{235}U Age	Prop 2SE	^{207}Pb-^{206}Pb Age	Prop 2SE	$^{238}U/^{206}Pb$	Prop 2SE	$^{207}Pb/^{206}Pb$	Prop 2SE	$^{207}Pb/^{235}U$	Prop 2SE	$^{206}Pb/^{238}U$	Prop 2SE
GSC 4170														
1	1823	36	1837	33	1859	57	3.06	0.07	0.1137	0.0036	5.11	0.20	0.327	0.007
3	1786	40	1821	42	1856	51	3.13	0.08	0.1135	0.0032	5.04	0.25	0.320	0.008
5	1821	38	1828	40	1840	47	3.06	0.07	0.1125	0.0029	5.05	0.24	0.327	0.008
5	1849	33	1852	33	1872	44	3.01	0.06	0.1145	0.0028	5.19	0.20	0.332	0.007
6	1833	34	1839	34	1856	48	3.04	0.06	0.1135	0.0030	5.13	0.20	0.329	0.007
7	1823	32	1840	33	1875	46	3.06	0.06	0.1147	0.0029	5.13	0.20	0.327	0.007
1b	1821	34	1838	33	1847	54	3.06	0.07	0.1129	0.0034	5.12	0.19	0.327	0.007
3b	1821	34	1827	32	1851	54	3.06	0.06	0.1132	0.0034	5.05	0.19	0.327	0.007
3b	1762	33	1801	31	1840	55	3.18	0.07	0.1125	0.0034	4.91	0.19	0.315	0.007
4b	1858	35	1855	33	1851	57	2.99	0.06	0.1132	0.0036	5.21	0.20	0.334	0.007
4b	1817	35	1836	31	1853	56	3.07	0.07	0.1133	0.0035	5.12	0.20	0.326	0.007
5b	1833	35	1874	34	1889	58	3.04	0.07	0.1156	0.0037	5.34	0.21	0.329	0.007
5b	1843	35	1852	33	1883	56	3.02	0.07	0.1152	0.0036	5.20	0.20	0.331	0.007
6b	1803	34	1827	32	1841	55	3.10	0.07	0.1125	0.0034	5.06	0.19	0.323	0.007
6b	1842	37	1830	34	1840	60	3.03	0.07	0.1125	0.0037	5.08	0.20	0.330	0.008

b indicates grains from a different mount

Chapter 4. Discussion

4.1 Signal loss during LASS

In order to quantify the proportion of ablated material sent to each mass spectrometer, we attempted to use the Nd signal intensities of a LREE glass of known Nd concentration [*Fisher et al*., 2011] measured simultaneously on both the Element and Neptune. However, attempts have demonstrated a complicated inter-play of gas flows/tuning conditions during LASS analyses which precluded an accurate quantification of the proportion of material sent to each mass spectrometer. In order to overcome this, we compare the signal intensity for LASS mode and "Nd only" mode analyses, each optimally tuned for maximum Nd signal intensity. The results of this comparison are shown in Figure 4-1, and demonstrate that even with optimal tuning there appears to be little signal loss (~14%) between LASS and "Nd only" mode, despite the fact that material is split between the two mass spectrometers. Similar observations have been made for LASS Lu-Hf+ U-Pb analyses [pers. comm., C. Fisher]. This experiment was carried out by C. Fisher at Washington State University using similar equipment to the setup presented in this thesis, due to instrument maintenance at Memorial at the time.

4.2 Assessment of precision and accuracy of measured Pb-Pb ages of the monazite standards

In general, an assessment of the monazite U-Pb data demonstrated that the LASS method presented in this study provides an accurate method for determining $^{207}Pb/^{206}Pb$ ages. Six of the seven samples have weighted mean $^{207}Pb/^{206}Pb$ LASS ages agree within 2σ uncertainty of the high precision ID-TIMS ages. The sample that is not in agreement is

GSC-4170 which is ~1.2% greater than the ID-TIMS age, plotting just outside of the analytical uncertainty. A BSE image of a selected GSC 4170 grain (Figure 3-11F) shows that these grains have complex internal zoning, which was likely the cause for inaccurate LASS age for this sample. Data are generally presented as $^{207}Pb/^{206}Pb$ ages rather than $^{206}Pb/^{238}U$ or $^{207}Pb/^{235}U$ ages as there remains uncorrected elemental fractionation in the majority of these samples, as $^{207}Pb/^{206}Pb$ ages are less impacted by elemental fractionation. This fractionation is seen as the horizontal trend of the ellipses on a TW concordia diagram (e.g. Figure 3-3A). The LASS setup requires a higher laser power than dedicated U-Pb work to ensure enough sensitivity for precise Sm-Nd results. The $^{206}Pb/^{238}U$ LASS age for the younger sample 93-GD-12 falls just outside the analytical uncertainty of the ID-TIMS age. This is likely due to elemental fractionation affecting the U-Pb age as this sample is too young for the accurate determination of a $^{207}Pb/^{206}Pb$ age.

While ^{232}Th-^{208}Pb ages were also obtained from the LASS analyses, there was no reliable Th-Pb age for the U-Pb standard used (Trebilcock) and therefore the accuracy of these ages could not be corrected or verified. *Liu et al*., [2012] discussed problems associated with Th-Pb ages, as their Th-Pb ages were generally older than the associated U-Pb ages. They suggested discordance in the U-Th-Pb system and false assumption of the Th-Pb age of the standard as likely causes of Th-Pb age bias.

Additionally, four of the six GSC samples had Sm-Nd LASS isochron ages (although with very large uncertainties) that overlapped the ID-TIMS Pb/Pb ages presented by *Stern and Berman* [2001], with one sample (GSC-3345) having an age just outside the ID-TIMS age. The Sm-Nd isochron for sample GSC-4170; however, gives an age that is far too young when compared to the U-Pb LASS ages or ID-TIMS ages. The

Sm-Nd isochron for this sample (Fig. 3-8D) shows an abnormal pattern, which was likely the cause of the inaccurate isochron age for this sample. The monazite grains in GSC-4170 displayed a great deal of patchy zoning (Fig. 3-11F) that was the likely cause of this abnormal pattern. While Sm-Nd isochron ages can help verify U-Pb ages, it is important to consider that isochron ages often have very large uncertainties due to the typically small spread of Sm-Nd values seen naturally in monazite. However it is important to note that while a portion of these samples did not show much spread in Sm-Nd, they were not entirely homogenous in Sm-Nd ratios. It is also important to note that while monazite Sm-Nd isochrons yield highly imprecise ages, additional analyses of cogenetic minerals with higher or lower Sm/Nd (e.g., apatite, titanite) are expected to greatly improve the precision of Sm-Nd isochrons [*McFarlane and McCulloch*, 2007].

The Eu* and Ce/Gd LASS results for the GSC monazites and Trebilcock standard are shown in Figure 3-9B. As displayed in this Figure, Eu* and Ce/Gd can exhibit high variance from sample to sample, while having low variance within an individual sample. These tendencies in REE values can make Eu* and Ce/Gd useful tools when investigating sample variation and source tracing.

4.3 Assessment of Sm-Nd in KMO3-72

As discussed in section 3.1 ID-TIMS analyses were done on KMO3-72, an in-house reference material, to assess the accuracy of the Sm-Nd results provided by the LASS study. KMO3-72 was chosen for these analyses rather than a GSC sample because there was more available material. These ID-TIMS results provide a means of comparing our LASS Sm-Nd data with more precise ID-TIMS data. A comparison of the ID-TIMS

Sm-Nd data with the LASS data is shown in Figure 3-1C, which shows that both the LASS points and the ID-TIMS points fall in one cluster of data, and the majority of the data points lie along the 1822 Ma reference isochron within uncertainty. The inset on Figure 3-1C shows a weighted mean initial $^{143}Nd/^{144}Nd$ plot for the LASS and ID-TIMS data. All data points from the LASS and all ID-TIMS points minus one agree with the weighted mean initial $^{143}Nd/^{144}Nd$ value within uncertainty. These two observations help reinforce the accuracy of the LASS method for Sm-Nd analyses.

4.4 Possibilities for future work

Further efforts in optimizing the LASS methodology and data reduction in order to reduce or eliminate any elemental fractionation are vital for obtaining more precise and accurate U-Pb ages in future studies.

Currently available monazite reference materials (e.g., Trebilcock; [*Tomascak et al*., 1996; *McFarlane and McCulloch*, 2007; *Fisher et al*., 2011].) are not as well-studied as some of the widely used zircon reference materials (e.g., 91500; [*Wiedenbeck et al.*, 2004]) as there has been less work done on monazite than zircon, so future work on developing better reference materials for monazite would improve data quality and our ability to evaluate the precision and accuracy of U-Pb and Sm-Nd monazite data. Also, this study required two distinct reference materials: one for reducing the U-Pb data; and one for reducing the Sm-Nd data. If a reference material could be found that works for both systems, it would simplify data acquisition and processing. Recently, *Liu et al.*, [2012] showed that both the Manantagoutry monazite and Namaqualand monazite are relatively homogenous in both the U-Th-Pb and Sm-Nd systems, and suggested that they

could potentially be used effectively as standards for LASS monazite studies. However, Manantagoutry monazite appears to be complex and its homogeneity varies in different pieces, as seen in the study of *Kylander-Clark et al.*, [2013] where Manantagoutry was the only standard analyzed whose laser ablation U-Pb ages differed from ID-TIMS values by >1%. Any potential monazite reference material would have to be abundant and widely available for distribution, and be thoroughly characterized using BSE imaging, elemental X-ray maps, as well as ID-TIMS and in situ Sm-Nd and U-Pb isotopic measurements.

The LASS method presented here could potentially be extended to other minerals which have high REE and U content, such as allanite, titanite or apatite provided they are old enough to have produced enough measurable radiogenic Pb to yield precise ages. However these minerals generally contain high amounts of common Pb, so any analyses of these minerals would require an accurate common Pb correction. A recent study, [*Chew et al.*, 2014], presents a general approach to common Pb corrections for U-Pb LA-ICP-MS analyses of minerals like those mentioned above.

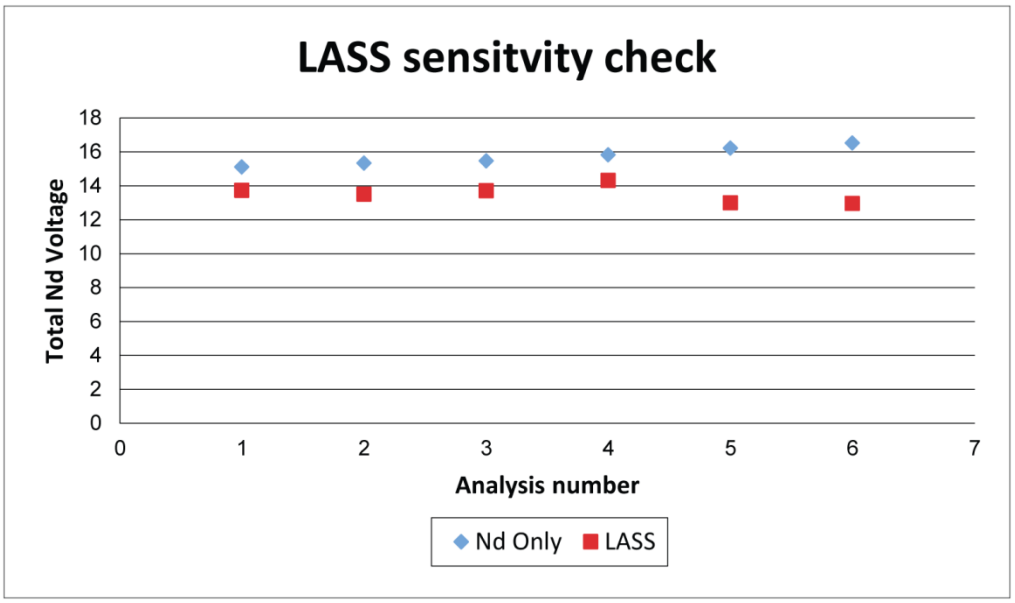

Figure 4-1: Comparison of total Nd voltage of LASS analyses and Nd Only analyses

Chapter 5. Birch Creek Pluton case study

5.1 Birch Creek Pluton

Monazite grains from the Birch Creek Pluton (BCP) were included in this study to demonstrate, as a case study, a potential application of LASS U-Pb, Sm-Nd, and REE measurements in monazite. The BCP is located in the White Mountains in southeastern California and is a two-mica granite [*Barton*, 2000; *Ayers et al*., 2006]. By combining Th-Pb dating with O isotope data in monazite, *Ayers et al*. [2006] were able to identify hydrothermal alteration of the monazite in nearby country rocks, caused by the intrusion of the BCP, by demonstrating that the altered country rock monazite had the same age and O isotope signature as the BCP samples. They also suggested that monazite could be useful for mapping the extent of hydrothermal alteration. The main objective of applying the LASS method to this case study was to test the response of Sm-Nd in monazite to hydrothermal alteration. Additionally, some of the BCP monazite grains underwent high-precision ID-TIMS U-Pb dating at Boise State University for this study.

The BCP is Cretaceous age and is composed of two large units, the Border Suite (BS) and Central Suite (CS), which intruded into Late Proterozoic and Early Cambrian metasedimentary rocks (Figure 5-1). Samples from the Deep Springs Formation included a sandstone (DU-1) and a quartzite (Dma-1). For this case study, monazite grains from each of BS1 and 2, CS1 and 2, DU-1, and Dma-1 were analyzed using the LASS setup. *Ayers et al*. [2006] showed that monazite from the BCP (i.e., BS and CS) had an average Th-Pb age of 78.0 ± 0.7 Ma and $\delta^{18}O$ value of 8.7 ± 0.2‰, which is identical within uncertainty to monazite found in country rock within the hydrothermal aureole (sample

Dma-1). Conversely, monazite sample DU-1 collected from just outside the hydrothermal aureole was apparently unaffected by any hydrothermal alteration and retained an age range of ~820–1070 Ma and $\delta^{18}O$ values of ~3.5–6.5‰. Based on these finding, the authors suggested that the intrusion of the BCP also caused partial dissolution-precipitation of the monazite from Dma-1, resulting in a complete resetting of the U-Th-Pb system. Most of the monazite grains in Dma-1 showed similar ages and $\delta^{18}O$ values to BS and CS; however, a small population of monazite from Dma-1 had Th-Pb ages of approximately 340 Ma and intermediate $\delta^{18}O$ values of around 7.0‰, which they suggested was the result of incomplete recrystallization and resetting of the U-Th-Pb system [*Ayers et al.*, 2006].

5.2.1 Birch Creek Pluton results

Grains from BS, CS, DU-1, and Dma-1 were analyzed using the LASS method for Sm-Nd and U-Pb; full results are presented in Tables 5-1 and 5-2. Figure 5-2A shows a U-Pb TW concordia diagram of all BCP samples (BS1, BS2, CS1, and CS2) with the blue uncertainty ellipses representing samples BS1 and BS2 and the green uncertainty ellipses representing samples CS1 and CS2. The weighted mean 207corrected $^{206}Pb/^{238}U$ age for the BS samples is 89.1 ± 2.3Ma, (2σ, MSWD=1.5, based on 9 of 11 analyses) and the weighted mean 207corrected $^{206}Pb/^{238}U$ age for the CS samples is 89.6 ± 3.2Ma, (2σ, MSWD=2.5, based on 9 of 10 analyses).

The altered quartzite sample, Dma-1, shows two distinct age populations, as previously shown by *Ayers et al.* [2006]. The U-Pb concordia diagram for the young

population of Dma-1 can be seen as Figure 5-2C, with a weighted mean $^{206}Pb/^{238}U$ age of 87.4 ± 1.7 Ma (2σ, MSWD = 2.0), consistent with LASS U-Pb results for BS and CS. The older population of Dma-1 and gives concordant ages (Fig. 5-2B) ranging from ~330-380 Ma, comprised of 4 analyses on 3 separate grains. The unaltered sandstone sample, DU-1, has LASS $^{207}Pb/^{206}Pb$ ages ranging from 803.2 Ma to 1174.6 Ma (Figure 5-2D). The high MSWDs for samples BS, CS and Dma-1 (young) likely represent an underestimation of the errors for these samples.

The BCP samples (BS-1, BS-2, CS-1, CS-2) has a mean $^{143}Nd/^{144}Nd$ (present day) value of 0.511604 ± 0.000092 (2 S.D.). The $^{147}Sm/^{144}Nd$ ranges from 0.0595 to 0.0859, and Eu* ranges from 0.148 to 0.494 and Ce/Gd ranges from 28.20 to 64.38.

The young population of Dma-1 has a mean $^{143}Nd/^{144}Nd$ (present day) value of 0.511536 ± 0.000043 (2 S.D.) and has a $^{147}Sm/^{144}Nd$ range of 0.0640 to 0.1128. The Eu* ranges from 0.187 to 0.540, and the Ce/Gd ranged from 14.34 to 49.10 for the young population of Dma-1. The small older population of Dma-1 has mean $^{143}Nd/^{144}Nd$ and $^{145}Nd/^{144}Nd$ values of 0.512288 ± 0.000065 (2 S.D.) and 0.348443 ± 0.000054 (2 S.D.), respectively. The Sm-Nd for this population ranges from 0.0920 to 0.1236, and the Eu* ranges from 0.103 to 0.161 while the Ce/Gd ranges from 13.26 to 26.70.

The sandstone sample, DU-1, has $^{143}Nd/^{144}Nd$ values ranging from 0.511249 to 0.511486. The $^{147}Sm/^{144}Nd$ in this sample ranges from 0.0682 to 0.1063, the Eu* values range from 0.028 to 0.135 and the Ce/Gd ranges from 16.48 to 40.70.

A compilation of the Sm-Nd results for the various Birch Creek samples (Figure 5-3A) shows the general trend of present $^{147}Sm/^{144}Nd$ and $^{143}Nd/^{144}Nd$ values for each sample whereas Figure 5-3B shows a compilation of initial Nd isotopic values for each

BCP sample. Figure 5-3C shows REE behaviour for the BCP samples and both populations of Dma-1. The LASS results for these samples are reported in Tables 5-1 and 5-2.

5.2.2 Birch Creek Pluton ID-TIMS results

Methodology for these ID-TIMS analyses is outlined in Appendix A. The $^{207}Pb/^{235}U$ date is the best estimate for crystallization age in Phanerozoic monazite due to initial Th-U disequilibrium that causes the $^{206}Pb/^{238}U$ date to be older than crystallization by up to several million years [*Schärer,* 1984; *Parrish,* 1990]. Uncertainty on the $^{207}Pb/^{235}U$ date is given as ± x / y / z Ma, where x is the internal uncertainty, y includes the uncertainty in the tracer calibration, and z includes the uncertainties in the tracer calibration and ^{235}U decay constant. Four grains from sample BS1 yielded a weighted mean $^{207}Pb/^{235}U$ date of 82.99 ± 0.22 / 0.24 / 0.26 Ma (MSWD = 1.1) (Fig. 5-4, appendix Table B-4). Three grains from sample BS2 yielded a weighted mean $^{207}Pb/^{235}U$ date of 83.04 ± 0.26 / 0.27 / 0.29 Ma (MSWD = 0.5). One other grain is older with $^{207}Pb/^{235}U$ date of 83.80 ± 0.19 Ma. The seven youngest grains from BS1 and BS2 yielded a weighted mean $^{207}Pb/^{235}U$ date of 83.01 ± 0.17 / 0.19 / 0.22 Ma (MSWD = 0.8). Six grains from sample Dma-1 yielded a weighted mean $^{207}Pb/^{235}U$ date of 83.54 ± 0.16 / 0.18 / 0.21 Ma (MSWD = 0.9). One other grain is older with $^{207}Pb/^{235}U$ date of 110.7 ± 0.6 Ma. The $^{207}Pb/^{235}U$ dates from LASS are not used because they are too inaccurate. The LASS $^{206}Pb/^{238}U$ dates are older than the ID-TIMS $^{207}Pb/^{235}U$ dates by ~5%, which is likely due to a combination of the analytical uncertainty associated with LASS dates (typically ~2-3%) and initial Th-U disequilibrium in the $^{206}Pb/^{238}U$ system.

5.3 Birch Creek case study discussion

The purpose of this case study was to determine the utility of the LASS method on well-studied samples, to evaluate its ability to determine the in situ response of the Sm-Nd and U-Pb systems in monazite to hydrothermal fluid alteration. As such, monazite grains from BCP (samples BS1-2, CS1-2) were compared with the altered country rock monazite from sample Dma-1. LASS U-Pb results for Dma-1 (Figs. 5-2B and 5-2C) identified two distinct age populations within Dma-1: one with a weighted mean $^{206}Pb/^{238}U$ age of 87.4 ± 1.7 Ma (2σ), which overlap the BCP age, and an older population composed of 3 grains (4 analyses) with concordant ages ranging from ~330Ma to ~380Ma. *Ayers et al.* [2006] linked the younger monazite population of Dma-1 to the BCP based on similar Th-Pb ages and $\delta^{18}O$ values. This connection is now strengthened by the very similar initial Nd isotope compositions for monazite from the pluton and the younger population of Dma-1. The hypothesis of *Ayers et al.* [2006] is that the younger population of Dma-1 monazite underwent simultaneous dissolution-reprecipitation under the influence of hydrothermal fluids from the BCP, resetting their Th-Pb as the older population of Dma-1 underwent incomplete resetting of the Th-Pb system. However, new LASS U-Pb and Sm-Nd data suggests that that the young population of monazite in the altered sample (Dma-1) could be newly grown via precipitation from the pluton derived fluid.

The formation of these monazites by new growth is supported by their Sm-Nd isotopic composition and initial Nd values being nearly identical to the BCP in addition to LASS U-Pb data showing that the older grains of Dma-1 are concordant, indicating that

they could not have undergone partial resetting of their U-Th-Pb system. The fact that this older age population of Dma-1 is concordant is important, as it means this is likely a true age and not the result of partial lead loss. *Ayers et al.*, [2006] could not check for concordance, as they only had a single geochronometer, Th-Pb ages. This ~330-380 Ma population of Dma-1 also has unique Sm-Nd isotopic composition when compared with the younger monazite from Dma-1 (Figure 5-3A), and thus distinct initial $^{143}Nd/^{144}Nd$ (Figure 5-3B). However, this population has a small sample size, with only 4 analyses so it is difficult to draw any definitive conclusions. It is possible that a combination of both mechanisms (dissolution-reprecipitation and new growth) influenced the formation of these monazites. $^{206}Pb/^{238}U$ LASS ages for the BCP samples (BS and CS) and the young population of Dma-1 are still ~4-5% higher than the high precision ID-TIMS ages for these samples. This is likely due to a combination of the analytical uncertainty of the LASS method and remaining uncorrected elemental fractionation as these samples are too young for accurate determinations of $^{207}Pb/^{206}Pb$ ages.

U-Pb ages for the DU-1 sandstone represent partially reset detrital ages. The slight overlap in Sm-Nd isotope composition of monazite from this unaltered sample and the other BCP samples (Figure 5-3A) suggests a similar source for some of the monazite in these samples.

Figure 5-3C shows Ce/Gd plotted against Eu* for both BCP samples and both populations of Dma-1. This figure shows a general linear pattern of the REE in these samples. The REE data for the young population of monazites from Dma-1 generally overlap the BCP samples, whereas the older population of Dma-1 plot have lower Ce/Gd and Eu*. These REE data reaffirms the existence of two distinct populations of Dma-1

and support the conclusions drawn from the Sm-Nd and initial Nd data. The REE concentrations provided by the LASS method can be another useful tool when studying the effects of hydrothermal fluids on monazites.

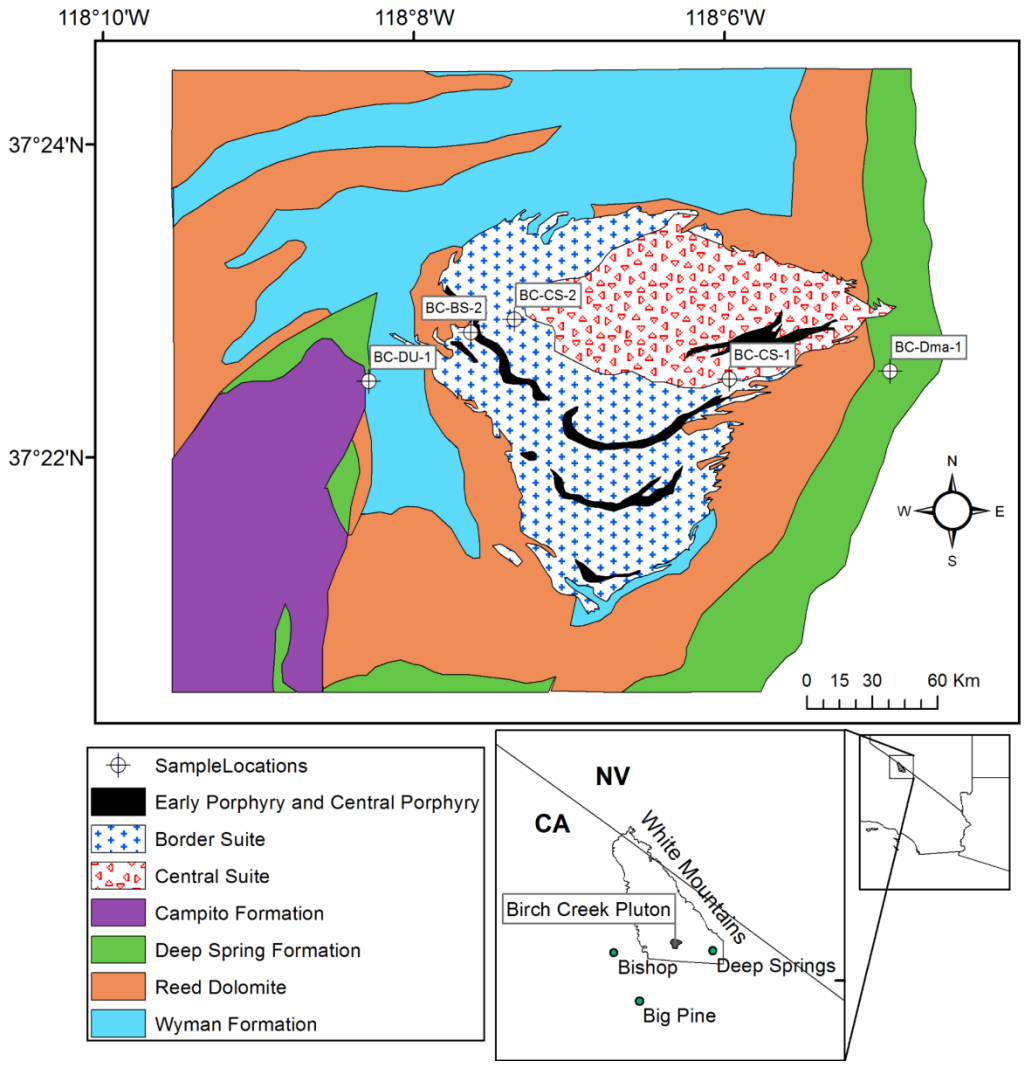

Figure 5-1: Map of the Birch Creek Pluton and surrounding rock units, after *Ayers et al*., [2006].

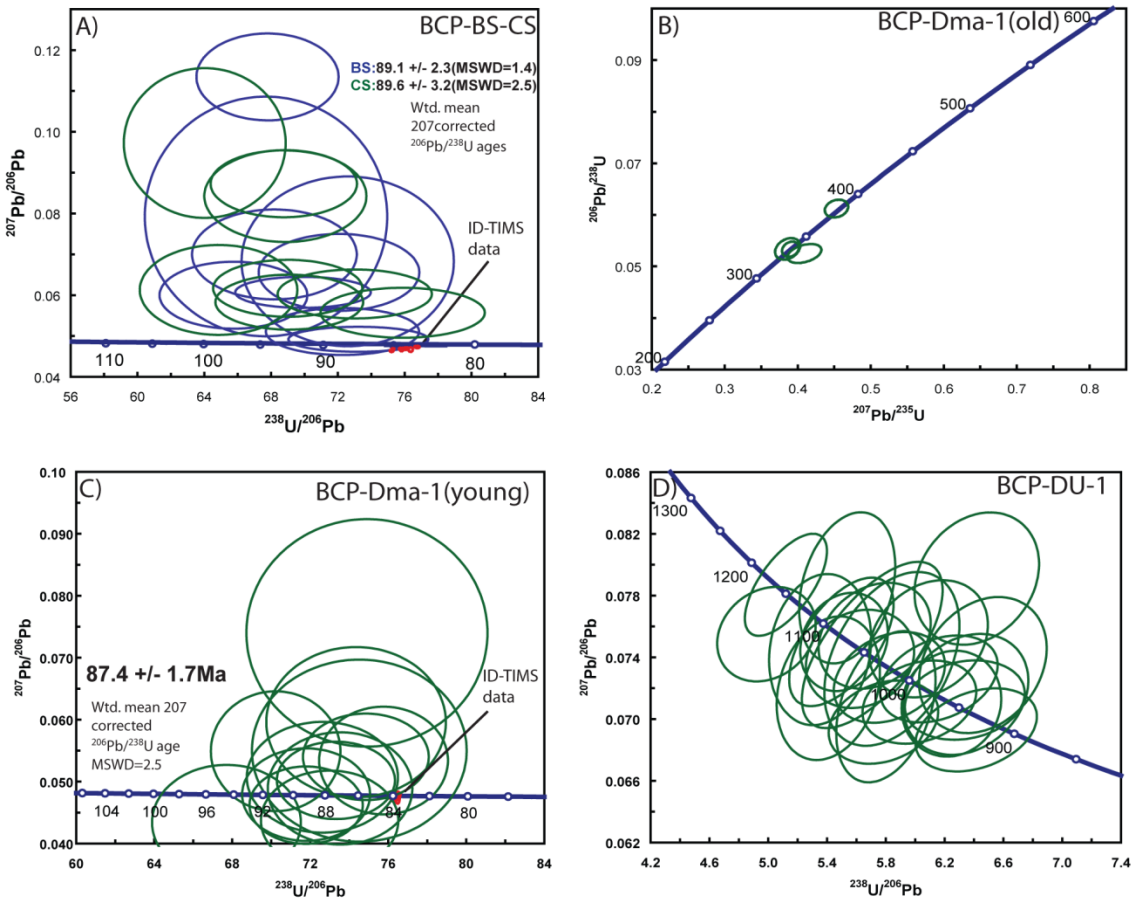

Figure 5-2: LASS results for BCP and related samples. **A)** U-Pb TW concordia for BS-1, BS-2, CS-1 and CS-2, with displayed $^{206}Pb/^{238}U$ weighted mean age. Blue ellipses represent BS-1 and BS-2 while green ellipses represent CS-1 and CS-2. Red circles display ID-TIMS data for these samples. **B)** U-Pb concordia for the older unaltered population of Dm-1. **C)** U-Pb TW concordia for the young altered population of Dma-1, with displayed $^{206}Pb/^{238}U$ weighted mean age. Red circles represent ID-TIMS data. **D)** U-Pb TW concordia for unaltered DU-1.

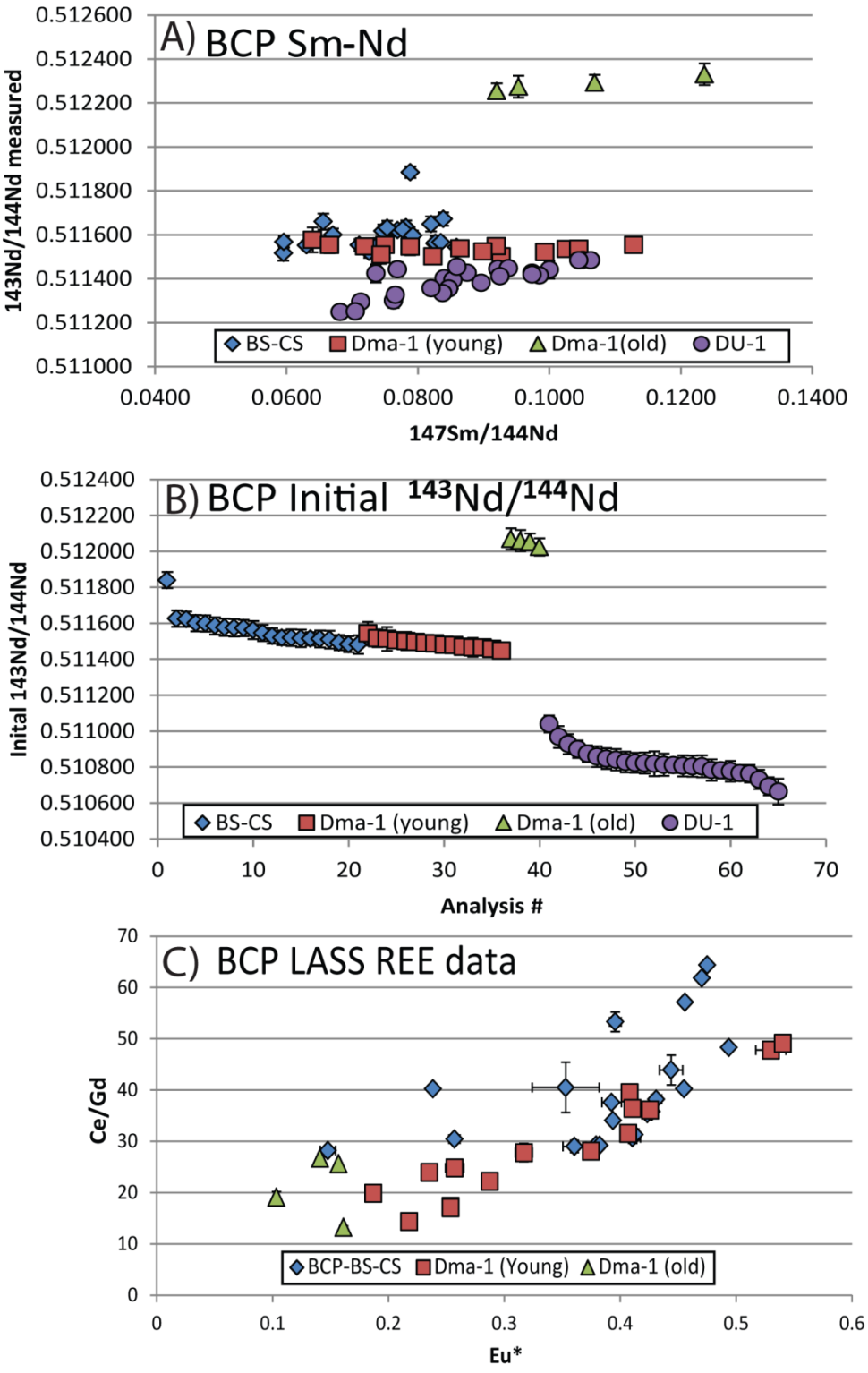

Figure 5-3: A) Sm-Nd (present day) for the BCP and related samples. **B)** Initial Nd isotopic concentration for the BCP and related samples. **C)** LASS REE data for the BCP and related samples. ID-TIMS U-Pb results for BCP samples (BS1, BS2 and Dma-1).

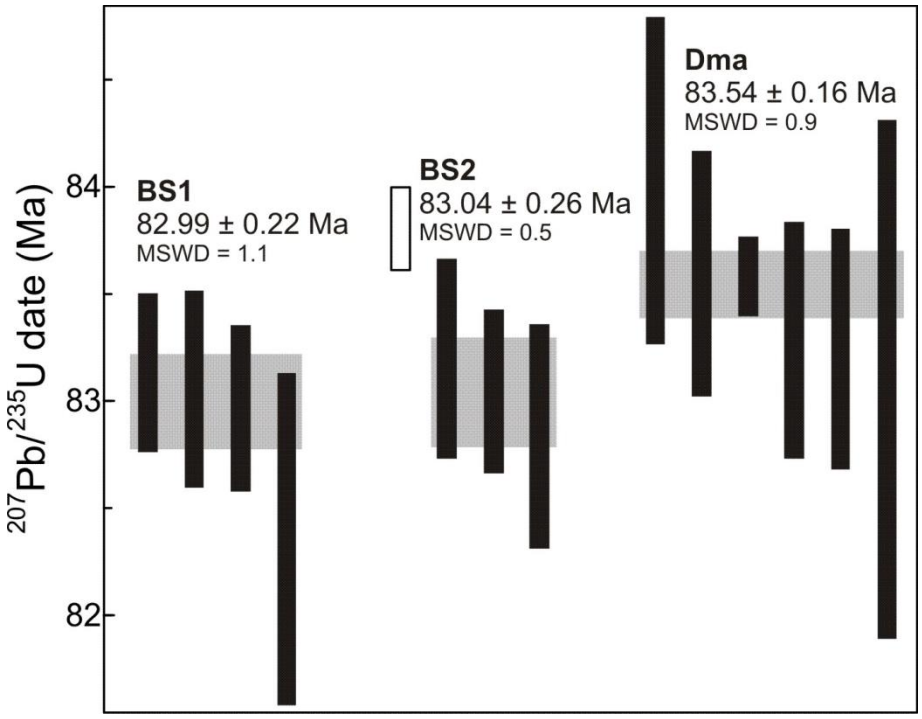

Figure 5-4: ID-TIMS ranked age plot for BCP and related samples (BS1, BS2 and Dma-1). Grey areas represent the mean values and uncertainties for each sample. The white bar for BS2 represents analysis which falls outside of this mean value, even within uncertainties.

Table 5-1: LASS Sm-Nd results for BCP and related samples

Grain	$^{143}Nd/^{144}Nd$	2SE	$^{147}Sm/^{144}Nd$	Prop uncertainty	$^{145}Nd/^{144}Nd$	2SE	$^{143}Nd/^{144}Nd$ Initial	Prop uncertainty	εNd(i)	Eu*	2SE	Ce/Gd	2SE	$\delta^{18}O^{1}$
BS-1														
1	0.511601	0.000028	0.0671	0.0002	0.348423	0.000018	0.511562	0.000050	-18.6	0.494	0.002	48.31	0.45	8.4
1	0.511649	0.000034	0.0820	0.0015	0.348439	0.000017	0.511600	0.000046	-17.8	0.411	0.007	30.70	1.10	8.4
9	0.511554	0.000027	0.0711	0.0020	0.348442	0.000024	0.511509	0.000050	-19.5	0.444	0.010	43.90	2.90	9.1
9	0.511517	0.000034	0.0595	0.0001	0.348421	0.000024	0.511483	0.000045	-20.2	0.475	0.0006	64.38	0.46	9.1
15	0.511621	0.000025	0.0769	0.0010	0.348432	0.000021	0.511575	0.000048	-18.3	0.427	0.002	35.78	0.72	9.5
16	0.511634	0.000031	0.0782	0.0066	0.348449	0.000022	0.511599	0.000046	-18.4	0.353	0.029	40.50	4.90	8.8
20	0.511523	0.000027	0.0726	0.0001	0.348421	0.000020	0.511481	0.000051	-20.2	0.239	0.0003	40.23	0.19	9.4
BS-2														
1	0.511660	0.000036	0.0656	0.0012	0.348437	0.000017	0.511623	0.000043	-17.5	0.396	0.005	53.30	1.90	8.8
2	0.511560	0.000022	0.0826	0.0016	0.348433	0.000017	0.511513	0.000047	-19.6	0.413	0.004	31.30	1.10	8.6
3	0.511618	0.000029	0.0747	0.0007	0.348445	0.000022	0.511573	0.000045	-18.3	0.431	0.005	38.22	0.86	9.1
7	0.511885	0.000026	0.0789	0.0003	0.348440	0.000022	0.511840	0.000044	-13.2	0.257	0.005	30.43	0.27	8.5
CS-1														
1	0.511624	0.000025	0.0777	0.0006	0.348436	0.000013	0.511577	0.000048	-18.2	0.424	0.003	35.38	0.83	8.7
2	0.511564	0.000031	0.0827	0.0008	0.348444	0.000014	0.511516	0.000049	-19.5	0.379	0.002	29.26	0.64	8.2
4	0.511632	0.000032	0.0753	0.0005	0.348431	0.000020	0.511585	0.000047	-18.0	0.393	0.008	37.61	0.58	8.5
7	0.511672	0.000030	0.0839	0.0004	0.348441	0.000017	0.511626	0.000045	-17.5	0.148	0.007	28.20	0.42	10.1
8	0.511568	0.000026	0.0596	0.0001	0.348437	0.000017	0.511529	0.000043	-19.0	0.470	0.0005	61.84	0.15	8.9

Grain	$^{143}Nd/^{144}Nd$	2SE	$^{147}Sm/^{144}Nd$	Prop Uncertainty	$^{145}Nd/^{144}Nd$	2SE	$^{143}Nd/^{144}Nd$ Initial	Prop Uncertainty	εNd(i)	Eu*	2SE	Ce/Gd	2SE	$\delta^{18}O^{1}$
CS-2														
1	0.511597	0.000022	0.0792	0.0002	0.348442	0.000014	0.511546	0.000046	-18.7	0.394	0.003	34.08	0.14	8.7
2	0.511544	0.000027	0.0859	0.0020	0.348433	0.000020	0.511492	0.000042	-19.9	0.361	0.010	29.00	1.20	8.3
3	0.511553	0.000020	0.0631	0.0003	0.348443	0.000021	0.511520	0.000040	-19.7	0.456	0.0007	57.16	0.62	8.6
4	0.511567	0.000017	0.0835	0.0003	0.348422	0.000022	0.511519	0.000046	-19.5	0.382	0.003	29.20	0.20	9.1
5	0.511557	0.000028	0.0740	0.0003	0.348445	0.000020	0.511514	0.000037	-19.6	0.455	0.003	40.25	0.41	8.8
Dma-1 (young)														
4	0.511547	0.000027	0.0719	0.0002	0.348421	0.000024	0.511505	0.000042	-19.7	0.408	0.002	39.46	0.13	10.5
5	0.511502	0.000030	0.0927	0.0006	0.348433	0.000019	0.511448	0.000044	-20.8	0.287	0.001	22.24	0.25	9.7
6	0.511554	0.000058	0.0750	0.0008	0.348461	0.000074	0.511513	0.000066	-19.7	0.426	0.001	36.10	1.10	9.3
7	0.511502	0.000032	0.0823	0.0004	0.348436	0.000025	0.511457	0.000045	-20.8	0.375	0.002	28.09	0.30	8.9
8	0.511538	0.000028	0.0864	0.0023	0.348430	0.000038	0.511489	0.000042	-20.1	0.317	0.007	27.80	1.80	9.3
9	0.511546	0.000039	0.0788	0.0006	0.348431	0.000026	0.511501	0.000050	-19.8	0.407	0.003	31.58	0.66	7.9
13	0.511510	0.000042	0.0744	0.0003	0.348426	0.000029	0.511466	0.000053	-20.4	0.411	0.004	36.39	0.31	9.8
14	0.511577	0.000057	0.0640	0.0010	0.348459	0.000020	0.511542	0.000065	-19.2	0.530	0.013	47.80	1.10	7.8
14	0.511554	0.000037	0.0665	0.0007	0.348440	0.000023	0.511517	0.000049	-19.6	0.540	0.007	49.10	1.60	7.8
15	0.511535	0.000029	0.1026	0.0011	0.348448	0.000016	0.511478	0.000043	-20.4	0.254	0.001	17.32	0.38	8.9
15	0.511554	0.000024	0.1128	0.0005	0.348441	0.000022	0.511488	0.000040	-20.0	0.218	0.002	14.34	0.13	8.9
16	0.511537	0.000018	0.1045	0.0009	0.348453	0.000017	0.511479	0.000037	-20.3	0.254	0.001	17.06	0.33	9.0
16	0.511521	0.000031	0.0993	0.0003	0.348423	0.000025	0.511465	0.000045	-20.6	0.187	0.004	19.85	0.17	9.0
17	0.511549	0.000019	0.0920	0.0009	0.348419	0.000018	0.511496	0.000037	-19.9	0.235	0.001	23.94	0.66	8.9
17	0.511524	0.000031	0.0899	0.0012	0.348445	0.000023	0.511468	0.000044	-20.3	0.257	0.008	24.82	0.79	8.9

Grain	$^{143}Nd/^{144}Nd$	2SE	$^{147}Sm/^{144}Nd$	Prop Uncertainty	$^{145}Nd/^{144}Nd$	2SE	$^{143}Nd/^{144}Nd$ Initial	Prop Uncertainty	εNd(i)	Eu*	2SE	Ce/Gd	2SE	$\delta^{18}O^{1}$
Dma-1 (old)														
1	0.512255	0.000034	0.0920	0.0015	0.348420	0.000017	0.512053	0.000047	-2.8	0.141	0.002	26.70	0.91	8.7
12	0.512274	0.000050	0.0953	0.0013	0.348481	0.000032	0.512069	0.000059	-2.7	0.157	0.012	25.63	0.73	6.5
19	0.512331	0.000050	0.1236	0.0010	0.348443	0.000034	0.512059	0.000060	-2.7	0.161	0.003	13.26	0.13	7.3
19	0.512293	0.000036	0.1069	0.0068	0.348428	0.000012	0.512025	0.000048	-2.2	0.103	0.005	19.10	2.20	7.3
DU-1														
1	0.511402	0.000028	0.0840	0.0033	0.348420	0.000028	0.510874	0.000047	-10.2	0.077	0.016	28.10	2.30	5.5
1	0.511301	0.000033	0.0763	0.0009	0.348440	0.000044	0.510900	0.000048	-13.6	0.076	0.002	33.23	0.73	5.5
2	0.511486	0.000023	0.1051	0.0005	0.348451	0.000018	0.510693	0.000050	-8.9	0.108	0.003	16.48	0.23	5.3
4	0.511427	0.000016	0.0875	0.0010	0.348437	0.000023	0.510810	0.000043	-8.5	0.083	0.005	24.80	0.80	4.4
5	0.511296	0.000019	0.0713	0.0008	0.348436	0.000029	0.510781	0.000044	-8.4	0.036	0.001	40.70	1.10	4.9
5	0.511249	0.000022	0.0682	0.0001	0.348422	0.000030	0.510766	0.000045	-9.2	0.034	0.0003	33.28	0.25	4.9
6	0.511395	0.000040	0.0853	0.0009	0.348468	0.000037	0.510813	0.000062	-9.3	0.043	0.0008	26.92	0.40	N/A
19	0.511484	0.000029	0.1063	0.0015	0.348429	0.000025	0.511040	0.000047	-15.0	0.072	0.007	18.74	0.40	4.8
20	0.511425	0.000041	0.0736	0.0039	0.348430	0.000030	0.510928	0.000056	-7.3	0.057	0.007	35.10	4.60	5.4
21	0.511382	0.000029	0.0896	0.0005	0.348437	0.000015	0.510731	0.000053	-9.2	0.043	0.0002	25.62	0.33	6.2
22	0.511355	0.000027	0.0847	0.0002	0.348428	0.000019	0.510763	0.000049	-9.6	0.070	0.002	25.70	0.07	5.5
23	0.511427	0.000030	0.0974	0.0029	0.348446	0.000018	0.510776	0.000058	-10.6	0.028	0.0006	21.70	1.60	5.8
2	0.511445	0.000044	0.0922	0.0005	0.348449	0.000043	0.510818	0.000070	-9.3	0.099	0.0008	22.13	0.27	5.3
4	0.511454	0.000023	0.0859	0.0004	0.348440	0.000018	0.510858	0.000058	-8.0	0.053	0.0008	26.85	0.26	4.4
5	0.511327	0.000032	0.0766	0.0003	0.348450	0.000037	0.510840	0.000060	-10.6	0.035	0.002	35.51	0.62	4.9
19	0.511484	0.000028	0.1045	0.0022	0.348430	0.000031	0.510804	0.000062	-10.7	0.048	0.002	18.99	0.78	4.8

Grain	$^{143}Nd/^{144}Nd$	2SE	$^{147}Sm/^{144}Nd$	Prop Uncertainty	$^{145}Nd/^{144}Nd$	2SE	$^{143}Nd/^{144}Nd$ Initial	Prop Uncertainty	εNd(i)	Eu*	2SE	Ce/Gd	2SE	$\delta^{18}O^{1}$
DU-1 (cont.)														
20	0.511443	0.000033	0.0769	0.0024	0.348466	0.000035	0.510967	0.000060	-8.7	0.082	0.008	32.30	2.30	5.4
21	0.511441	0.000041	0.1000	0.0034	0.348437	0.000016	0.510664	0.000072	-8.6	0.039	0.001	21.60	1.20	6.2
22	0.511335	0.000027	0.0838	0.0002	0.348437	0.000024	0.510828	0.000058	-12.0	0.056	0.002	26.17	0.14	5.5
23	0.511357	0.000027	0.0820	0.0011	0.348433	0.000018	0.510807	0.000059	-9.9	0.033	0.0006	31.00	1.00	5.8
24	0.511415	0.000024	0.0985	0.0012	0.348452	0.000023	0.510805	0.000058	-11.9	0.135	0.015	18.55	0.40	5.1
26	0.511420	0.000026	0.0974	0.0022	0.348443	0.000020	0.510822	0.000059	-11.8	0.110	0.011	20.00	1.00	5.6
28	0.511448	0.000024	0.0938	0.0040	0.348446	0.000021	0.510847	0.000059	-10.2	0.055	0.003	22.50	2.60	4.4
29	0.511411	0.000025	0.0925	0.0019	0.348449	0.000019	0.510784	0.000059	-10.0	0.100	0.017	22.30	1.10	3.5

[1]From Ayers et al., (2006). Mean value of nearest spots

Table 5-2: LASS U-Pb results for BCP and related samples (ages in Ma)

Grain	^{206}Pb-^{238}U Age	Prop 2SE	^{207}Pb-^{235}U Age	Prop 2SE	^{207}Pb-^{206}Pb Age	Prop 2SE	$^{238}U/^{206}Pb$	Prop 2SE	$^{207}Pb/^{206}Pb$	Prop 2SE	$^{207}Pb/^{235}U$	Prop 2SE	$^{206}Pb/^{238}U$	Prop 2SE
BS-1														
1	102.9	6.1	230	21	89	5.7	62.23	3.72	0.1570	0.0170	0.28	0.03	0.016	0.001
1	91.7	4.3	111.6	6.6	90	4.3	69.78	3.31	0.0604	0.0031	0.12	0.01	0.014	0.001
9	97.4	5.3	108	12	96	5.3	65.62	3.62	0.0597	0.0067	0.12	0.01	0.015	0.001
9	94.5	4.9	202	15	87	4.6	67.66	3.48	0.1132	0.0087	0.22	0.02	0.015	0.001
15	94.8	8.2	148	40	91	8.5	67.57	5.93	0.0790	0.0240	0.16	0.05	0.015	0.001
16	100.6	7.1	353	37	68	7.4	63.45	4.43	0.3060	0.0440	0.49	0.06	0.016	0.001
20	88.7	4.6	87.1	8.2	88	4.6	72.15	3.75	0.0508	0.0047	0.09	0.01	0.014	0.001
BS-2														
1	88.3	6.3	123	28	86	6.4	72.46	5.20	0.0680	0.0170	0.14	0.03	0.014	0.001
2	89	4.8	112	13	87	4.8	71.94	3.93	0.0653	0.0077	0.12	0.01	0.014	0.001
3	93.9	5.5	110	14	91	5.5	68.07	4.03	0.0697	0.0090	0.12	0.02	0.015	0.001
7	87.6	4.1	89.2	5.3	87	4.1	73.10	3.42	0.0489	0.0025	0.09	0.01	0.014	0.001
CS-1														
1	92.9	4.9	108.2	10	91	4.9	68.87	3.65	0.0614	0.0057	0.12	0.01	0.015	0.001
2	93.2	4.8	157	12	89	4.7	68.63	3.58	0.0870	0.0067	0.17	0.01	0.015	0.001
4	100	6.2	129	16	94	6.1	63.90	3.96	0.0970	0.0150	0.15	0.02	0.016	0.001
7	84.5	4.4	94.9	8.8	84	4.5	75.76	4.02	0.0554	0.0050	0.10	0.01	0.013	0.001
8	96.8	9.5	240	42	98	15.3	65.79	6.49	0.0400	0.0960	0.38	0.07	0.015	0.002

Grain	^{206}Pb-^{238}U Age	Prop 2SE	^{207}Pb-^{235}U Age	Prop 2SE	^{207}Pb-^{206}Pb Age	Prop 2SE	$^{238}U/^{206}Pb$	Prop 2SE	$^{207}Pb/^{206}Pb$	Prop 2SE	$^{207}Pb/^{235}U$	Prop 2SE	$^{206}Pb/^{238}U$	Prop 2SE
CS-2														
1	98.8	5.9	107	15	97	5.9	64.72	3.85	0.0610	0.0090	0.12	0.02	0.015	0.001
2	92.9	4.8	105.5	10	92	4.8	68.97	3.61	0.0580	0.0055	0.11	0.01	0.015	0.001
3	104.7	8.1	249	31	80	8.3	60.98	4.83	0.2340	0.0400	0.32	0.04	0.016	0.001
4	87.8	4.5	100.8	8.3	86	4.5	72.89	3.77	0.0600	0.0049	0.11	0.01	0.014	0.001
5	93.1	5.3	133	14	89	5.2	68.73	3.97	0.0840	0.0092	0.15	0.02	0.015	0.001
Dma-1 (young)														
4	89.1	3.3	80.3	9.9	89	3.4	71.79	2.68	0.0479	0.0061	0.09	0.01	0.014	0.001
5	87.7	3.4	77	11	88	3.5	72.99	2.88	0.0437	0.0066	0.08	0.01	0.014	0.001
6	85.5	5.7	120	22	83	5.8	74.91	5.05	0.0740	0.0150	0.13	0.03	0.013	0.001
7	84.5	3	92	12	84	3.1	75.76	2.70	0.0534	0.0071	0.10	0.01	0.013	0.001
8	87	3.6	80	11	87	3.7	73.53	3.03	0.0489	0.0074	0.09	0.01	0.014	0.001
9	87.3	2.9	85.2	8.3	87	3.0	73.31	2.47	0.0502	0.0051	0.09	0.01	0.014	0.001
13	91.1	3.5	94	13	90	3.6	70.22	2.71	0.0549	0.0079	0.10	0.01	0.014	0.001
14	108	4.6	436	21	82	4.2	59.14	2.52	0.2380	0.0170	0.54	0.03	0.017	0.001
14	101.7	3.9	326	17	85	3.6	62.85	2.45	0.1770	0.0120	0.39	0.02	0.016	0.001
15	85.5	3	89.5	8.8	85	3.0	74.85	2.63	0.0540	0.0057	0.09	0.01	0.013	0.001
15	89.2	2.9	81.1	8.7	89	3.0	71.79	2.37	0.0462	0.0051	0.09	0.01	0.014	0.001
16	86	4.3	104	16	85	4.4	74.35	3.76	0.0596	0.0099	0.11	0.02	0.013	0.001
16	85.8	5.1	73	16	85	5.3	74.52	4.50	0.0550	0.0120	0.08	0.02	0.013	0.001
17	88.1	3.8	87	11	88	3.9	72.62	3.16	0.0507	0.0073	0.09	0.01	0.014	0.001
17	94.5	4.3	78	13	95	4.4	67.70	3.12	0.0434	0.0076	0.08	0.01	0.015	0.001

Grain	^{206}Pb-^{238}U Age	Prop 2SE	^{207}Pb-^{235}U Age	Prop 2SE	^{207}Pb-^{206}Pb Age	Prop 2SE	$^{238}U/^{206}Pb$	Prop 2SE	$^{207}Pb/^{206}Pb$	Prop 2SE	$^{207}Pb/^{235}U$	Prop 2SE	$^{206}Pb/^{238}U$	Prop 2SE
Dma-1 (old)														
1	334.9	7.2	332.6	6.9	335	7.5	18.75	0.42	0.0528	0.0016	0.39	0.01	0.053	0.001
12	329.6	8.9	348	14	328	9.3	19.05	0.54	0.0570	0.0028	0.41	0.02	0.053	0.002
19	335	11	332	10	335	10.6	18.73	0.60	0.0533	0.0025	0.39	0.01	0.053	0.002
19	383	8.3	378.5	9.2	383	8.7	16.33	0.37	0.0542	0.0019	0.45	0.01	0.061	0.001
DU-1														
1	955	38	935	40	957	41.3	6.25	0.28	0.0710	0.0028	1.56	0.11	0.160	0.007
1	800	33	793	38	800	34.2	7.56	0.33	0.0659	0.0028	1.19	0.08	0.132	0.006
2	1149	45	1144	42	1149	49.8	5.12	0.23	0.0787	0.0027	2.10	0.14	0.195	0.009
4	1070	42	1049	43	1074	46.1	5.52	0.24	0.0750	0.0026	1.82	0.13	0.181	0.008
5	1092	53	1027	50	1099	56.7	5.41	0.29	0.0720	0.0038	1.76	0.14	0.185	0.010
5	1081	50	1031	43	1078	55.3	5.50	0.29	0.0750	0.0034	1.77	0.13	0.182	0.010
6	1026	62	1020	50	1040	69.2	5.71	0.39	0.0748	0.0044	1.78	0.15	0.175	0.012
19	640	30	645	36	637	30.9	9.57	0.48	0.0660	0.0026	0.90	0.07	0.105	0.005
20	1023	45	1002	49	1029	47.7	5.80	0.28	0.0708	0.0040	1.70	0.14	0.172	0.008
21	1087	50	1067	48	1107	57.1	5.35	0.28	0.0745	0.0040	1.88	0.15	0.187	0.010
22	1070	46	1056	51	1066	50.0	5.54	0.27	0.0785	0.0040	1.91	0.15	0.181	0.009
23	1013	59	1033	54	1018	63.6	5.84	0.38	0.0739	0.0046	1.80	0.16	0.171	0.011
1	927	47	974	41	924	49.3	6.46	0.35	0.0735	0.0036	1.61	0.10	0.155	0.009
2	1038	52	1045	39	1036	54.7	5.72	0.31	0.0754	0.0028	1.78	0.10	0.175	0.010
4	1056	52	1053	38	1056	54.8	5.62	0.30	0.0739	0.0026	1.82	0.10	0.178	0.010
5	969.3	47	994	35	968	49.8	6.16	0.33	0.0726	0.0023	1.66	0.09	0.162	0.009

Grain	^{206}Pb-^{238}U Age	Prop 2SE	^{207}Pb-^{235}U Age	Prop 2SE	^{207}Pb-^{206}Pb Age	Prop 2SE	$^{238}U/^{206}Pb$	Prop 2SE	$^{207}Pb/^{206}Pb$	Prop 2SE	$^{207}Pb/^{235}U$	Prop 2SE	$^{206}Pb/^{238}U$	Prop 2SE
DU-1 (cont.)														
19	989.9	48	973.5	34	991	50.4	6.03	0.32	0.0711	0.0022	1.61	0.09	0.166	0.009
20	944	47	944	39	942	50.0	6.35	0.35	0.0716	0.0032	1.54	0.10	0.158	0.009
21	1178	57	1141	37	1184	63.1	4.99	0.27	0.0755	0.0025	2.07	0.11	0.201	0.011
22	934	46	998	39	923	48.4	6.42	0.35	0.0791	0.0035	1.69	0.11	0.156	0.008
23	1020.6	50	1014	36	1022	52.6	5.82	0.31	0.0727	0.0024	1.71	0.10	0.172	0.009
24	945	46	947.9	33	944	48.2	6.34	0.33	0.0712	0.0021	1.55	0.08	0.158	0.008
26	933.5	46	925	33	935	47.7	6.41	0.34	0.0693	0.0022	1.49	0.08	0.156	0.008
28	981	50	1015	38	976	51.4	6.09	0.33	0.0752	0.0031	1.74	0.11	0.164	0.009
29	1027.8	50	990	35	1033	52.7	5.78	0.30	0.0698	0.0022	1.65	0.09	0.173	0.009

Chapter 6. Conclusions

The Sm-Nd isotope and U-Pb age data obtained on monazite by the LASS method are shown to have geological useful accuracy and precision based on comparison with ID-TIMS data from the same samples. The LASS ages for 6 of 8 samples analyzed in this study agree within 2σ uncertainty with high precision ID-TIMS ages. Importantly, the LASS method provides a robust way to measure U-Pb age and Sm-Nd isotopes simultaneously from the same ablation volume, thus eliminating any uncertainties associated with correlating data from two different ablation volumes, while still maintaining useful accuracy and precision. This advantage is most useful in studies involving grains with complex fine-scaled zoning in age and isotopic composition. In addition, this method is potentially useful in detrital monazite studies, where a large number of grains need to be analyzed. However, there are still some issues with laser induced elemental fractionation of U/Pb in some of the samples analyzed in this study, due to the laser parameters required for precise Sm-Nd. Further refinement of the LASS ablation parameters and on down-hole fractionation corrections will help improve the quality of the U-Pb data in future studies.

New LASS U-Pb and Sm-Nd data show that monazite from the Birch Creek Pluton (BCP) and altered country rock adjacent to the pluton have homogenous and overlapping initial Nd isotope compositions, strengthening the hypothesis of *Ayers et al.* [2006] that monazite in the hydrothermal aureole was affected by hydrothermal fluids sourced from the BCP. The data suggest that the mechanism behind the formation of pluton-aged monazite in a nearby altered sedimentary unit could have been new growth alone, although some contribution from dissolution-reprecipitation cannot yet be ruled

out. The LASS U-Pb ages are ~4-5% higher than new high-precision ID-TIMS U-Pb ages from the same monazite grains, likely due to analytical uncertainty of the LASS methodology combined with uncorrected elemental fractionation of U/Pb in these young grains. These results demonstrate how monazite age and Sm-Nd isotopic data, coupled with oxygen isotopic data, can be used to identify hydrothermal monazite, constrain the timing of fluid events and map the potential sources of hydrothermal fluids.

References

Ayers, J. C., M. Loflin, C. F. Miller, M. D. Barton, and C. D. Coath (2006), In situ oxygen isotope analysis of monazite as a monitor of fluid infiltration during contact metamorphism: Birch Creek Pluton aureole, White Mountains, eastern California. *Geology*, 34, 653–656. doi:10.1130/G22185.1.

Barton, M. D (2000), Overview of the lithophile element-bearing magmatic-hydrothermal system at Birch Creek, White Mountains, California, in Constraining Styles of Intrusion Associated Hydrothermal Systems, Society of Economic Geologists Guide Book Series, vol. 32, edited by J. H. Dillies, M. D. Barton, D. A. Johnson, J. M. Proffett, and M. T. Einaudi, pp. 9–26.

Bouvier, A., J. D. Vervoort, and P.J. Patchett (2008), The Lu–Hf and Sm–Nd isotopic composition of CHUR: Constraints from unequilibrated chondrites and implications for the bulk composition of terrestrial planets. Earth Planet. Sci. Lett., 273, 48-57. doi: 10.1016/j.epsl.2008.06.010

Cherniak, D. J. (2010), Diffusion in accessory minerals; zircon, titanite, apatite, monazite and xenotime, *Rev. Mineral. & Geochem.*, 72, 827–869. doi:10.2138/rmg.2010.72.18.

Chew, D.M., J.A. Petrus, and B.S. Kamper (2014), U-Pb LA-ICPMS dating using accessory minerals with variable common Pb. Chem. Geol., 363, 185-199. doi: 10.1016/j.chemgeo.2013.11.006

Davis, W. J., R. R. Parrish, V. McNicoll, and D. Bellerive (1998), Analytical techniques for the determination of $^{208}Pb/^{232}Th$ ages of monazite and zircon at the Geochronology Laboratory, Geologic Survey of Canada, in Radiogenic Age and Isotope Studies: Report 11, Geological Survey of Canada, Current Research 1998-F, 19–22.

DePaolo, D.J. (1988), Neodymium Isotope Geochemistry an Introduction. Springer-Verlag, Berlin.

Evans, J., and J. Zalasiewicz (1996), U-Pb, Pb-Pb, and Sm-Nd dating of authigenic monazite: Implications for the diagenetic evolution of the Welsh Basin, *Earth Planet. Sci. Lett.*, 144, 421–433.

Fisher, C. M., C. R. M. McFarlane, J. M. Hanchar, M. D. Schmitz, P. J. Sylester, R. Lam, and H. P. Longerich (2011), Sm-Nd isotope systematics by laser ablation-multicollector-inductively coupled plasma mass spectrometry: Methods and potential natural and synthetic reference materials, *Chem. Geol.*, 284, 1–20, doi:10.1016/j.chemgeo.2011.01.012.

Foster, G., P. Kinny, D. Vance, C. Prince, and N. Harris (2000), The significance of monazite U-Th-Pb age data in metamorphic assemblages; a combined study of monazite and garnet chronometry, Earth Planet. Sci. Lett., 181, 327-340. doi: S0012-821X(00)00212-0

Fowler, A. D., and R. Doig (1983), The significance of europium anomalies in the REE spectra of granites and pegmatites, Mont Laurier, Quebec, *Geochim. Cosmochim. Acta*, 47, 1131–1137.

Gebauer, D., and M. Grünenfelder (1979), U-Th-Pb dating of minerals, in Lectures in Isotope Geology, edited by E. Jager and J. C. Hunziker, pp. 105–131.

Gerstenberger, H., and G. Haase, (1997), A highly effective emitter substance for mass spectrometric Pb isotope ratio determinations: *Chem. Geol*., 136, 309-312.

Harlov, D. E., R. Wirth, and C. J. Hetherington (2011), Fluid-mediated partial alteration in monazite: the role of coupled dissolution-reprecipitation in element redistribution and mass transfer, *Contrib. Mineral. Petrol*, 162, 329-348.

Harrison, T. M., E. J. Catlos, and J.-M Montel (2002), U-Th-Pb dating of phosphate minerals, *Rev. Mineral. Geochem.*, 48, 523–558.

Hawkesworth, C.J., and A.I.S. Kemp (2006), Using hafnium and oxygen isotopes in zircons to unravel the record of crustal evolution, *Chem. Geol.*, 226, 144-162. doi:10.1016/j.chemgeo.2005.09.018

Hawkins, D. P., and S. A. Bowring (1997), U-Pb systematics of monazite and xenotime: case studies from the Paleoproterozoic of the Grand Canyon, Arizona, *Contrib. Mineral. Petrol.*, 127, 87–103.

Heaman, L., and R. Parrish (1991), U-Pb geochronology of accessory minerals, in Applications of Radiogenic Isotope Systems to Problems in Geology: Short Course Handbook 19, edited by L. Heaman and J. N. Ludden, pp. 59–102, Mineralogical Association of Canada.

Hietpas, J., S. Samson, D. Moecher, and A. K. Schmitt (2010), Recovering tectonic events from the sedimentary record: Detrital monazite plays in high fidelity, *Geology*, 38, 167–170. doi:10.1130/G30265.1.

Hietpas, J., S. Samson, and D. Moecher (2011), A direct comparison of the ages of detrital monazite versus detrital zircon in Appalachian foreland basin sandstones: Searching for the record of Phanerozoic orogenic events, *Earth Planet. Sci. Lett.*, 310, 488–497. doi:10.1016/j.epsl.2011.08.033.

Iizuka, T., S. M. Eggins, M. T. McCulloch, L. P. J. Kinsley, and G. E. Mortimer (2011A), Precise and accurate determination of $^{147}Sm/^{144}Nd$ and $^{143}Nd/^{144}Nd$ in monazite using laser ablation-MC-ICP-MS, *Chem. Geol.*, 282, 45–57. doi:10.1016/j.chemgeo.2011.01.008.

Iizuka, T., O. Nebel, and M. T. McCulloch (2011B), Tracing the provenance and recrystallization processes of the Earth's oldest detritus at Mt. Narryer and Jack Hills, Western Australia: An in situ Sm–Nd isotopic study of monazite, *Earth Planet. Sci. Lett.*, 308, 350–358. doi:10.1016/j.epsl.2011.06.006.

Isnard, H., R. Brennetot, C. Caussignac, N. Caussignac, and F. Cartier (2005), Investigations for determinations of Gd and Sm isotopic compositions in spent nuclear fuels samples by MC ICPMS. *International Journal of Mass Spectrometry,* 246, 66-73.

Jackson, S.E., N.J. Pearson, W.L. Griffin, E.A. Belousova (2004), The application of laser ablation-inductively coupled plasma-mass spectrometry to in-situ U-Pb zircon geochronology. *Chem. Geol.,* 211, 47-69. doi:10.1016/j.chemgeo.2004.06.017.

Jaffey, A.H., K.F. Flynn, L.E. Glendenin, W.C. Bentley, and A.M. Essling, (1971), Precision measurements of half-lives and specific activities of ^{235}U and ^{238}U, *Phys. Rev. C,* 4, 1889-1906.

Kemp, A.I.S., C.J. Hawkesworth, B.A. Paterson and P.D. Kinny, (2006), Episodic growth of the Gondwana super continent from hafnium and oxygen isotopes in zircon. *Nature*, 439, 580-583. doi: 10.1038/nature04505

Kemp, A. I. S., G. I. Foster, A. Scherstén, M. J. Whitehouse, J. Darling, and C. Storey (2009), Concurrent Pb–Hf isotope analysis of zircon by laser ablation multicollector ICP-MS, with implications for the crustal evolution of Greenland and the Himalayas, *Chem. Geol*., 261, 244–260. doi:10.1016/j.chemgeo.2008.06.019.

Kohn, M. J., and J. D. Vervoort (2008), U-Th-Pb dating of monazite by single collector ICP-MS: Pitfalls and potential, *Geochem., Geophys., Geosys.*, 9, Q04031. doi:10.1029/2007GC001899.

Košler, J., M. N. Tubrett, and P. J. Sylvester (2001), Application of laser ablation ICP-MS to U-Th-Pb dating of monazite, *Geostand. Geoanal. Res.*, 25, 375–386.

Košler, J., and P. J. Sylvester (2003), Present trends and the future of zircon in geochronology: Laser ablation ICP-MS, in *Reviews in Mineralogy & Geochemistry*, vol. 53, edited by J. M. Hanchar and P. W. O. Hoskin, pp. 243–275.

Kylander-Clark, A.R.C., Hacker, B.R., and Cottle, J.M. (2013), Laser Ablation Split-Stream ICP Petrochronology, *Chem. Geo.,* doi: 10.1016/j.chemgeo.2013.02.019

Krogh, T.E., (1973), A low contamination method for hydrothermal decomposition of zircon and extraction of U and Pb for isotopic age determination. *Geochim. Cosmochim. Acta*, 37, 485-494.

Liu, Z.C., F.Y. Wu, Y.H. Yang, J.H. Yang, and S.A. Wilde (2012), Neodymium isotopic compositions of the standard monazites used in U-Th-Pb geochronology. *Chem. Geo.*, 334, 221-239.

Ludwig, K.R., (2003), User's Manual for Isoplot 3.00. Berkeley Geochronology Center: Berkeley, CA, 70 p.

Lugamir, G.W. and K. Marti (1978), Lunar initial $^{143}Nd/^{144}Nd$: Differential evolution of the lunar crust and mantle. *Earth Planet. Sci. Lett., 39, 349-357.*

MacLachlan, K., N. Rayner, G. Dunning, and C. Leugner (2004), New results and ideas from the Rottenstone Domain project, in Summary of Investigations 2004, vol. 2, Saskatchewan Geological Survey, Sask. Industry Resources, Misc. Rep. 2004-4.2, CD-ROM, Paper A-3, p. 21.

McFarlane, C. R. M., and M. T. McCulloch (2007), Coupling of in-situ Sm-Nd systematics and U-Pb dating of monazite and allanite with application to crustal evolution studies, *Chem. Geol*., 245, 45–60. doi:10.1016/j.chemgeo.2007.07.020.

Moecher, D., J. Hietpas, S. Samson, and S. Chakreborty (2011), Insights into southern Appalachian tectonics from ages, *Geosphere*, 7, 494–512. doi:10.1130/GES00615.1.

Moore, B.T., Hanchar, J.M., Chafe, A., and Fournelle, J. (2013) Rare earth element substitution and charge balancing in synthetic apatite. *Program with Abstracts, Geological Association of Canada-Mineralogical Association of Canada Annual Meeting, Winnipeg, Canada, May 22-24, 2013,* 36: p. 148.

Parrish, R. R. (1990), U-Pb dating of monazite and its application of geologic problems, *Can. J. Earth Sci*., 27, 1431–1450.

Paton, C., J. C. Hellstrom, B. Paul, J. D. Woodhead, and J. M. Hergt (2011), Iolite: Freeware for the visualisation and processing of mass spectrometric data, *J. Anal. At. Spectrom.,* 26, 2508–2518. doi:10.1039/c1ja10172b.

Paton, C., J. D. Woodhead, J. C. Hellstrom, J. M. Hergt, A. Greig, and R. Maas (2010), Improved laser ablation U-Pb zircon geochronology through robust downhole fractionation correction, *Geochem., Geophys., Geosystems*., 11, Q0AA06. doi:10.1029/2009GC002618.

Ross, G. M., R. R. Parrish, and F. Ö. Dudás (1991), Provenance of the Bonner Formation (Belt Supergroup), Montana: Insights from U-Pb and Sm-Nd analyses of detrital minerals, *Geology*, 19, 340–343.

Schärer, U. (1984), The effect of initial ^{230Th} disequilibrium on young U-Pb ages: the Makalu case, Himalaya, *Earth Planet. Sci. Lett., 67, 191-204.*

Schmitz, M.D., and B. Schoene, (2007), Derivation of isotope ratios, errors and error correlations for U-Pb geochronology using ^{205}Pb-^{235}U-(^{233}U)-spiked isotope dilution thermal ionization mass spectrometric data: *Geochem, Geophys, Geosystems* 8, Q08006. doi:10.1029/2006GC001492.

Stacey, J.S., and J.D. Kramers, (1975), Approximation of terrestrial lead isotope evolution by a two-stage model: Earth and Planetary Science Letters 26:207-221.

Stern, R. A., and R. G. Berman (2001), Monazite U-Pb and Th-Pb geochronology by ion microprobe, with an application to in situ dating of an Archean metasedimentary rock, *Chem. Geol*., 172, 113–130.

Stern, R. A., and N. Sanborn (1998), Monazite U-Pb and Th-Pb geochronology by high resolution secondary ion mass spectrometry, in Radiogenic Age and Isotopic Studies: Report 11; Geologic Survey of Canada, Current Research 1998-F, pp. 1–18.

Tollstrup, D. L., L.W. Xie, J. B. Wimpenny, E. Chin, C. T. Lee, and Q. Z. Yin (2012), A trio of laser ablation in concert with two ICP-MSs: Simultaneous, pulse-by-pulse determination of U-Pb discordant ages and a single spot Hf isotope ratio analysis in complex zircons from petrographic thin sections, *Geochem. Geophys. Geosyst*., 13, Q03017. doi:10.1029/2011GC004027.

Tomascak, P. B., E. J. Krogstad, and R. J. Walker (1996), U-Pb monazite geochronology of granitic rocks from Maine: Implications for late paleozoic tectonics in the Northern Appalachians, *J. Geol*., 104, 185–195.

Tomascak, P. B., E. J. Krogstad, and R. J. Walker (1998), Sm-Nd isotope systematics and the derivation of granite pegmatites in southwestern Maine, *Can. Mineral*., 36, 327–337.

Trail, D., E.B. Watson, and N.D. Tailby (2012) Ce and Eu anomalies in zircon as proxies for the oxidation states of magmas. *Geochim. Cosmochim. Acta*, 97, 70-87.

http://dx.doi.org/10.1016/j.gca.2012.08.032

Warren, C.J., D. Grujie, D.A. Kellett, J. Cottle, R.A. Jamieson, and K.S. Ghalley (2011), Probing the depth of the India-Asia collision: U-Th-Pb monazite chronology of granulites from NW Bhutan, *Tectonics*, 30, TC2004. doi: 10.1029/2010TC002738

Wiedenbeck, M., J.M. Hanchar, W.H. Peck, P. Sylvester, J. Valley, M. Whitehouse, A. Kronz, Y. Morishita, L. Nasdala (2004), Further characterisation of the 91500 zircon crystal, *Geostand. Geoanal. Res.*, 28, 9-39.

Williams, M. L., M. J. Jercinovic, and C. J. Hetherington (2007), Microprobe monazite geochronology: Understanding geologic processes by integrating composition and chronology, *Annu. Rev. Earth Planet. Sci*., 35, 137–175. doi:10.1146/annurev.earth.35.031306.140228.

Williams, M. L., M. J. Jercinovic, D. E. Harlov, B. Budzyń and C.J. Hethington (2011), Resetting monazite ages during fluid-related alteration, *Chem. Geol*., 283, 218-225. doi:10.1016/j.chemgeo.2011.01.019

Williams, M. L., and M. J. Jercinovic (2012), Tectonic interpretation of metamorphic tectonites: integrating compositional mapping, microstructural analysis and in situ monazite dating, *J. Metamorphic Geol*., 30, 739–752. doi:10.1111/j.1525-1314.2012.00995.x.

Xie, L. W., Y. B. Zhang, H. H. Zhang, J. F. Sun, and F. Y. Wu (2008), *In situ* simultaneous determination of trace elements, U-Pb and Lu-Hf isotopes in zircon and baddeleyite, *Chinese Science Bulletin*, 53(10), 1565–1573. doi:10.1007/s11434-008-0086-y.

Yang, Y. H., F. Y. Wang, S. A. Wilde, X. M. Liu, Y. B. Zhang, L. W. Xie, and J. H. Yang (2009), In situ perovskite Sr-Nd isotopic constraints on the petrogenesis of the Ordovician Mengyin kimberlites in the North China Craton, *Chem. Geol*., 264, 24–42. doi:10.1016/j.chemgeo.2009.02.011.

Yuan, H. L., S. Gao, M. N. Dai, C. L. Zong, D. Günther, G. H. Fontaine, X. M. Liu, and C. R. Diwu (2007), Simultaneous determinations of U-Pb age, Hf isotopes and trace element compositions of zircon by excimer laser-ablation quadrupole and multiple-collector ICP-MS, *Chem. Geol*., 247, 100–118. doi:10.1016/j.chemgeo.2007.10.003.

APPENDIX A:

A.1 ID-TIMS methodology

Four to seven monazite grains from three samples from the Birch Creek Pluton were dated by the isotope dilution thermal ionization mass spectrometry method (ID-TIMS) at Boise State University. These grains were the same grains that were used for LASS measurements. Monazite was mounted in epoxy and polished until the grain centers were exposed. Backscattered electron images were obtained using a scanning electron microscope. Grains that exhibited the least complex zoning patterns were chosen for analysis. Single monazite grains were put in 3 ml Teflon PFA beakers, ultrasonically cleaned for an hour in ultrapure H_2O, fluxed on a hotplate at 80°C for 15 minutes in 3.5 M HNO_3, and loaded into 300 µl Teflon PFA microcapsules and spiked with the mixed Boise State ^{233}U-^{235}U-^{205}Pb tracer solution. Fifteen microcapsules were placed in a large-capacity Parr vessel. Grains were dissolved in 120 µl of 6 M HCl at 180°C for 48 hours, dried to fluorides, and then re-dissolved in 6 M HCl at 180°C overnight. U and Pb were separated from the zircon matrix using an HCl-based anion-exchange chromatographic procedure [*Krogh*, 1973], eluted together and dried with 2 µl of 0.05 N H_3PO_4.

Pb and U were loaded on a single outgassed Re filament in 2 µl of a silica-gel/phosphoric acid mixture [*Gerstenberger and Haase*, 1997], and U and Pb isotopic measurements made on an Isotopx Isoprobe-T multicollector thermal ionization mass spectrometer equipped with an ion-counting Daly detector. Pb isotopes were measured by peak-jumping all isotopes on the Daly detector for 100 to 150 cycles, and corrected for 0.18 ± 0.03%/a.m.u. (1 sigma) mass fractionation. Transitory isobaric interferences due to high-molecular weight organics, particularly on ^{204}Pb and ^{207}Pb, disappeared within approximately 30 cycles, whereas ionization efficiency averaged 10^4 cps/pg of each Pb

isotope. Linearity (to ≥1.4 x 10^6 cps) and the associated deadtime correction of the Daly detector were monitored by repeated analyses of NBS982, and have been constant since installation. Uranium was analyzed as UO_2^+ ions in static Faraday mode on 10^{11} ohm resistors for 150 to 200 cycles, and corrected for isobaric interference of $^{233}U^{18}O^{16}O$ on $^{235}U^{16}O^{16}O$ with an $^{18}O/^{16}O$ of 0.00206. Ionization efficiency averaged 20 mV/ng of each U isotope. U mass fractionation was corrected using the known $^{233}U/^{235}U$ ratio of the tracer solution.

The $^{207}Pb/^{235}U$ dates are used rather than $^{206}Pb/^{238}U$ dates due to initial Th-U disequilibrium. Weighted mean $^{207}Pb/^{235}U$ dates were calculated from 3-6 equivalent dates using Isoplot 3.0 [*Ludwig*, 2003] and are interpreted as being the igneous crystallization age. Uncertainties on the weighted mean $^{207}Pb/^{235}U$ dates are the internal uncertainties based on analytical uncertainties only, including counting statistics, subtraction of tracer solution, and blank and initial common Pb subtraction. They are given at the 2σ confidence interval. These uncertainties should be considered when comparing our dates with $^{207}Pb/^{235}U$ dates from other laboratories that used the same Boise State University tracer solution or a tracer solution that was cross-calibrated using EARTHTIME gravimetric standards. When comparing our dates with those derived from laboratories that did not use the same tracer solution or a tracer solution that was not cross-calibrated using EARTHTIME gravimetric standards, a systematic uncertainty in the tracer calibration of 0.05% should be added to the internal uncertainties in quadrature. When comparing our dates with those derived from other decay schemes (e.g., $^{206}Pb/^{238}U$, $^{40}Ar/^{39}Ar$, ^{187}Re-^{187}Os), systematic uncertainties in the tracer calibration and ^{235}U decay constant [*Jaffey et al*., 1971] should be added to the internal error in quadrature. These

uncertainties are given as $^{207}Pb/^{235}U$ date ± x / y / z Ma, where x is the internal error, y includes the uncertainty in the tracer calibration, and z includes the uncertainties in the tracer calibration and ^{235}U decay constant. Uncertainties on the $^{207}Pb/^{235}U$ dates from individual grains are also given at the 2σ confidence interval.

U-Pb dates and uncertainties were calculated using the algorithms of *Schmitz and Schoene* [2007], $^{235}U/^{205}Pb$ of 77.93 and $^{233}U/^{235}U$ of 1.007066 for the Boise State University tracer solution, and U decay constants recommended by *Jaffey et al*. [1971]. All common Pb in analyses was assigned to the monazite with a composition determined by *Stacey and Kramers* [1975], except for 0.4 pg that was assigned to laboratory blank and subtracted based on the measured laboratory Pb isotopic composition and associated uncertainty. U blanks are difficult to precisely measure, but are estimated at 0.07 pg.

Seven aliquots of the EARTHTIME 100 Ma synthetic solution were measured during this experiment using the Boise State University tracer solution and the same mass spectrometry methods described above. Each aliquot was 4-6 pg of radiogenic Pb, slightly smaller than the average analysis measured during the experiment. The weighted mean $^{206}Pb/^{238}U$ and $^{207}Pb/^{235}U$ dates are 100.08 ± 0.03 / 0.10 and 100.04 ± 0.13 / 0.16 Ma, respectively. These dates agree with the known dates determined by analysis of large aliquots measured with the EARTHTIME mixed ^{233}U-^{235}U-^{202}Pb-^{205}Pb tracer solution [*D. Condon*, unpublished data].

APPENDIX B:

See supplementary data for appendix tables:

Table B-1: Trebilcock monazite Sm-Nd results

Table B-2: KMO3-72 and 93-GD-12 LASS results

Table B-3: LREE glass Sm-Nd results

Table B-4: BCP ID-TIMS U-Pb results